The Experimental Investigation of the Effect of Unsteady Obstacle Wakes on Stirring and Mixing of Gamete Filaments

by

F. Shoaei

B.S., Amirkabir University of Technology, 2007

M.S., Sharif University of Technology, 2009

A thesis submitted to the

Faculty of the Graduate School of the

University of Colorado in partial fulfillment

of the requirements for the degree of

Doctor of Philosophy

Department of Civil, Environmental, and Architectural Engineering

2015

This thesis entitled:
The Experimental Investigation of the Effect of Unsteady Obstacle Wakes on Stirring and Mixing of Gamete Filaments
written by F. Shoaei
has been approved for the Department of Civil, Environmental, and Architectural Engineering

_____

Prof. John Crimaldi

_____

Prof. Harihar Rajaram

_____

Prof. Roseanna Neupauer

_____

Prof. Peter Hamlington

_____

Prof. Joseph Kasprzyk

Date _____

The final copy of this thesis has been examined by the signatories, and we find that both the content and the form meet acceptable presentation standards of scholarly work in the above mentioned discipline.

Shoaei, F. (Ph.D., Civil Engineering)

The Experimental Investigation of the Effect of Unsteady Obstacle Wakes on Stirring and Mixing of Gamete Filaments

Thesis directed by Prof. John Crimaldi

One of the most common methods of reproduction in the sea is broadcast spawning where marine invertebrates release eggs and sperm into the ambient flow and fertilization occurs externally. Gamete coalescence at large scales is dominated by fluid stirring, and may be influenced by the presence of flow obstructions (e.g., coral heads, bed topography). The effect of turbulent wake behind a round obstacle on the second-order reaction between two initially distant scalars has been investigated by series of planar laser-induced fluorescence experiments. The scalars are released continuously, and are separated from each other by a lateral distance that initially impedes the reaction. The direct effect of the wake on mixing enhancement is determined by comparing segregation coefficient for cases with and without the cylinder wake. We measured mixing statistics for variety of flow regimes, streamwise locations, and scalar release geometries. This study suggests that the presence of turbulent obstacle wakes in spawning regions may substantially raise the efficacy of external fertilization. In addition, the effect of viscosity and non-Newtonian (shear-thinning) rheology on mixing and reaction between two initially distant scalars has been investigated. In this case, the ambient flow is pure water, but the scalar solutions include Xanthan gum to alter their rheology. Results indicate that mixing and reaction rates in the low-Damkohler limit between the two scalars plumes increase with the increase in viscosity of the scalars. The results of this study have broad implications for biological and ecological mixing processes involving now-Newtonian fluids.

Dedication

To My Love, Mahshid.

Thank you for encouraging me to do my best and being my biggest supporter. Your love, support, and encouragement has brought me through some of the toughest times in this journey.

Acknowledgements

I would like to convey my sincere gratitude towards the following people who were instrumental to my success and well-being:

Dr. John Crimaldi - I would like to thank you for your consistent guidance. Your insightful suggestions, encouragement, and constructive criticism has and will make me a better scientist. I wish to express to you my deepest appreciation and gratitude. Without your support and guidance none of this would have been possible.

Committee Members - I would like to thank Dr. Hari Rajaram, Dr. Roseanna Neupauer, Dr. Peter Hamlington , and Dr. Joseph Kasprzyk for all of their comments and suggestions. Thank you for teaching me to never accept less than excellence.

Research Group and Officemates - A big thank you to Mike Soltys, Kenneth Pratt, Aaron True, Jose Solis, Sachin Pandey, Amy Piscopo and Masoud Arshadi for a great working environment and positive encouragement. Thank you all for your support and friendships along the way.

My Mom and Dad, for their unwavering support and insistence that I can do whatever I put my mind to. Your love and support are invaluable to me. Without your confidence and friendship, I would not be where I am today. Also thanks to my sister, Farnaz, who is always a source of joy and encouragement. I am very proud of you.

Contents

Chapter

Tables

Table

Figures

Figure

Chapter 1

Introduction

1.1 The Biology of Broadcast Spawning

Many benthic invertebrates utilize broadcast spawning as a reproductive strategy. Species using this form of external fertilization are typically sessile (e.g. sea urchins, sea anemones, corals) or are limited in their ability to aggregate by the nature of their chosen habitats or environments. In a wide variety of rocky shore organisms, spawning synchrony could increase the probability of gamete encounters. It could also mitigate deleterious effects of sperm aging [47, 80, 79, 72]. When gametes are released, the following parameters influence fertilization success: individual reproductive output, collective ratio of sperm and egg, the corresponding time period of the release. [150, 76]. On broader scale, synchrony may occur as a response to single or combinations of environmental issues such as lunar or tidal phases (e.g. [17, 81]), hydrodynamics (e.g. [121]), temperature (e.g. [98]) or food availability such as phytoplankton (e.g. [127]). In corals, we could see multi-species spawning synchrony and its resultant effect on fertilization rate. In fact, synchrony increases the chances of gametes meeting, enhances the possibility of outbreeding and may swamp opportunistic predators. (e.g. [81, 50]). Finally, although widespread correlations exist between spawning and various environmental cues, especially with lunar cycles, the physiological mechanisms behind such patterns are poorly understood [120].

There is experimental evidence confirming that chemotaxis plays a role in coral fertilization [15, 93, 94]. In this context, chemotaxis is the attraction of sperm gametes toward chemicals released by eggs. Chemotaxis has been mathematically studied in the context of mold and bacterial

colonies (e.g. [67]) and in coral broadcast spawning [68]. In proximity to eggs, sperm swim faster and orient towards the egg surface [112]. Sperm swimming velocities have been measured for several benthic invertebrates to be in the range of 0.05 to 0.3 mm/s [49, 80, 73, 112]. In typical turbulent benthic flows, since velocity fluctuations are on the scale of 0.01 m/s to 0.1 m/s and spawning adults are separated on the scale of centimeters or meters [29], it is likely that large-scale sperm motion is almost entirely passive [37]. It has been suggested that the action of sperm swimming and chemotaxis is unlikely to substantially increase egg-sperm collisions [74]. However, in proximity of eggs, sperm swimming and taxis might significantly increase contact rates [60] and the fertilization rate can be arbitrarily close to being complete provided that the chemotactic attraction is sufficiently strong [68].

Polyspermy, the fertilization of an egg by more than one sperm, is usually a negative condition which could impede the proper development of the zygote. Polyspermy risk may cause sexual conflict, in which traits that increase male reproductive success will simultaneously decrease female reproductive success. Modern efforts to model broadcast spawning fertilization rates incorporate effects of polyspermy [13, 128, 129, 92]. Polyspermy imposes a strong negative selective pressure. In situ rates of polyspermy in induced sea urchins reached 42% at high subtidal population densities [75] and up to 63% in tide pools [41]. However, for broadcasting marine algae, natural polyspermy levels are comparatively low (usually $< 10\%$) in intertidal [11], tide-pool [101] and subtidal habitats [122] .

Egg size can influence the success of fertilization. The importance of physical egg size was first investigated by Gerhard [146] who showed that increases in egg size enhance sperm collision frequency and final fertilization rates. Subsequent studies implied that the physical size of the egg cell could affect fertilization success [78, 87], although this effect may not be present in all species (e.g., [130]) or be important even in same species based on other studies (e.g. [107]). The outer cell structures surrounding many marine invertebrate eggs increase their effective size and might be a developing response to sperm limitation [73, 39]. However, the hydrodynamic effect of egg size on gamete coalescence and fertilization success is minimally known. In turbulent

or unsteady currents, finite-size particles do not precisely follow fluid paths [123], and particle size and/or differences in particle density relative to the local fluid density affect particle path deviations. These inertial effects are known to produce particle clustering [135, 38] and increases particle collisions [3]. Although egg size may be vital in some species, when sperm is limited other gamete traits such as chemotaxis, Jelly coats and fertilization efficiency are all important factors [120].

Gamete buoyancy can also be critical to reproductive success. Gamete buoyancy varies between species and influences gamete distribution within the water column. Sea urchin gametes are typically negatively buoyant [137, 151], with larger eggs sinking faster [77], whereas highly buoyant gamete bundles are seen in most mass spawning coral species [54, 53, 4], compressing gamete interactions into two dimensions at the sea surface. [100, 95] Such surface accumulation lowers dilution rates and increases the chances of egg and sperm encounter [99, 52, 16, 138]. Gamete buoyancy can also enhance fertilization success for some other type of species like anemone [119]. In general, floating particles are known to cluster due to effects of turbulence [118, 19], surface waves [27, 83], surface tension [124], or wind-induced langmuir circulations [71, 139], but the quantitative effect of these clustering mechanisms on gamete distribution and fertilization success is unknown.

1.2 Turbulent Mixing and Stirring in Gamete Flow

Fertilization success is affected by water motion in several ways. Motion is itself useful for mixing eggs and sperms, but higher velocity will lead to rapid sperm dilution and even damage to gametes or zygotes. The organisms with external fertilization have usually applied different strategies like synchronous spawning, high quantity and longevity of gametes and spawning in pairs or groups which all reduce the effect of water motion in fertilization rate [121]. The abundance of surge channels on a shore is strongly dependent on the local topography. Denny et. al [28] showed that exchange between surge channel and mainstream water is slow and local topography of each surge channel and chance variation in the shape of each breaking wave affects the mixing parameter. In fact, the fraction of eggs fertilized increases with the number of male presents in a

surge channel and also is independent of egg concentration.

The turbulent structures in the flow field can lead to coalescence between high-concentration filaments of freely spawned egg and sperm and enhance fertilization rates [21]. Release of gametes in viscous media (e.g. [132, 59, 151]) may enhance this process and substantially raise fertilization rates above those predicted for freely spawned gametes [21]. By contrast, turbulent transport models predict that suspension times for spores of most seaweeds are likely to be less than 1 week, and that their dispersal in typical nearshore currents is therefore limited to distances of several kilometers [45]. In shallow waters where wave-driven fluid motions extend to the substratum, the resulting back-and-forth surge increases bottom shear and alters the profile of vertical mixing. Typically, in the absence of a vegetation canopy and strong stratification, eddy diffusivities within a depth-limited current boundary layer, (such as is common in the nearshore) peak at middle depths [36, 45].

Little is known about the direct effect of structured flow and turbulence on gamete coalescence and dispersion at instantaneous time scales. Laboratory studies in a Couette cell [31, 90] show a modest increase in average fertilization rates at moderate turbulence levels (presumably due to increased contact rates), followed by a more dramatic fertilization decrease at higher turbulence levels (perhaps due to shear-induced damage to gametes). One of the characteristic of wave-swept shores in the aquatic environment is turbulent water motion. Gaylord [44] in his field study showed that viscous shear associated with strong turbulence leads to decreases fertilization success. He determined short and long-term energy dissipation rate, which have inverse relation with fertilization success. This study implied that characteristic of the time scales of gamete-turbulence interaction could be important in the field.

Flow-mediated spawning behavior has been studied primarily in fucoid algae [102] and kelp and green algae [48]. During high water motion periods, avoidance of spawning is a conserved response which results in high natural fertilization success (e.g.[121]). During gamete release under calm conditions, for photosynthesis there is diffusion-limited supply of dissolved inorganic carbon (DIC) that has been shown to act as a signal for gamete release [103]. In addition, in some fucoid

seaweeds, there are photoreceptors to specific blue and green light wavelengths which coordinate gamete release, and may contribute to restrict the release of gametes to calm intervals [104, 121]. There is not enough information on flow-mediated spawning behaviors of different marine invertebrates. However, several intertidal species are known to restrict spawning to periods of low tide such as gastropods [17], tunicates [86], and anthozoans [88]. Further investigation is required to find which spawning behaviors have been selected for different flow regimes.

1.2.1 Mixing of Multiple Reactive Scalars

Fertilization is treated as a bimolecular reaction between two scalar species (egg and sperm). The likelihood of an individual egg being fertilized is dependent on sperm concentration, and the resulting dimensional fertilization rate is kC_EC_S, where C_E and C_S are "virgin" egg and sperm concentrations, and k is a rate constant [30, 21, 22, 24].

Instantaneous gamete concentrations are governed by a coupled pair of reactive advection-diffusion equations that can be expressed as [24]

$$\frac{\partial C_E}{\partial t} = -U_i \cdot \nabla C_E + D_E \nabla^2 C_E - \Theta \tag{1.1}$$

$$\frac{\partial C_S}{\partial t} = -U_i \cdot \nabla C_S + D_S \nabla^2 C_S - \Theta \tag{1.2}$$

where D is diffusivity of scalar and $\Theta = kC_EC_S$ is the dimensional form of the fertilization rate. Using a standard Reynolds decomposition (e.g., reference [1]), the local gamete concentrations can be decomposed into the sum of a mean component (denoted by $<>$) and a fluctuating component relative to the mean (denoted by a prime): $C_E =< C_E > +c'_E$, and $C_S =< C_S > +c'_S$. By substituting these decompositions into the expression for Θ and then averaging, the averaged value (inclusive of instantaneous physics) of the normalized fertilization rate Θ/k is then [22]

$$< C_EC_S > = < C_E >< C_S > \; + \; < c'_Ec'_S > \tag{1.3}$$

where the first term on the RHS is simply the product of the average concentrations, and the

second term is the correlation between the fluctuating concentrations. Extant fertilization models consider only the effect of the mean concentrations (first term in Eq. 1.3). Present work aims to understand the role of instantaneous processes (second term in Eq. 1.3) on the success of the broadcast spawning strategy.

1.2.2 Length Scales of Turbulence

Length scales are commonly used to describe turbulent fields and these scales relate to the scales of concentration gradients described above as well as eddy sizes. These scales range from the size of the largest structures found within the flow to the size of the smallest structures where eddies dissipate to heat. The integral length scale is an approximate measure of the largest eddies found within the flow and is usually assumed to be on the order of half of the flow depth. The dissipation of turbulent kinetic energy to heat occurs at what is called the Kolmogorov microscale:

$$\eta = (\frac{\nu^3}{\epsilon})^{\frac{1}{4}} \tag{1.4}$$

where ν is the kinematic viscosity of the fluid and ϵ is the dissipation rate of the turbulent kinetic energy. This microscale is not exact but rather an approximation of the smallest eddy sizes. As stated above, molecular diffusion acts to smooth the steep concentration gradients at a small length scale. The scale at which this occurs is referred to as the Batchelor length scale:

$$L_B \approx (\frac{\nu D^2}{\epsilon})^{\frac{1}{4}} \tag{1.5}$$

in which D is the molecular diffusivity of the substance being stirred in the flow. The Kolmogorov and Batchelor length scales are related:

$$\frac{\eta}{L_B} \approx S_c^{\frac{1}{2}} \tag{1.6}$$

where the Schmidt number, S_c, is defined as $\frac{\nu}{D}$.

1.3 Present Study

One of the most common methods of reproduction in the sea is broadcast spawning: a process through which marine invertebrates (e.g. sea urchins, sea anemones, corals) release eggs and sperm into the ambient flow and fertilization occurs externally. Gamete coalescence on a large scale is dominated by fluid stirring, and may be influenced by the presence of flow obstructions (e.g., coral heads, bed topography). Mixing and reaction between these scalars initially separated by scalar-free ambient fluid is important in problems ranging from ecology to engineering, but is relatively unstudied compared to the more common topology where the two scalars initially share a material interface.

The present research aims to determine the effect of key physical and biological factors on the fertilization rate associated with broadcast spawning in benthic invertebrates. Specifically, the research objectives are to answer the following questions:

1. What is the effect of unsteady flow phenomena typical to benthic and reef environments (e.g., wakes behind obstacles) on fertilization success?

2. What is the effect of instantaneous turbulence structure (e.g., vortices, integral length scale) on gamete coalescence and subsequent enhancement of fertilization rates?

3. How do physical and behavioral gamete traits (e.g. viscosity, non-Newtonian rheology, morphology) alter the mixing process and ensuing fertilization rates?

Using a combination of analytical work and laboratory experiments, we show that turbulence imparts spatial correlations on two initially distant passive scalars, resulting in mixing enhancement. This phenomenon has never been reported in the fluid mechanics literature, and it has important consequences for a range of engineered and ecological systems, including broadcast spawning.

Chapter 2

Experimental Methodology and Equipments

2.1 Flow Facilty

Figure 2.1: The Benthic Turbulence Facility in the Environmental Fluid Mechanics Laboratory

The experiments were conducted in the recirculating benthic boundary layer flume (Fig. 2.1) in the Environmental Fluid Mechanics Laboratory at the University of Colorado at Boulder. The flume test section is 9 meters long and 1.25 meters wide. The facility features a highly configurable setup for comparison of specific depth and flow conditions. It is also fitted with a plunger-style wavemaker to make surface waves with different amplitudes and frequencies (Fig. 2.2); however, waves were not used in the present study. At the end of the test section, various size weir plates are used to adjust the running flow depth. The mean flow velocity and turbulence intensities can be varied, and the flume can be configured with or without bed roughness, flow obstacles, and surface waves. The walls and bed of the flume are glass, which is suitable for non-intrusive optical measurement techniques.

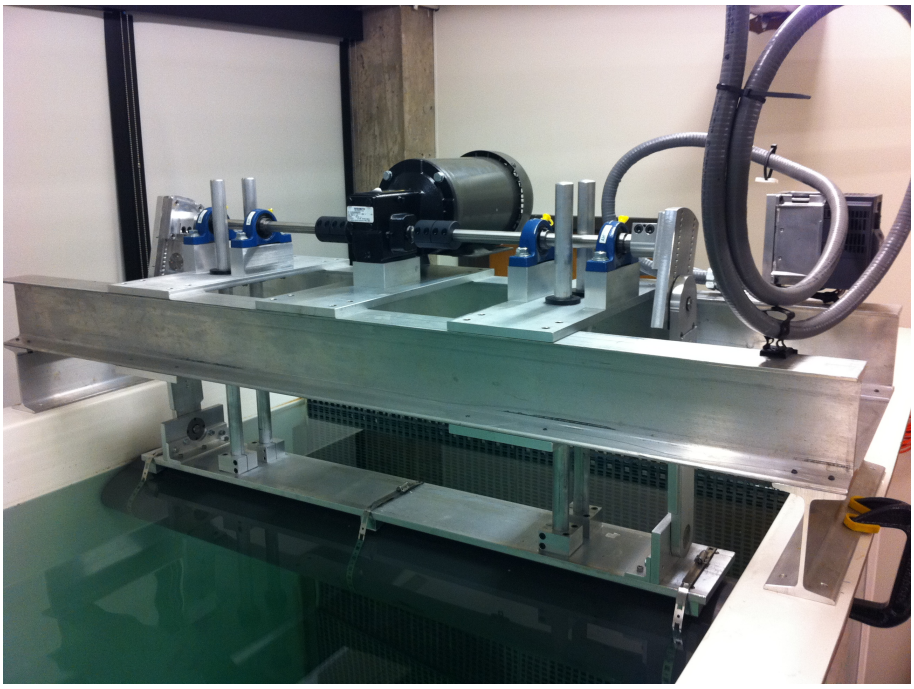

Figure 2.2: The vertical wavemaker

2.2 Laser Doppler Velocimeter (LDV/LDA)

The laboratory has a Dantec Dynamics 2-component (u,w) fiber optic LDV system (Fig. 2.3) with a 112 mm diameter probe, and uses a BSA F60 processor running Flow Software version 4.0. The probe has an 800 mm focal length with an expansion ratio of 1.5, producing a measurement volume 0.080 mm in diameter and 1.17 mm in length. The LDV probe contains both transmitting and receiving optics, and operates in backscatter mode. It is mounted on a three-dimensional automated traverse that is controlled through the BSA software. The LDV is driven with 750 mW of argon-ion laser power [33].

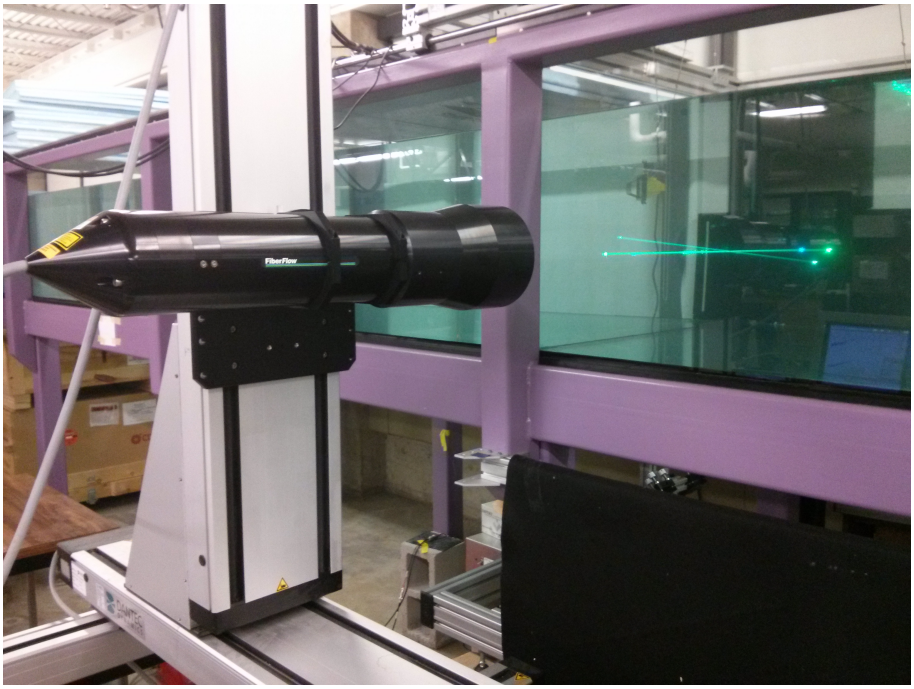

Figure 2.3: The Dantec Dynamics two-component (u,w) LDV probe and traverse system at the University of Colorado.

2.3 Two-Channel Planar Laser-Induced Fluorescence

The laboratory has high-quality imaging equipment, lasers, and optics to perform flow visualization studies. The complete imaging system is comprised of custom components driven by a combination of digitally-controlled interfaces, software packages, and user-generated voltage signals. The primary components of the high-quality imaging system are:

Laser: Coherent Innova 90C 5-Watt 488 nm argon-Ion, and Coherent Innova 90C 5-Watt 647.1nm krypton-Ion. Operated in TEM00 mode. Both water cooled.

Cameras: IMPERX digital C-Mount, 1393 x 1040 pixels resolution at 30 fps

Lenses: 25mm Fujinon HF25SA-1

Signal control computer: Windows 2000, LabView 9.0, National Instruments PCI-6733 DAQ card, and National Instruments BNC-2110 breakout box

Image acquisition system: Windows XP, Quazar software, 2 TB total hard drive capacity

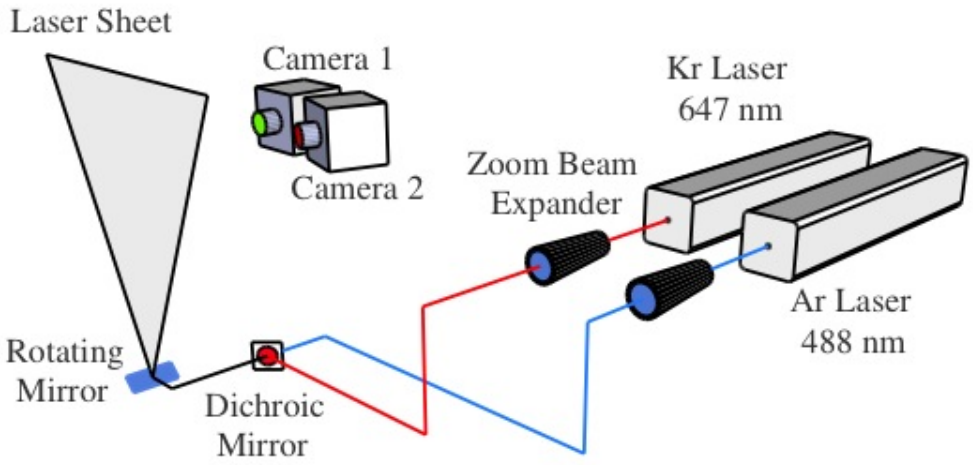

Figure 2.4: Schematic of two-channel planar laser Induced fluorescence system, Soltys and Crimaldi [125]

A novel two-color planar laser-induced fluorescence (2C-PLIF) system [125] has been used to quantify the spatial and temporal dispersion and coalescence of gamete surrogates released in the flume. The gamete plumes advect downstream to the measurement region, where they are illuminated by a thin (100 μm) bispectral laser sheet comprised of two colors of light from argon and krypton lasers. Egg and sperm surrogates each fluoresce light at different wavelengths, with an intensity (under appropriate conditions) proportional to local concentration. According to test location, two different size regions, each region is simultaneous imaged by two 12-bit IMPERX digital cameras, each fitted with a narrow-band filter that passes only one of the two fluoresced wavelengths. Time series of 12-bit, 1393 x 1040 pixel images are recorded at up to 10 Hz from

each camera, one corresponding to egg concentrations, and one to sperm. For a typical experiment, approximately 5000 images at $0.4 \sim 0.8$ Hz are recorded, for each scalar. Data is streamed live to a 1Tb image acquisition system (Quazar, Boulder Imaging). Images from each camera location are mathematically mapped onto a common image plane to remove parallax effects, ensuring accurate (less than 0.5 pixel) spatial correspondence between egg and sperm image pairs[125, 20]. An image processing algorithm calibrates the images and corrects them for errors caused by background fluorescence, variations in the laser scan intensity, attenuation due to background dye, lens vignette, camera pixel response variations and camera dark response (Fig. 2.5). Here a brief description of each PLIF component is presented:

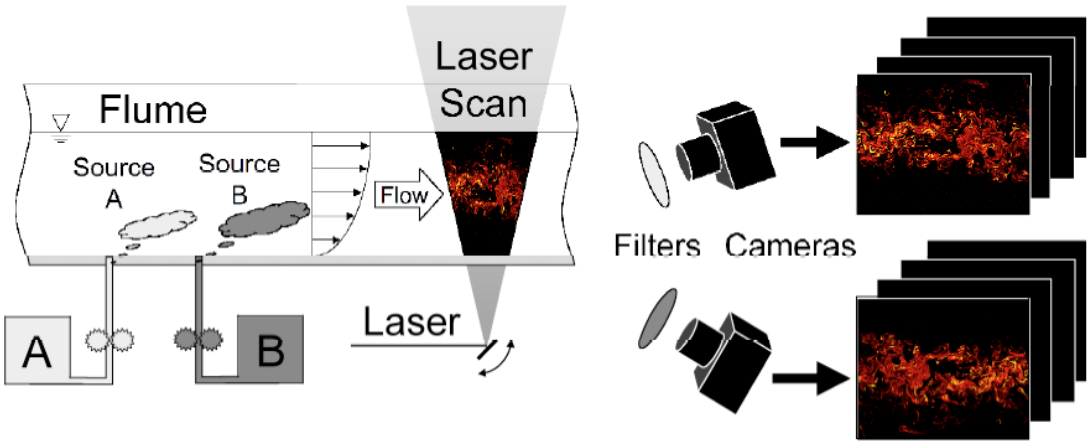

Figure 2.5: Schematic of the test section and two-channel PLIF system

2.3.1 Dyes

Two dyes (Fluorescein and Oxazine 725) were used for the two-color PLIF experiment. According to Table. 2.1 the fluorescein peak absorption wavelength was 491 nm and peak emission wavelength was 514 nm. Similarly, the oxazine 725 peak absorption wavelength was 656 nm and peak emission wavelength was 668 nm (Fig. 2.8). Once in solution, all dyes were stored in the dark to minimize absorption of light [125, 20].

Table 2.1: Measured Properties of Fluorescein and Oxazine 725 in Aqueous Solutions [125].

Dye	Peak Abs. [nm]	Peak Em. [nm]	ϵ [cm^{-1} M^{-1}]
Fluorescein	491	514	1.40e5
Oxazine 725	656	668	2.33e5

2.3.2 Dye Delivery

For PLIF experiments dyes were released from two 0.56 cm diameter nozzles held firmly in place by acrylic strings attached to ceiling. For the two-color PLIF system, two mounting nozzles were located symmetrically about the flume centerline with spanwise separation of 2.41 cm. Tygon tubing connected the fluorescein nozzle to a gear pump with a maximum flow rate of 330 mililiter per minute. A 8-gallon open-top polyethylene container was used to hold the source dye, connected to the gear pump. The height difference between pump and flume was about half a meter, well within the limits of the pump. Another 8-gallon bucket was placed in the laboratory about a meter below the flume, and a tygon tubing connected the bucket to the second nozzle. A valve was located just below the bucket along the tubing line to allow easy control of the source flow rate. Pump calibration is performed to control the flow from each nozzle to create an isokinetic release in the flume flow.

2.3.3 Computers

Two computers were used to perform the experiments. One was equipped with National Instruments LabVIEW software to create timing signals and to synchronize the data collection process. A National Instruments multipurpose module was connected to this computer and controlled all voltage input and output. Another computer was used for image acquisition from two cameras. This computer was equipped with eight 250 GB hard drives each configured in a RAID array to ensure that data was not lost or corrupted. This computer was equipped with Quazar

image capturing software (Boulder Imaging Corp.) which adjusted the hard drive writing speed, in relation to the image capture frequency, limited the bandwidth for image capture.

2.3.4 Software

Two custom LabVIEW VIs were created for performing experiments. One VI synchronized a digital-to-analog output channel for the scanning mirror for the image capture signal of a camera. The other VI synchronized the same analog output channel with counter output channels, for two cameras. Each VI had adjustable voltage limits for the analog output channel in order to adjust the width of the x-axis scanning mirror sweep as well as adjustable frequency for the scanning mirror sweep rate and signal for image capture (Fig. 2.6). The Quazar software was used to adjust the image exposure time period and set storage parameters of the captured image files.

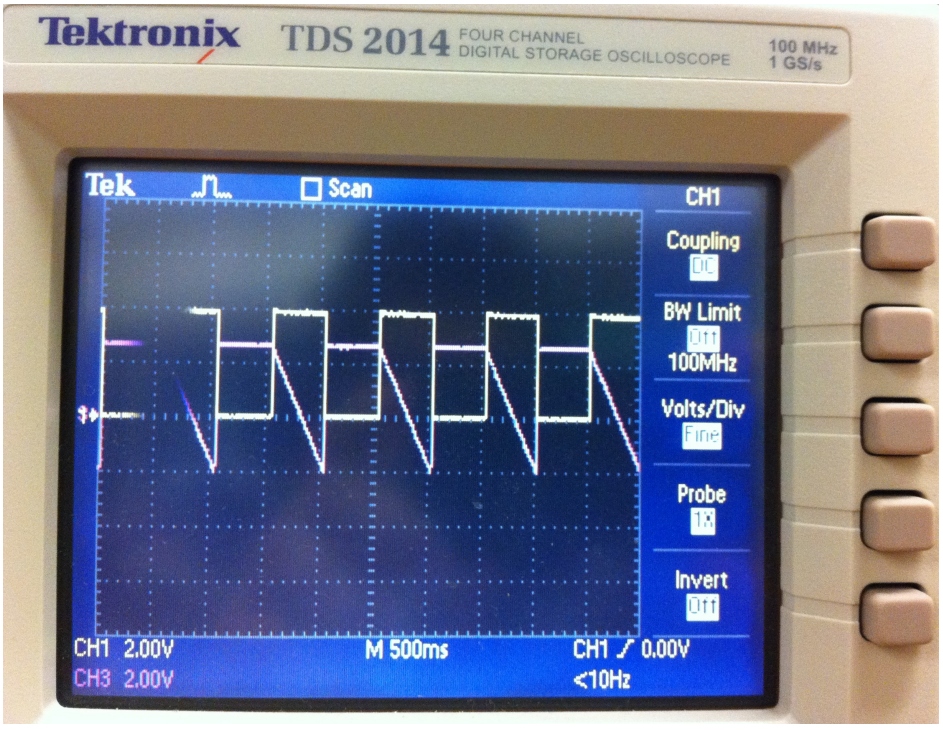

Figure 2.6: View of running LabVIEW signal on four channel oscilloscope monitor

.

2.3.5 Scanning Mirrors

One scanning mirror is mounted on an aluminum block attached to frame under flumeside. The x-axis mirror rotated to reflect the laser beam in the horizontal direction creating a sheet of light. A second axis (y direction) was designed to allow for three dimensional LIF by moving the reflected beam(s) left and right. This mirror, however, was fixed for all experiments. The control signal was sent from the National Instruments module to the scanning mirrors via a control and power unit (Fig. 2.7).

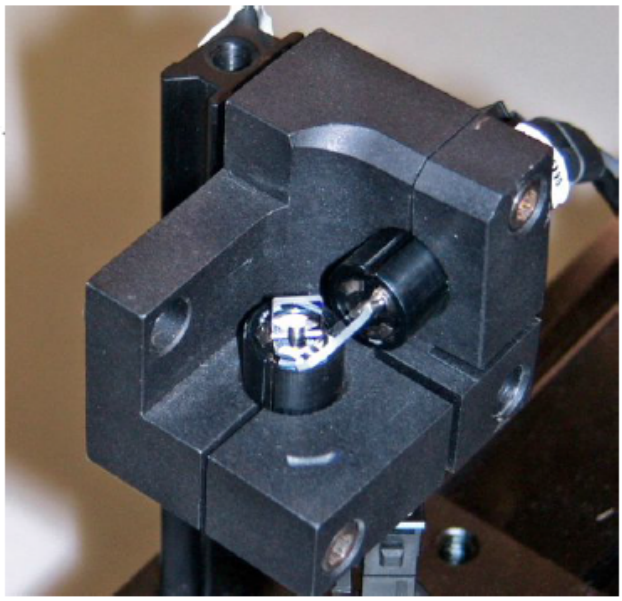

Figure 2.7: Image of dual scanning mirrors with aluminum mounting block.

2.3.6 Cameras

Two digital cameras (IMPERX Corp.) were used for the two-color PLIF experiments. These CCD cameras captured images at a resolution of 1393 pixel width and 1040 pixel height and a total of 1.5 megapixels.

The Oxazine 725 camera was centered and mounted to a support frame beside the flume on an adjustable stage. This camera was moved half its width to one side and the second camera was mounted next to it so that the cameras were symmetrically slightly off-center beside the flume's

glass wall.

2.3.7 Camera Filters

Two filters were used, one for each camera, in order to filter out unnecessary light and allow only the fluoresced light of each dye to be captured. The camera for the fluorescein was fitted with a band pass filter allowing only light in the range of 511 to 559 nm wavelength to pass through. The camera for the oxazine 725 had a long pass filter to pass light above 660 nm. Each filter was attached to a adapter ring that is fitted to the lens of each camera [125, 20].

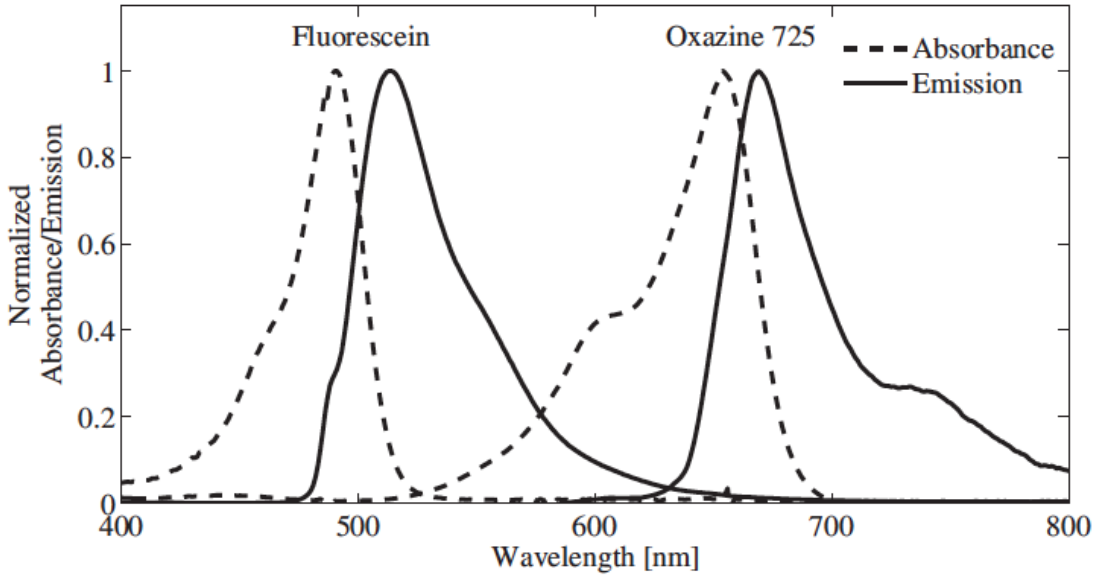

Figure 2.8: Normalized absorption/emission spectra for fluorescein and oxazine 725 in aqueous solution [125]

.

Chapter 3

Experimental Investigation Of The Effect Of Unsteady Obstacle Wakes On Stirring And Mixing Of Gamete Filaments

3.1 Introduction to Cylinder Wake Mixing

In aquatic ecosystems, structured flow such as a cylinder wake, can facilitate stirring and subsequent diffusion of transported scalars. Structured stirring can enhance population growth of the system, by bringing together species and nutrients [110]. Moreover, structured flow contributes directly to the coexistence of species competing for a resource [64]. Flow becomes structured as it advects past benthic topology, such as sea-mounts, and can be dominated by a vortex street causing mixing [111].

The flow environment in spawning regions can be influenced by unsteady vortex shedding in wakes behind obstacles [40, 51]. The obstacles can be the animals themselves (e.g. urchins, coral heads), or local bed topography. Unsteady wakes (e.g., Karman vortex streets) behind flow obstacles serve as effective reactors for bimolecular reactions [66, 143, 63]. Obstacle wakes alter scalar structure [109] and produce clustering of inertial particles [135, 57]. The effect of these unsteady flow phenomena on gamete coalescence and fertilization rates is unknown. Results shown in Sec. 3.3 suggest that obstacle wakes produce significant reaction enhancement.

Over a broad range of scales, bluff-body wakes or cylinders wakes are universal in natural and engineered systems. At small scales, cylinder wakes are used as microfluidic reactors to mix chemicals [32, 147]. At large scales, higher mixing and reaction are observed by wakes behind oceanic islands [58, 34, 35] with ecological implications on nutrient distributions [55] and phyto-

plankton dynamics [114, 56]. Mixing and reactions in a cylinder laminar wake have been studied both in the biological context of species competition and coexistence [116, 117] and in the general context of nonlinear dynamics [62, 152, 136]. Previous numerical studies also looked at mixing and reactions in downstream wake region [42, 14, 23]. At laboratory scales, particularly for turbulent flows, mixing and reactions behind cylinders have been studied experimentally [12, 65, 91].

In cylinder mixing, the Reynolds number describes the flow regime. A flow with $Re < 1$ is a Stokes flow in which the velocity of the fluid typically is very slow, or the length scale is very small. The shear layers do not separate as this flow passes around a cylinder. As Re increases, a wake begins to develop behind the cylinder, more quickly in the lateral direction than streamwise [18] and a pair of fixed vortices develop immediately behind the cylinder[131]. At $Re \sim 40$, instabilities in the wake cause the attached vortices to alternately detach and advect downstream forming a vortex street[144]. At $Re \sim 100$, the vortices begin to shed periodically[144]. Diffusion of vorticity is no longer the primary factor in determining vortex strength and frequency, and there are no standing vortices as convection begins to overwhelm diffusion near the cylinder[46]. The flow transitions to turbulent at the critical Re, $200 < Re < 300$, and as Re increases, the formation region length decreases[10]. In the turbulent regime, $Re > 300$, turbulence in the incoming flow has a significant effect on the variation of Strouhal number with Reynolds number[131].

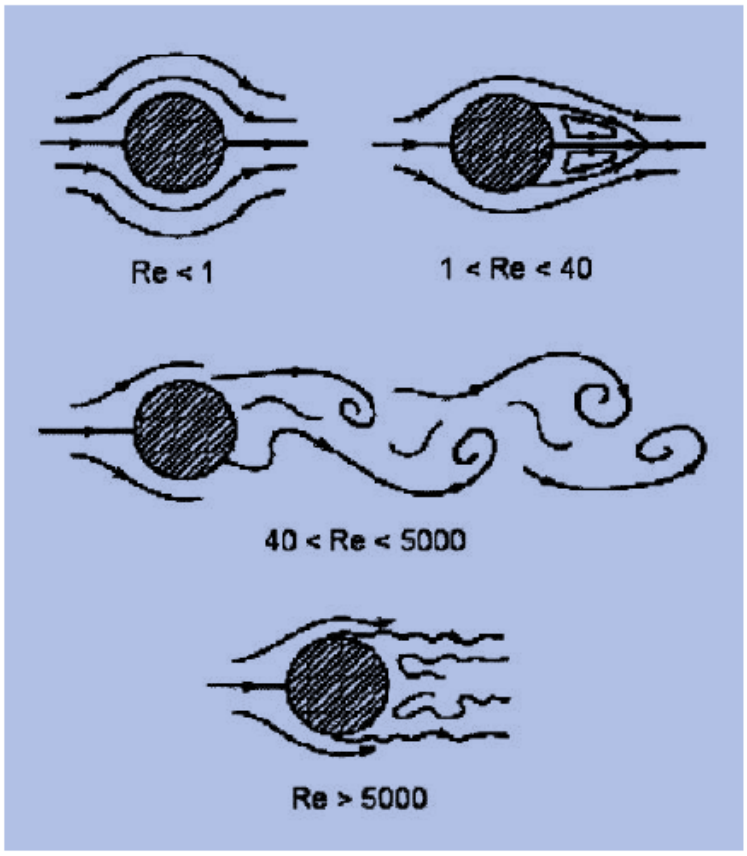

Figure 3.1: The cylinder wake shape with variation of Reynolds number

In cylinder mixing, Reynolds numbers can be defined by both the cylinder diameter size, $\tilde{\phi}$

$$Re_{\phi} = \frac{U\tilde{\phi}}{\nu} \tag{3.1}$$

or grid mesh size, $\tilde{M}$:

$$Re_{M} = \frac{U\tilde{M}}{\nu} \tag{3.2}$$

where ν is water viscosity and U is velocity of flow.

Using broadcast spawning as motivation, the current study investigates how the turbulent wakes behind a circular cylinder can promote coalescence between initially distant scalars (sperm and egg gametes) to facilitate reactions. There is a dearth of research on the effects of these unsteady flow phenomena on gamete coalescence and fertilization. The research suggests that the

cylinder wake greatly enhances the fertilization and reaction rate in gamete coalescence.

3.2 Experiment Setup

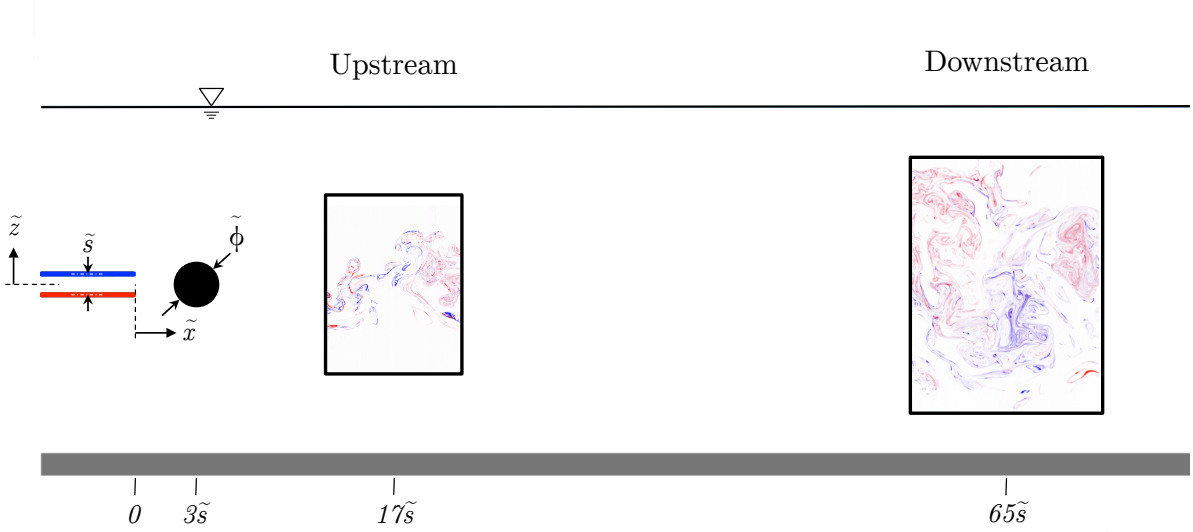

Figure 3.2: Experimental configuration showing the location of the scalar release tubes, cylinder, and upstream and downstream measurement locations. The cylinder diameter, $\tilde{\phi}$, spacing, $\tilde{s}$, as well as the coordinate axes, are denoted here. The grid and honeycomb are located in $27\tilde{s}$ and $50\tilde{s}$ upstream of release tubes, respectivel

The experimental setup to create a pair of initially distant plumes in a cylinder wake is shown schematically in Fig. 3.2. In order to create homogenous isotropic turbulence, a wire mesh with wire diameter $\tilde{d} = 0.55$ cm and square mesh openings $\tilde{M} = 3.18$ cm was used. The grid was placed 0.56 m downstream of a flow-straightening honeycomb, which it is located 1.5 m downstream of transition between fiberglass and glass at the entrance to the flume. The grid covers the entire width and depth of the flume.

Table 3.1: Experiment Setup

	$Re_\phi = 2000$	$Re_\phi = 2000$	$Re_\phi = 5000$
Upstream	With Cylinder	No Cylinder	-
Downstream	With Cylinder	No Cylinder	With Cylinder

3.2.1 Cylinder Wake Mixing Experiments

For the cylinder wake experiments, one cylindrical PVC pipe with diameter of $\tilde{\phi} = 4.826$cm was used to produce unsteady obstacle wakes in flow. A total of five experimental configurations were considered in one nozzle spacing ($\tilde{s} = 2.41$ cm) at two upstream ($\tilde{x} = 34 - 50$ cm) and downstream ($\tilde{x} = 146 - 170$ cm) locations for two flow regimes (i.e., $Re_\phi = 2000$ and $Re_\phi = 5000$).

Additional data was taken for the $\tilde{s} = 1.20$ cm nozzle spacing at low Reynolds number in downstream location to help understand the effect of nozzles spacing on cylinder wake mixing. Accurate measurement were taken by LDV in the flow test section. Two flow velocities of 4.05 cm/s and 10.05 cm/sec with temperature held at 21.5 C yielded $Re_\phi = 2000$ and $Re_\phi = 5000$ for cylinder case and $Re_M = 1600$ and $Re_M = 4000$ for non-cylinder case. The pulseless gear pumps were used to inject the scalars to flow. Those pumps were calibrated to match the flume velocity for an isokinetic release [125].

In order to allow plumes to have well developed turbulence, scalars were released 65 cm downstream of the turbulence generating grid. Another injection system was designed separately to measure the full strength dye concentration to scale the scalar dye concentration for the upstream and downstream data set. For cylinder case, the distance of nozzles to cylinder is an order of pipe diameter size (i.e., $\tilde{\phi} = 4.826$ cm). The scalars were introduced using 2.75 m copper tubing with 0.56 cm diameter to ensure a well developed flow profile and remove temperature fluctuations from the dye release. Once the scalars are released into the flow, they advect with the developed flow field past the cylinder and into the vortex street. The presence of cylinder and associated wake increase the coalescence of the scalar, and produces higher reaction rate.

In order to measure the reaction, we use conservative scalars, and then compute the scalar

overlap term C_1C_2 digitally after-the-fact, and that this scalar overlap term approaches the non-dimensional reaction in the low-Da limit. The images are re-combined into a single image with the color map shown in Fig. 3.3. The color map uniquely displays concentrations of the individual scalars, as well as any combination of the two. The concentration of the lower plume, C_1, is shown in varying tints of red, while the upper jet, C_2, is shown in varying tints of blue. Ambient fluid is shown as white, and any mixture of C_1 and C_2 is displayed as a unique hue of purple. All possible mixtures are contained in the triangular region of colormap in Fig. 3.3.

An instantaneous composite image of an x-z slice through the cylinder wake system is shown in Fig. 3.3. The colormap for this process appears beside each plot to give us more sense about values. The purple filaments represents regions where mixing and overlapping occurred. Turbulent stirring brings the filaments together and continues to stretch and fold the scalar fields until molecular diffusions start to bridge the barrier of ambient fluid.

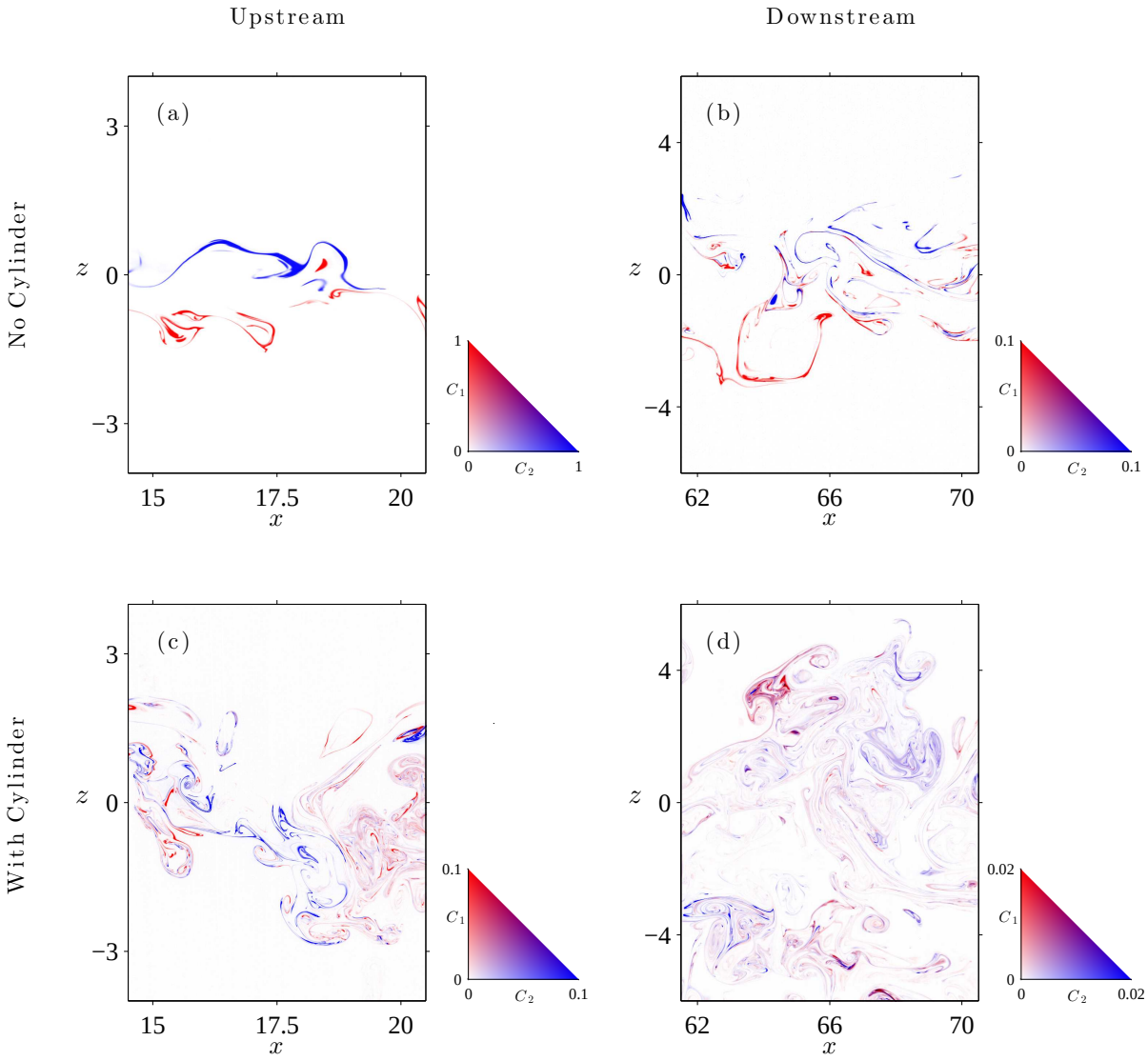

Figure 3.3: Instantaneous distributions of concentrations C_1 and C_2 at the upstream and downstream locations are shown. The top row stands for flow without the cylinder, and the bottom row depicts flow with the cylinder. The color scheme for C_1 (shades of red), C_2 (shades of blue), and various combinations of the two (shades of purple) is illustrated correspond to each case.

Table 3.2: The setup parameters and flow conditions for LDV experiments

	Low Re With Cylinder	Low Re Non-Cylinder	High Re With Cylinder	High Re Non-Cylinder
Water Temperature ('C)	21.8	21.5	21.8	21.5
Static Water Depth (mm)	370	370	370	370
Flow Depth (mm)	501.5	501.5	487.5	487.5
Weir Height (inch)	18	18	16	16
$U_o(cm/sec)$	3.94	3.94	9.52	9.52

3.2.2 Laser Doppler Velocimetry Experiments

The basic premise of the LDV/LDA technique is measurement of particle velocity within a volume formed by the intersection of laser beams. The technique is nonintrusive; the entire system resides outside the flow regime, taking advantage of the glass walls of the flume. The system components make the technique well-suited for highly resolved turbulence measurements in laboratory environments. The LDV system components include an Argon-Ion laser, fiber-optic cables and coupling hardware, transmitting and receiving optics, three-dimensional traverse with stepper motor, signal processing computer, and software for user interface. The size, complexity, and power requirements of the LDV system makes the technique generally impractical for field use. LDV velocity measurements rely on light scattered from a measuring volume formed by the intersection of two or more laser beams. The intersecting beams create a pattern of interference fringes, and the calibration of the instrument is based on the spacing of the fringes.

The flow tests were conducted at two flow settings ($U_o = 4.05$ cm/s and $U_o = 10.05$ cm/s) in two locations ($\tilde{x} = 42$ cm and $\tilde{x} = 150$ cm) with and without cylinder obstacle in flume. Table 3.2 contains the setup parameters and flow conditions for each recorded data set. Twenty-minute sample records from each point in the flow were used to produce profiles of velocity and calculate turbulence statistics. The LDV profiles consisted of 9 points spaced linearly and symmetric to middle of nozzle spacing ($z = 0$) from 3.6 cm to 46 cm above the bed. The sampling time is designed to be long enough to ensure sufficient statistical convergence. The seeding particles used for the LDV are Polyamid Seedings Particles (PSP) with diameter size of 5μm. The flow depends only

on temperature, flow depth, and pump settings, the latter two of which are precisely controlled. Temperature effects are very minimal and are removed in the nondimensionalization scheme by using a temperature-dependent value for the kinematic viscosity ν.

3.3 Results and Discussion

Time averaged distributions of concentrations C_1 and C_2 at the upstream and downstream locations are shown in Fig. 3.4 for two locations and for the cylinder and non-cylinder cases. The average plume spreads linearly and it is symmetric across the centerline between the nozzles ($z = 0$). In the cylinder cases, the obstacle wakes produce large dispersion and mixing entire the depth of flow. As the vortices shed and advect, the scalars are drawn downstream, increasing the interfacial length between scalars, facilitating diffusion and increasing the mixing.

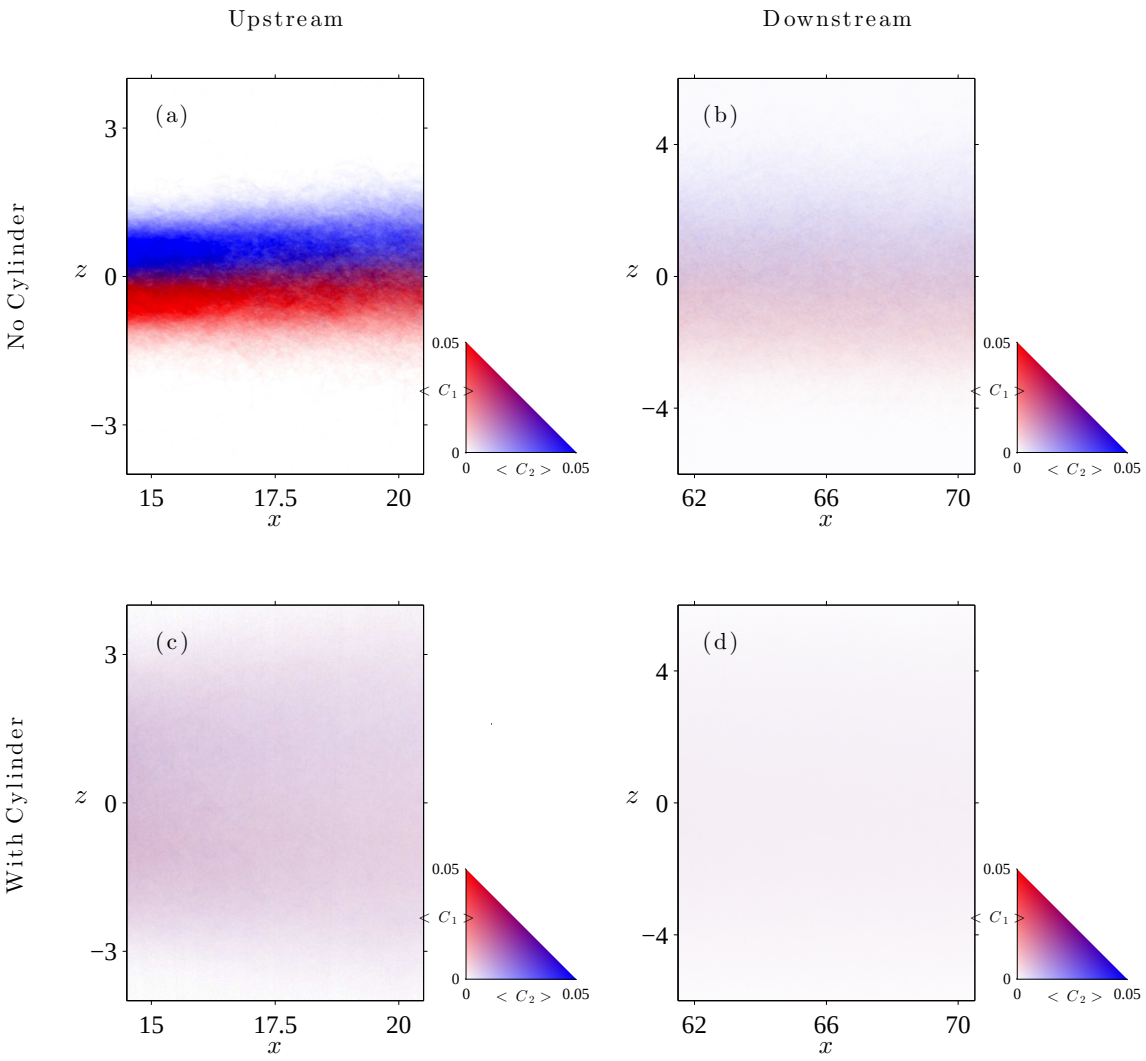

Figure 3.4: Time averaged distributions of concentrations C_1 and C_2 at the upstream and downstream locations shown in Fig. 1. The top row is for flow without the cylinder, and the bottom row is with the cylinder. The color scheme for $< C_1 >$ (shades of red), $< C_2 >$ (shades of blue), and various combinations of the two (shades of purple) is shown for each case.

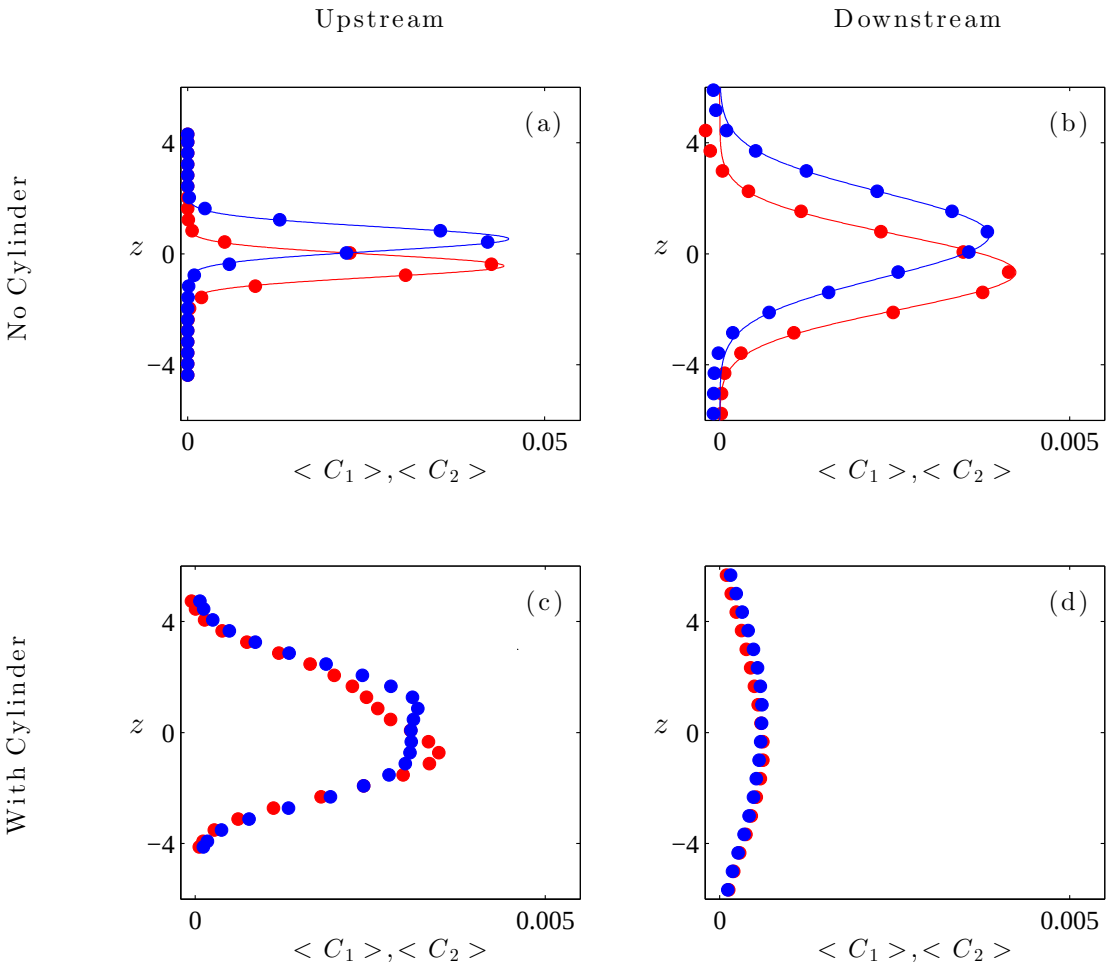

Figure 3.5: Profiles of average concentrations $< C_1 >$ (red) and $< C_2 >$ (blue) corresponding to the four cases shown in Fig. 3.3. Solid lines in top figures are the Gaussian profiles fit to average concentration profiles. Note that the concentration scale is an order of magnitude lower for the top right and bottom row relative to the top left row.

Profiles of the time-averaged non-dimensional plume concentrations at upstream and downstream locations are shown in Fig. 3.5. Each point represents a bin of 75 pixels in z direction, averaged spatially in x and then normalized to full strength dye concentration. The mean profiles are Gaussian and symmetric along the centerline ($z = 0$) for the non-cylinder case. In cylinder case, the averaged plumes are symmetric, but not completely Gaussian, with a slight skew due to

the entrainment of the two plumes towards each other, especially in upstream location.

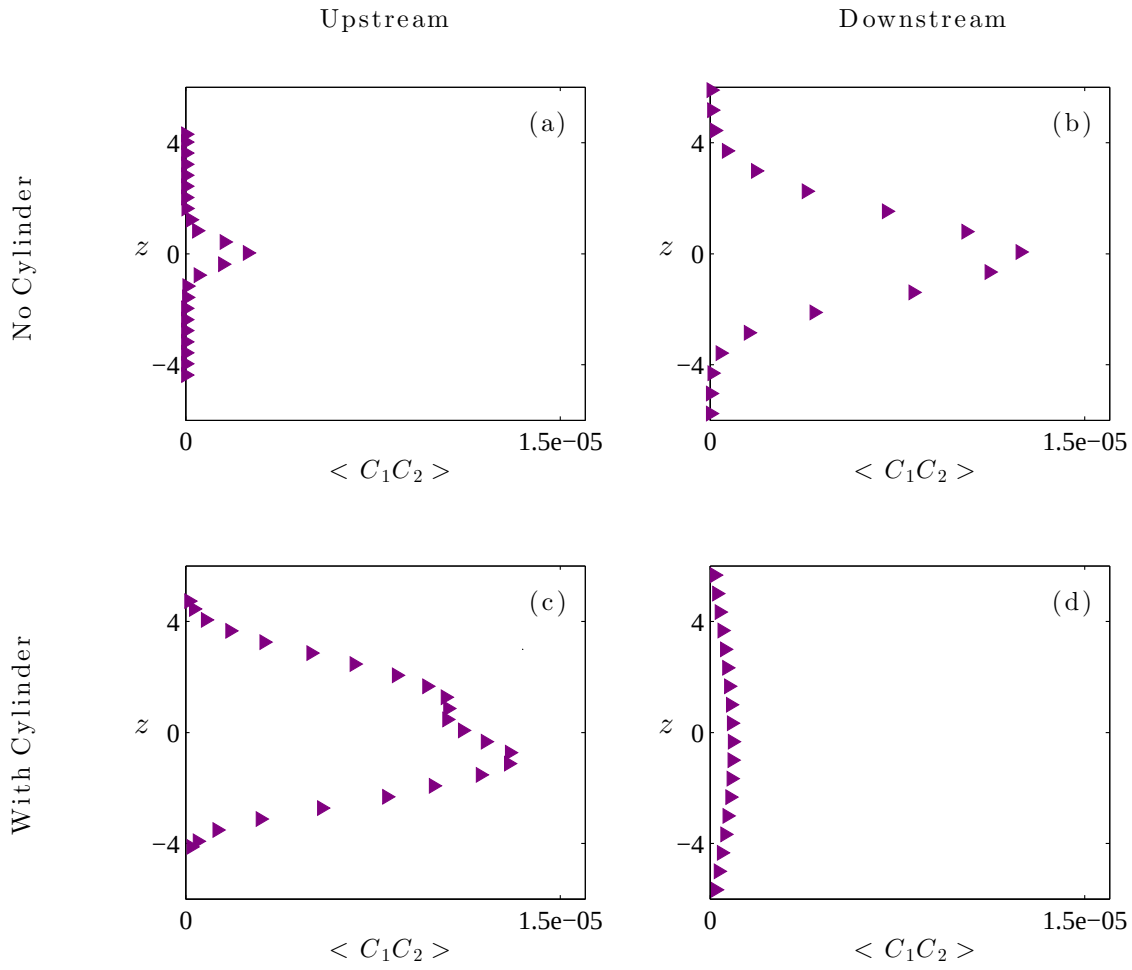

Figure 3.6: Profiles of average scalar overlap $< C_1C_2 >$ corresponding to the four cases shown in Fig. 3.3

The total non-dimensional simulated reaction product, $\langle C_1C_2 \rangle$ shown in Fig. 3.6. In non-cylinder case, the reaction plume exhibits a Gaussian cross-section and symmetric along the centerline ($z = 0$). The mean scalar fields are spread across the domain, which represents well the transport of scalars in grid turbulence. However, in the upstream location, the cylinder wake mixing is significantly larger than mixing in the corresponding no-cylinder flow.

The presence of the obstacle wake generates significant mixing enhancement by increasing

the rate of stretching and folding of filaments in direction of flow. In the downstream location, low estimates of reaction result from rapid dispersion of scalars with distance from the main source.

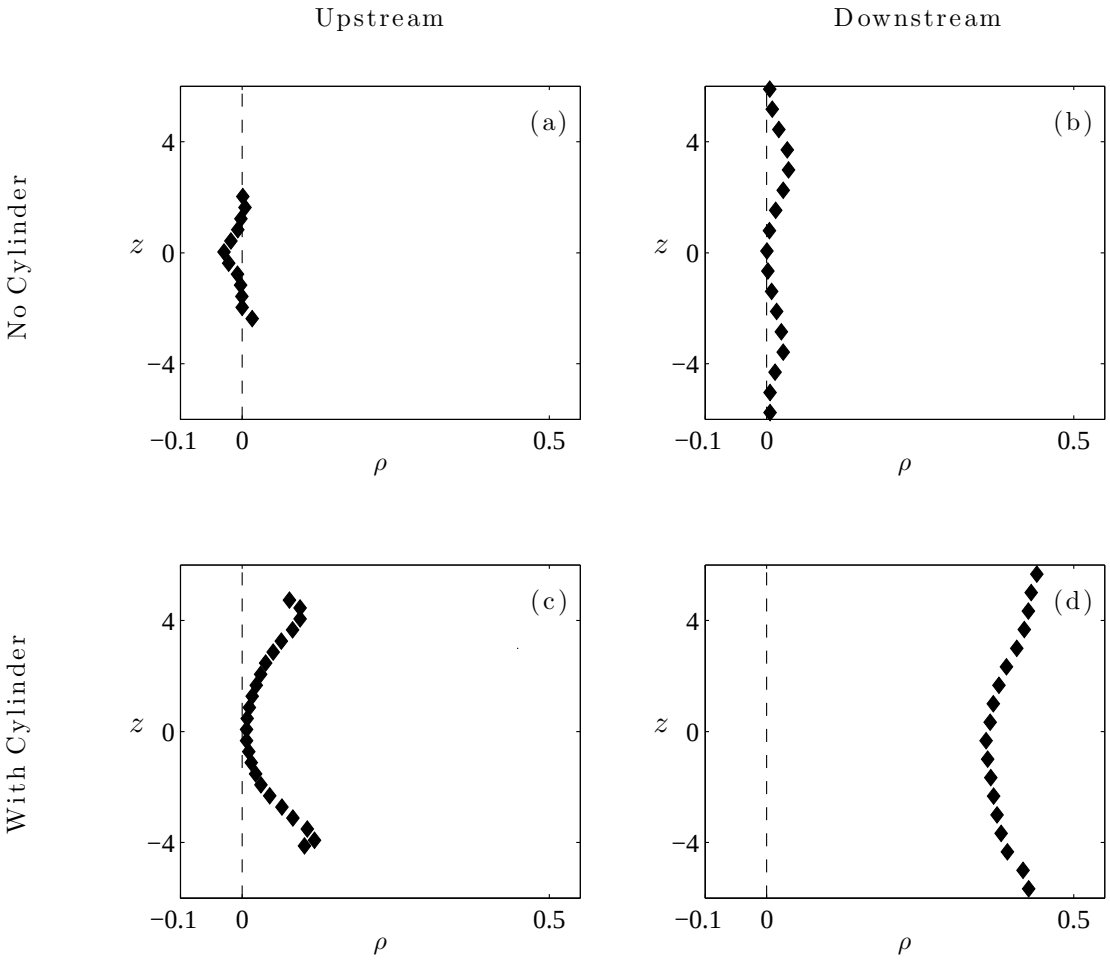

Figure 3.7: Time averaged Pearson's correlation coefficient profiles corresponding to the four cases shown in Fig. 3.3

As discussed in section 2.2 the mean local mixing parameter, $< C_1\, C_2 >$, can be decomposed as:

$$< C_1 C_2 > = < C_1 >< C_2 > \; + \; < c_1' c_2' > \tag{3.3}$$

where the two terms on the RHS correspond to contributions from the mean and fluctuating concentration fields, respectively. To understand instantaneous processes, the covariance term $\langle c_1' c_2' \rangle = \langle C_1 C_2 \rangle - \langle C_1 \rangle \langle C_2 \rangle$ is examined. Figure 3.7 shows the covariance normalized as the Pearson's correlation coefficient, ρ,

$$\rho = \langle c_1' c_2' \rangle / (\sqrt{\langle c_1' \rangle^2} \sqrt{\langle c_2' \rangle^2}) \tag{3.4}$$

over the entire experimental domain for four experimental setups. In non-cylinder case, at upstream there are negative correlations in corner due to the lack of C_1 and C_2 and small positive values in the middle of domain. At downstream, the mean plumes begin to overlap and positive correlation occurs in corner. In cylinder case, as obstacle wake processes continue to stretch and fold the scalar fields, we see the overlap of diffused filaments over the entire domain.

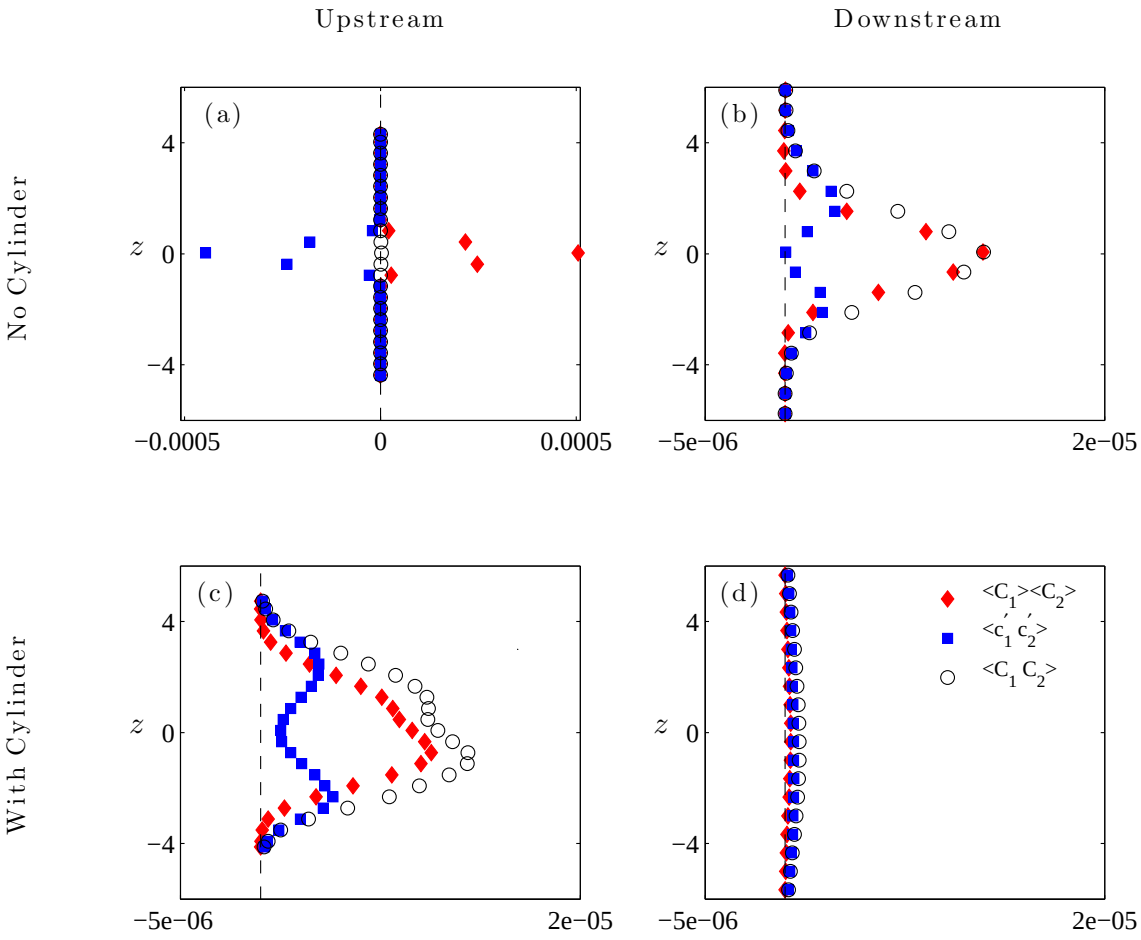

Figure 3.8: Non-dimensional profiles of ♦ $\langle C_1 \rangle \langle C_2 \rangle$, ■ $\langle c_1' c_2' \rangle$, and ∘ $\langle C_1 C_2 \rangle$ for corresponding to the four cases shown in Fig. 3.3. Note that the scale is an order of magnitude lower for the top right and bottom row relative to the top left row.

In order to investigate the contribution of mean and instantaneous processes on total reaction, non-dimensional profiles of each term at the same locations are shown in Fig. 3.8. The total reaction term, $\langle C_1 C_2 \rangle$, the product of the means, $\langle C_1 \rangle \langle C_2 \rangle$, and the covariance term, $\langle c_1' c_2' \rangle$ are plotted. For non-cylinder case, Figure 3.8 as discussed above, due to dominant negative values of correlation (due to negative covariance) the product of the means is initially larger than the reaction. As turbulence bring filaments together and the mean plumes begin to overlap, the covariance becomes

positive. In downstream location the covariance is positive across the entire profile. For cylinder cases all covariance terms are positive and they play major role to total reaction term.

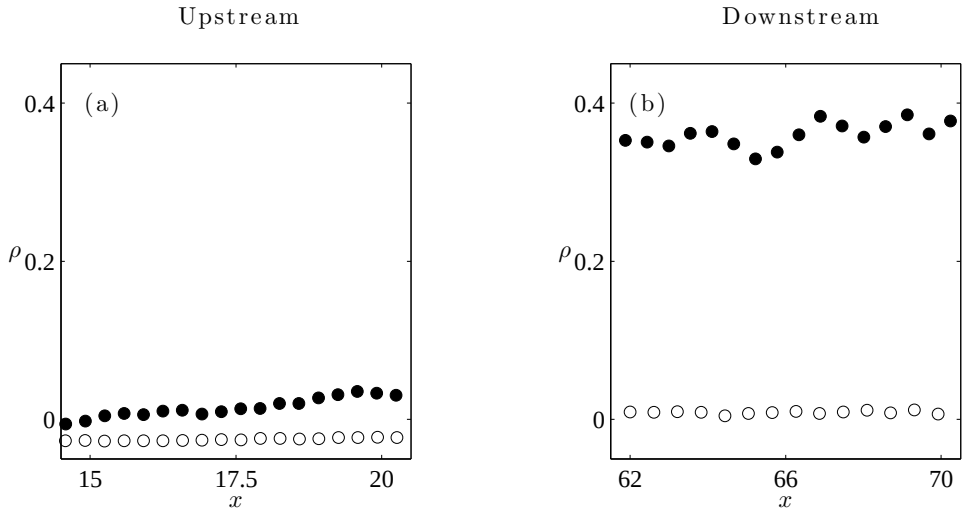

Figure 3.9: Time averaged correlation coefficient profiles along the centerline, $z = 0$ at (a) Upstream, and (b) Downstream locations (∘ No Cylinder - • Cylinder)

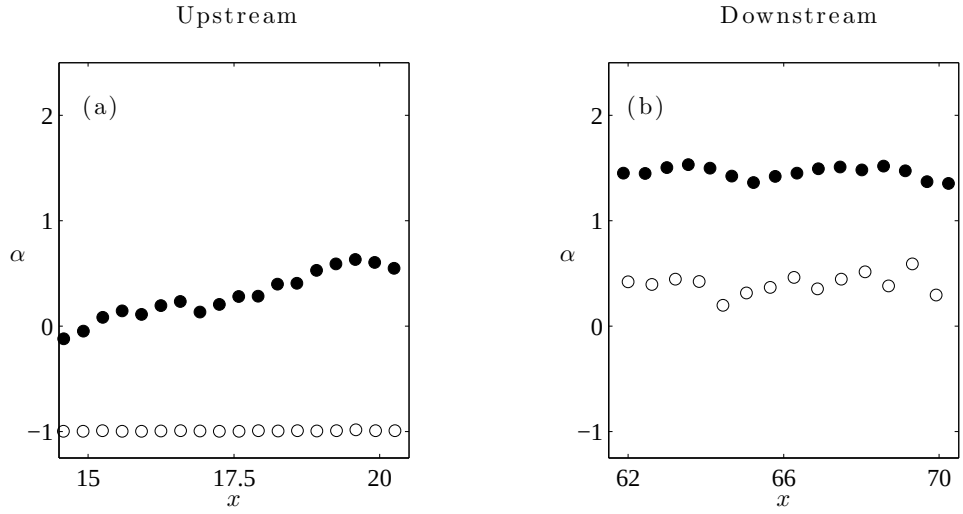

Figure 3.10: Time averaged segregation parameter profiles along the centerline, $z = 0$ at (a) Upstream, and (b) Downstream locations ($\circ$ No Cylinder - $\bullet$ Cylinder)

Figures 3.9-3.10 shows the centerline profiles of the normalized covariance as the Pearson's correlation coefficient and the segregation parameter, α, which is defined as:

$$\alpha = \left\langle c_1' c_2' \right\rangle / \left\langle C_1 \right\rangle \left\langle C_2 \right\rangle \tag{3.5}$$

are shown. In upstream cylinder case, ρ increases with x along the centerline due to existence of turbulence wakes behind the cylinder, but in downstream, turbulence eddies dominate cylinder wake and ρ is almost constant. However, both ρ and α centerline values in cylinder case are bigger than non-cylinder case. The variation of ρ and α values in non cylinder case are decreased in the farthest downstream of flow and they are almost constant.

The roles of instantaneous and mean processes are compared using the beta parameter. Figure 3.11 shows the traverse profiles of the normalized covariance called the beta parameter, β,

$$\beta = \left\langle c_1' c_2' \right\rangle / \left\langle C_1 C_2 \right\rangle \tag{3.6}$$

for two obstructive and grid turbulence flows. Figure 3.11a implies that, at downstream

location beta increases due to the presence of the cylinder, and the contribution from instantaneous processes to the total overlap is increased up to 65% along the centerline regions (i.e., $z/w < 0.1$).

In terms of location, figure 3.11b shows thatβ monotonically increases due to decay of $< C_1 >< C_2 >$ in comparison with upstream case. Generally for both cases, off the centerline ($z/w > 0.1$) the scalar covariance is the dominant term and $\beta > 0.25$. In these regions, the product of the means completely fails to predict the mean scalar overlap.

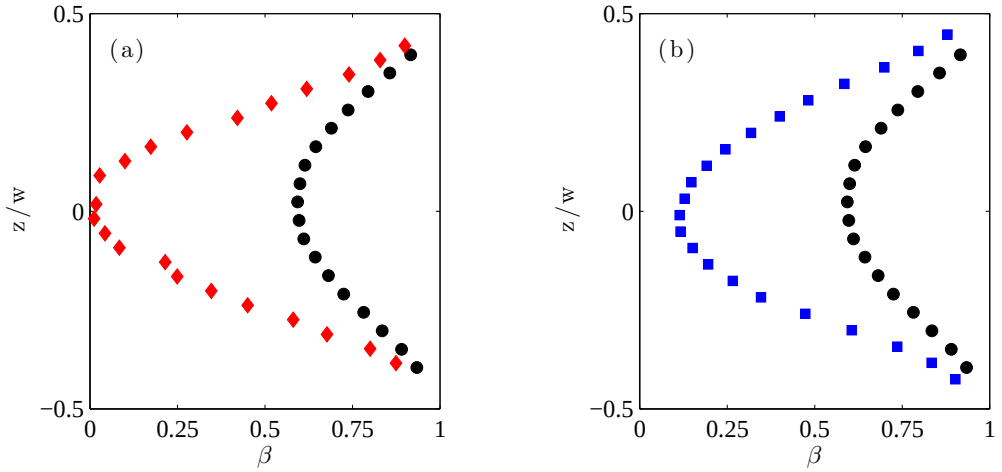

Figure 3.11: Comparison of β for (a) ♦ No Cylinder vs. • Cylinder at downstream location and (b) ■ Upstream vs. • Downstream in Cylinder case

3.3.1 Effect of The Flow Velocity and Nozzles Spacing on Cylinder Wake Mixing

Additional data was taken for the close nozzle space ($s = 1.20$ cm) at low Reynolds number ($Re_\phi = 2000$) at downstream location to help understand the effect of nozzle spacing on cylinder wake mixing. In addition, One more experimental setup was considered in regular nozzle spacing (i.e., $s = 2.41$ cm) in cylinder case at downstream location ($x = 146 - 170$ cm) but for higher flow speed regime. The flow velocity of 10.05 cm/s with temperature held at 21.5 C yielded $Re_\phi = 5000$ for cylinder case. Accurate velocity measurement were taken using the LDV in the flow test section as well.

An instantaneous composite image of an x-z slice through the cylinder wake system appears in Fig. 3.12. According to Fig.3.12, in terms of nozzle spacing, there is not much difference in filaments' shape at that specific location, but in higher Reynolds number you will observe more cylinder mixing entire depth of the flow. Although the concentration of each filaments has decayed and the total reaction is less than reaction in low Reynolds number.

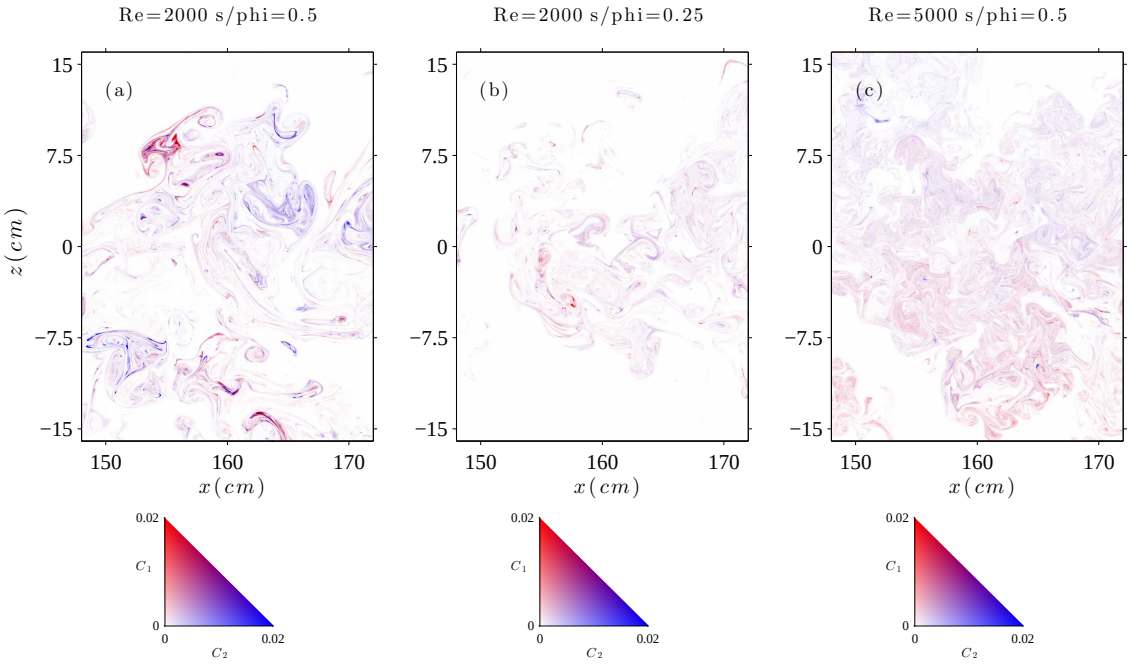

Figure 3.12: Instantaneous distributions of concentrations C_1 and C_2 at three cases are shown. The left stands for $\tilde{s}/\tilde{\phi} = 0.5$ at $Re_\phi = 2000$, the middle depicts $\tilde{s}/\tilde{\phi} = 0.25$ at $Re_\phi = 2000$, and the right shows the $\tilde{s}/\tilde{\phi} = 0.25$ at $Re_\phi = 5000$. The color scheme for C_1 (shades of red), C_2 (shades of blue), and various combinations of the two (shades of purple) is illustrated correspond to each case.

The time-averaged, non-dimensional concentration profiles of the plumes for three cases at downstream location appear in Fig. 3.13. Each point represents a bin of 60 x 60 pixels, averaged spatially and temporally and then normalized to full strength dye concentration. The averaged

plumes are symmetric along the centerline between the nozzles ($z = 0$), but they not Gaussian and sometimes with a slight skew due to the entrainment of the two plumes towards each other.

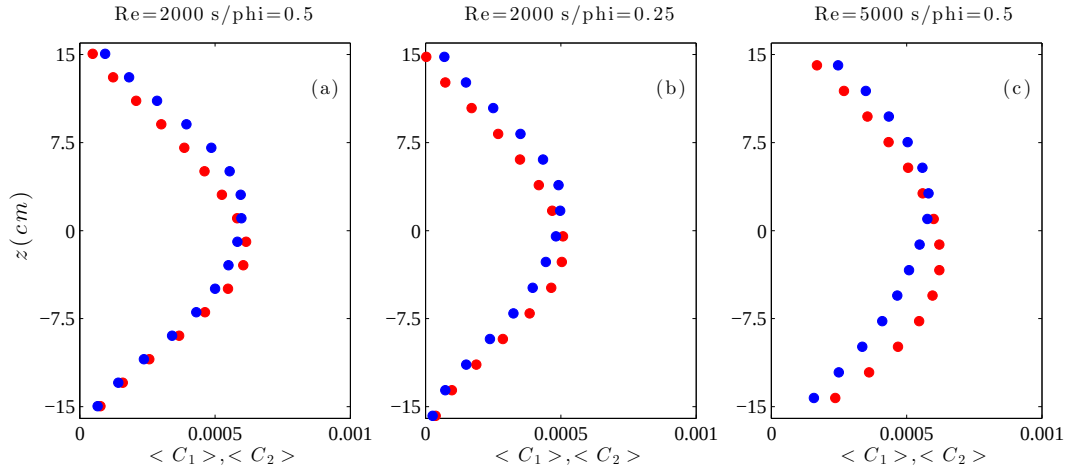

Figure 3.13: Profiles of average concentrations $< C_1 >$ (red) and $< C_2 >$ (blue) corresponding to the three cases shown in Fig. 3.12

The total non-dimensional simulated reaction product, $\langle C_1 C_2 \rangle$ appears in Fig. 3.14. The centerline increases as the mean scalar fields are spread across the domain, However, in same flow regime, in the bigger nozzle spacing case, the mixing are larger than mixing in the corresponding close nozzle spacing

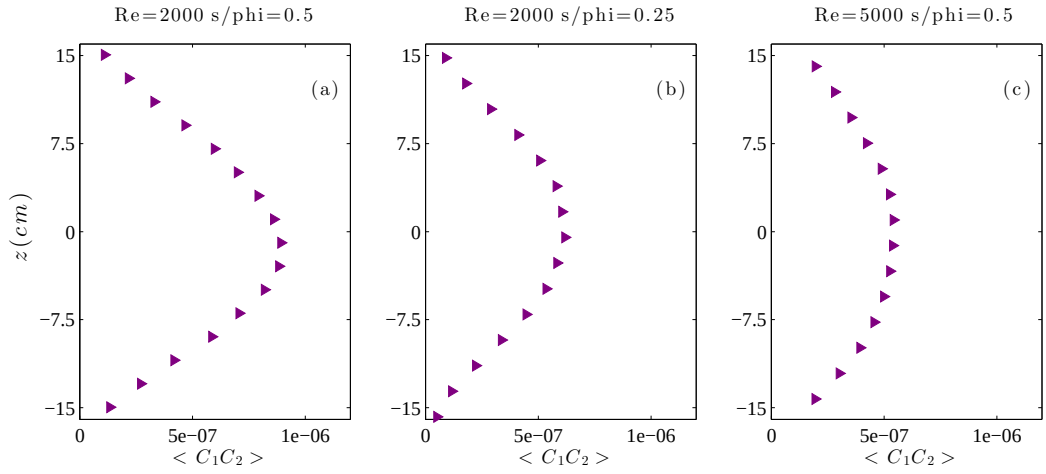

Figure 3.14: Profiles of average scalar overlap $< C_1C_2 >$ corresponding to the three cases shown in Instantaneous images

The roles of instantaneous and mean processes are compared using the beta parameter. Figure 3.15 shows the traverse profiles of the normalized covariance called the beta parameter, $\beta = \langle c_1' c_2' \rangle \,/\, \langle C_1 C_2 \rangle$ for two turbulence flows (i.e., $Re_\phi = 2000$ and $Re_\phi = 5000$) and in two nozzle spacings (i.e., $\tilde{s}/\tilde{\phi} = 0.25$ and $\tilde{s}/\tilde{\phi} = 0.5$). Figure 3.15a implies that, at low Reynolds number at downstream location and with presence of cylinder beta is unchanged by nozzle spacing, meaning that the instantaneous processes contribution to the total overlap is independent of nozzle spacing. Figure 3.15b shows that the $\langle c_1' c_2' \rangle$ continues to decay and β monotonically decreases, approaching 0.35% along the centerline regions (i.e., $z/w < 0.1$ for higher Reynolds number at downstream location and same nozzle spacing. Generally for both cases, off the centerline ($z/w > 0.1$) the scalar covariance is the dominant term and $\beta > 0.50$. In these regions, the product of the means completely fails to predict the mean scalar overlap.

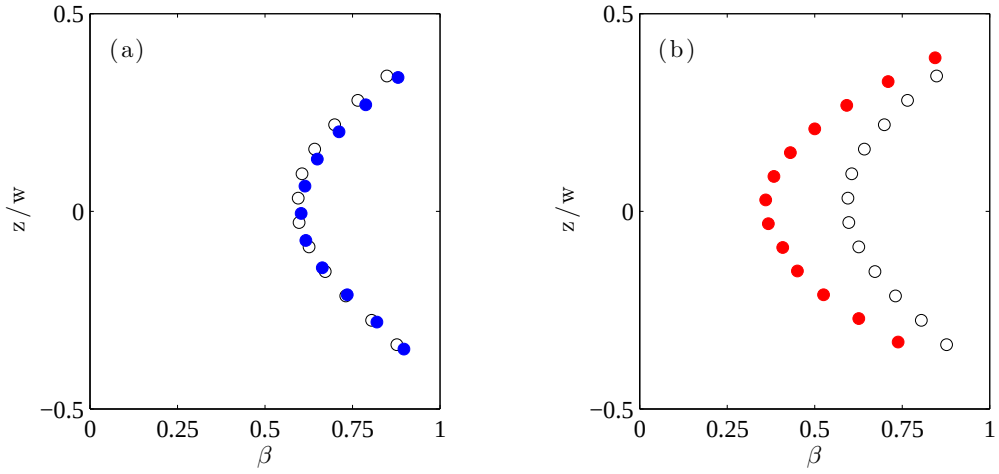

Figure 3.15: Comparison of β for (a) • $\tilde{s}/\tilde{\phi} = 0.25$ vs. ∘ $\tilde{s}/\tilde{\phi} = 0.5$ at $Re_\phi = 2000$ and (b) • $Re_\phi = 5000$ vs. ∘ $Re_\phi = 2000$ in $\tilde{s}/\tilde{\phi} = 0.5$.

3.3.2 Velocity and Turbulence Intensities Measurement

The velocity signal is decomposed according to $u =< U > +u'$, where $< U >$ is the mean velocity and u' is the fluctuating component. The mean velocity is also described nondimensionally as $< U >=< U > /U_o$, where U_o is the averaged velocity over entire depth of flow in non-cylinder case [33].

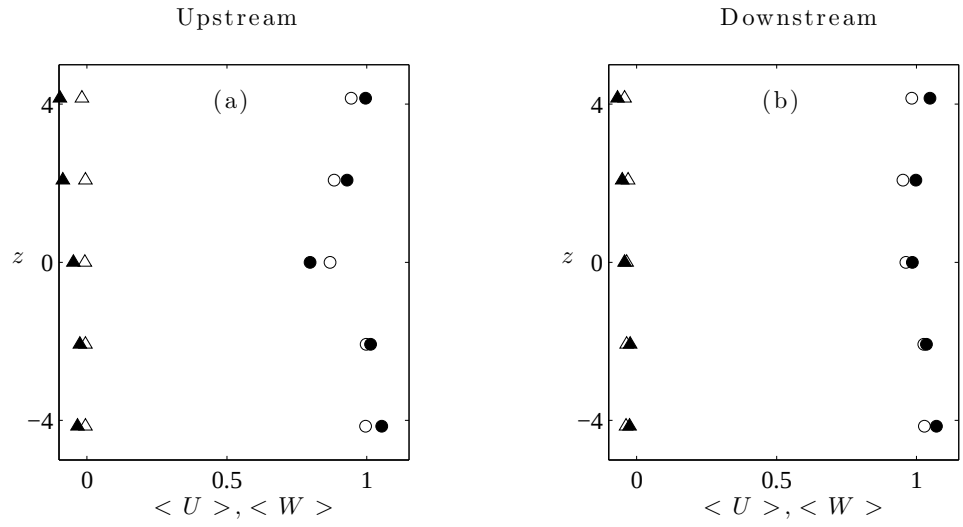

Figure 3.16: Nondimensional mean velocity profiles in cylinder wake region for $U_o = 4.05$ cm/s, streamwise and vertical components for (a) Upstream and (b) Downstream location (∘ No Cylinder $< U >$, △ No Cylinder $< W >$, • Cylinder $< U >$, ▲ Cylinder $< W >$)

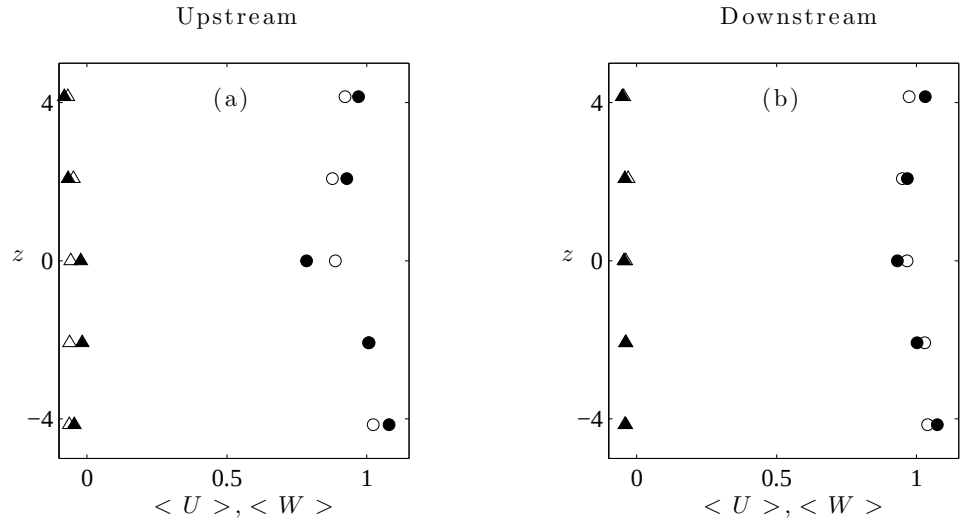

Figure 3.17: Nondimensional mean velocity profiles in cylinder wake region for $U_o = 10.05$ cm/s, streamwise and vertical components for (a) Upstream and (b) Downstream location (∘ No Cylinder $< U >$, △ No Cylinder $< W >$, • Cylinder $< U >$, ▲ Cylinder $< W >$)

Figures 3.16 -3.17 shows non-dimensional velocity data for $U_o = 4.05$ cm/s and $U_o = 10.05$

cm/s at two upstream and downstream locations respectively. The statistics are plotted versus z non-dimensional depth of flow. The figures compare cylinder data (closed symbols) with non-cylinder data (open symbols). They all are symmetric to $z = 0$, but there is a horizontal velocity deficit along the centerline at upstream location due to existence of cylinder. This effect diminishes at downstream location where the role of cylinder's location in flow field is negligible.

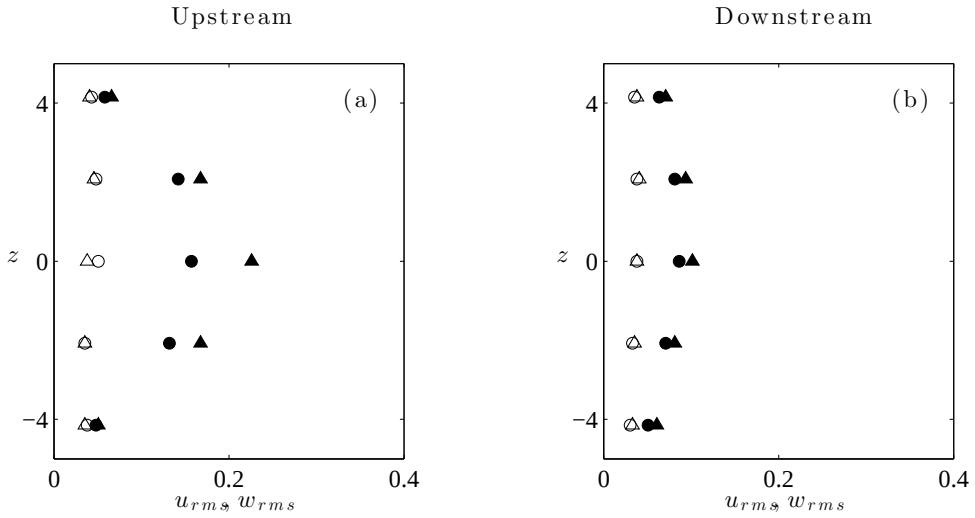

Figure 3.18: Turbulent intensity profiles are shown at (a) $\tilde{x} = 42$ cm/s (Upstream), and (b) $\tilde{x} = 160$ cm/s (Downstream) comparing cylinder data (closed symbols) with No cylinder data (open symbols).

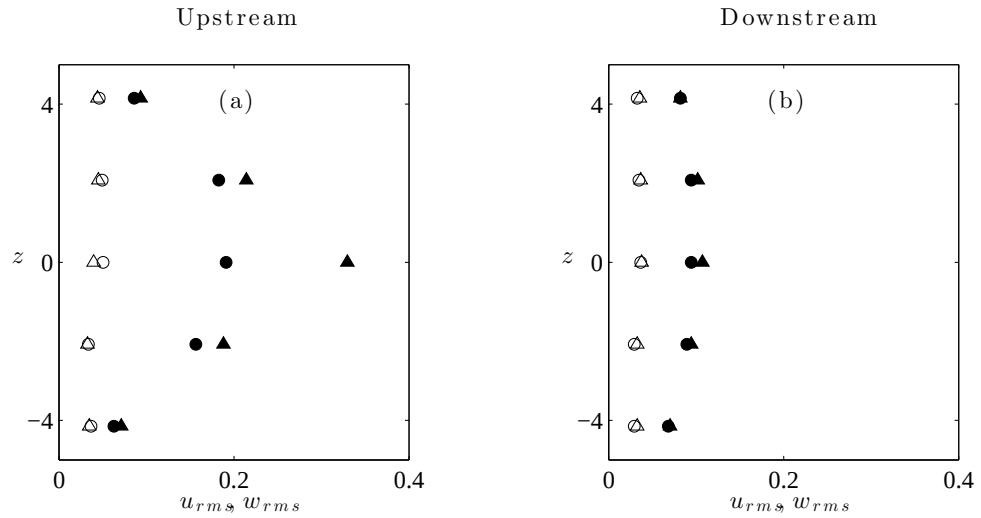

Figure 3.19: Nondimensional turbulence intensity profiles for $U_o = 10.05$ cm/s, streamwise and vertical components for (a) Upstream and (b) Downstream location

Similarity, the non-dimensional turbulence intensities data, (u_{rms} and w_{rms}) are shown in Figs. 3.18 -3.19 at two upstream and downstream locations. According to definition, $u_{rms} = \sqrt{< u'^2 >}$, and u' is the fluctuating component of velocity field. The figures compare cylinder data (closed symbols) with non-cylinder data (open symbols). In No cylinder case, the profiles of u_{rms} and w_{rms} are uniform entire the depth of flow, but in the cylinder case It is clear that all two profiles exhibit a hump around the cylinder axis ($z = 0$) and an increase of u_{rms} and w_{rms} is observed. This increase is probably produced by instability motions occurring in the vicinity of cylinder zone.

When the cylinder obstacle is included, a well-marked peak is observed at the upstream section ($\tilde{x} = 42cm$). This peak diminishes at downstream location ($\tilde{x} = 160cm$). This is a particular interest that how turbulence level and the fluctuating scalar fields contribute to the total scalar mixing. The turbulence length scale of flow will be proposed to estimate in future to investigate its relationship with mixing and coalescence of filaments and the total reaction rate.

Chapter 4

Analytical Model of Scalar Filament Structures on Mixing, Reactions and Segregation Parameter

4.1 Introduction

Mechanical stirring stretches introduced scalars into thin shells (in 3D) and filaments (in 2D), increasing the interfacial area between the scalar and surrounding fluid, sharpening concentration gradients, and enhancing diffusive mixing and reactions. For chaotic systems, filaments undergo a stretching and folding process that locally forms closely spaced scalar lamellae. If two reactive scalars are present, mechanical stirring and diffusion can produce partial overlap of adjacent filaments, with associated reactions in the region of coalescence. For structured stirring, the spatial distribution of instantaneous reaction rate can be highly localized, especially for weakly diffusive scalars.

When two scalars mix in ambient fluid we can say that the mean local mixing parameter, $< C_1\, C_2 >$:

$$< C_1 C_2 > = < C_1 >< C_2 > \; + \; < c_1' c_2' > \tag{4.1}$$

where the two terms on the RHS correspond to contributions from the mean and fluctuating concentration fields, respectively.

The manner in which two separate fluctuating scalars are correlated, and the processes by which the correlation develops are important in turbulent mixing and reactions area. In fact, the correlation indicates the effects of turbulence and molecular mixing on the mean chemical

reaction rate. for example, In an isothermal flow, for a second-order chemical reaction between two chemical scalars, a general turbulent diffusion (mass conservation) equation can be written for the mean concentration $< C_1 >$ and $< C_2 >$:

Figure 4.1: Experimental modeling of two scalars mixing in fluid

$$\frac{\partial < C_1 >}{\partial t} + U_i \cdot \nabla < C_1 >= D_1 \nabla^2 < C_1 > -K[< C_1 >< C_2 > + < c_1' c_2' >] \tag{4.2}$$

$$\frac{\partial < C_2 >}{\partial t} + U_i \cdot \nabla < C_2 >= D_2 \nabla^2 < C_2 > -K[< C_1 >< C_2 > + < c_1' c_2' >] \tag{4.3}$$

where C and c' are the instantaneous and fluctuating concentrations, D_i is the molecular diffusivity and K is the chemical-reaction-rate constant and U_i is the mean velocity in the x_i direction, and the $<>$ indicate mean (averaged) values. The second term on the right, as seen in Eq. 4.1, is the mean chemical reaction rate term, and it can be split into the mean concentration product $< C_1 >< C_2 >$ and the concentration fluctuation product $< c_1' c_2' >$. Clearly, the latter correlation between the species concentration fluctuations, $< c_1' c_2' >$, is of great importance if the covariance

term is not equal to zero. [84, 8, 69].

The sign of the mean covariance term, $< c_1' c_2' >$, can be changed by the way C_1 and C_2 are correlated. In the last chapter we learned that the covariance term can be expressed as the Pearson's correlation coefficient, $\rho = \frac{<c_1' c_2'>}{\sqrt{<c_1'^2>}\sqrt{<c_2'^2>}}$, or as the segregation parameter, $\alpha = \frac{<c_1' c_2'>}{<C_1><C_2>}$, when it normalized by the mean concentrations. This was first introduced by Danckwerts [26] when considering the depletion rate of the reactants. Komori et al. [69] studied ρ and α parameters using a Lagrangian stochastic model for non-premixed reacting flows. He found that α increases from near -1 to zero with the time (or distance) from the moment (or location) of release of two species in turbulent flows. If $\alpha = -1$, there is no molecular mixing since $C_1 C_2 = 0$.

There have been other meausrements of α in counterflowing jets [96], in grid turbulence [7] and in a two-dimensional plume in the atmospheric surface layer [69]. In these studies the asymptotic values of α varied from slightly negative values to -0.7. Wide range of values are measured in different studies (e.g., [7, 9, 70, 82, 142]. There is controversy concerning the sign of α in some flows [9, 69]. Measurements of α for atmospheric mixing, in which we need accurate knowledge of reactions involving HNO_3, O_3 and other species, can be studied as well (e.g., [108]). Studying the sign and magnitude of segregation parameters under different regimes of flows is still required.

In addition, Juneja and Pope [61] investigated the DNS studies of two-scalar mixing without reaction, including the evolution of their joint pdf. The turbulent scale (Re number), Schmidt number, and Damkohler number affect the ρ and α and they are strongly dependent on ratio of initial concentrations of two reactants [69]. The segregation parameter varies widely within a particular flow and mean shears can affect α as well [142].

The correlation coefficient and segregation parameter provide information about a bulk measure of mixing, but contain no scale information [142]. Mixing is a multi-scale process, while turbulence deals with the large and intermediate scales, and molecular diffusion smears and completes the mixing at the smallest scales, the correlation can become positive only when the scalars are mixed at molecular level. Warhaft [148] showed that when two reactive scalars are released separately into a fluid, $\rho \approx -1$ close to the sources, where the turbulence is moving plumes up

and down simultaneously, to $\rho \approx +1$ far downstream, where the plumes have mixed. The result of boundary-layer measurements show the same trend [115].

To investigate the role of mean and fluctuating reactant concentrations on average reactions in mechanically stirred systems, we present an idealized one-dimensional model of two neighboring reactant filaments. The model is assumed to represent a pair of "typical" reactant filaments for a given system, based on filament cross-sectional shape, width, and abundance, as well as the typical proximity between them. The objective is to understand how the instantaneous structure and spacing of filaments determines the relative contributions of the mean product and covariance terms to the average reaction.

4.2 Model

In many situations, the resulting spatial or temporal average of the reaction rate is of interest, and there is value in expressing this net reaction rate in terms of average scalar parameters. For a second-order reaction between two scalars, the average reaction rate can be decomposed as the sum of two contributions: the product of the average concentrations plus the covariance of the two fluctuating concentrations. The relative importance of the these two contributions depends on the structural characteristics and relationship between neighboring filaments.

According to Eq. 4.1, we consider a class of reaction problems where the two reactants are initially localized and distant from one another, separated by ambient fluid that contains neither reactant. We propose a simple 1-D idealized model of a representative slice across two representative filaments (Fig. 4.2). In this model we define σ as representation of filament width, s as representation of filament separation, h as representation of spatially averaged concentration. In addition, we assume filaments profiles are symmetric and gaussian. We will use the model to investigate the effect of σ, s, and h on $< c_1' c_2' >$, and to gain intuition on the processes that govern the magnitude and sign of reaction terms.

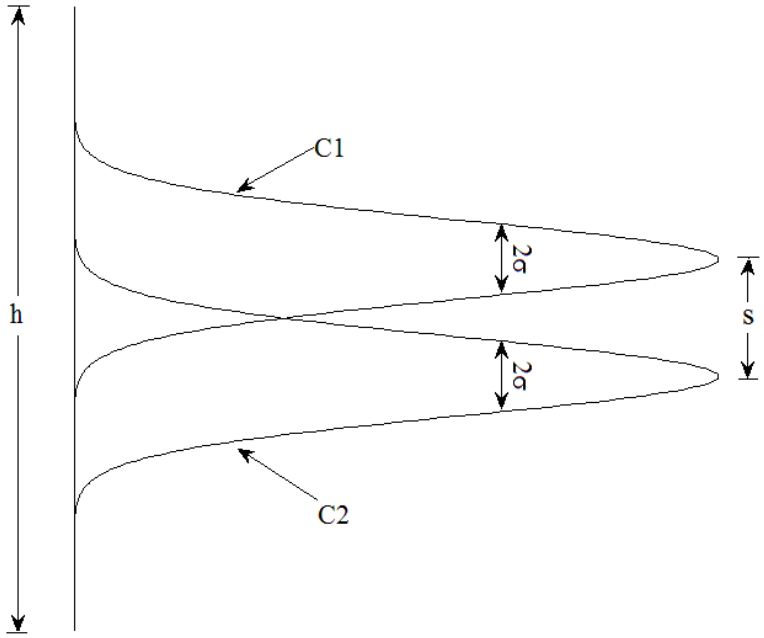

Figure 4.2: Parameter definitions

The filament concentration profiles shown in Fig. 4.2 are described by,

$$C_1(y) \;=\; C_0 \exp(-\frac{(y+\frac{s}{2})^2}{2\sigma^2}) \tag{4.4}$$

and,

$$C_2(y) \;=\; C_0 \exp(-\frac{(y-\frac{s}{2})^2}{2\sigma^2}) \tag{4.5}$$

Eq. 4.4 and Eq. 4.5 can be written nondimensionally as:

$$C_1^* = \exp(-\frac{(2y^*h^*+s^*)^2}{8}) \tag{4.6}$$

and

$$C_2^* = \exp(-\frac{(2y^*h^*-s^*)^2}{8}) \tag{4.7}$$

where $C_1^* = \frac{C_1}{C_0}$, $C_2^* = \frac{C_2}{C_0}$, $y^* = \frac{y}{h}$, $s^* = \frac{s}{\sigma}$, and $h^* = \frac{h}{\sigma}$.

According to Eq. 4.1, the spatially averaged covariance would be,

$$< {c_1'}^* {c_2'}^* >=< C_1^* C_2^* > - < C_1^* >< C_2^* > \tag{4.8}$$

The concentrations can be spatially averaged over the model domains:

$$< C_1^* >= \frac{\sqrt{2\pi}}{2h^*}[\mathrm{erf}(\frac{h^* - s^*}{2\sqrt{2}}) + \mathrm{erf}(\frac{h^* + s^*}{2\sqrt{2}})] \tag{4.9}$$

Which is same equation for $< C_2^* >$.

The product of the concentration profiles can be spatially averaged in a similar fashion, leading to:

$$< C_1^* C_2^* >= \frac{\sqrt{\pi}}{h^*} \exp(-\frac{{s^*}^2}{4})\mathrm{erf}(\frac{h^*}{2}) \tag{4.10}$$

Thus, normalizing Eq. 4.8 by $< C_1^* >< C_2^* >$, it gives a coefficient called "Segregation Parameter:" [26, 69]

$$\alpha = \frac{< {c_1'}^* {c_2'}^* >}{< C_1^* >< C_2^* >} = \frac{2h^*}{\sqrt{\pi}} \exp(-\frac{{s^*}^2}{4})(\frac{\mathrm{erf}(\frac{h^*}{2})}{[\mathrm{erf}(\frac{h^*-s^*}{2\sqrt{2}}) + \mathrm{erf}(\frac{h^*+s^*}{2\sqrt{2}})]^2}) - 1 \tag{4.11}$$

Contours of α in the $h^* - s^*$ plane are shown in Fig. 4.3. Here, the segregation parameter increases as h^* gets larger and s^* gets smaller.

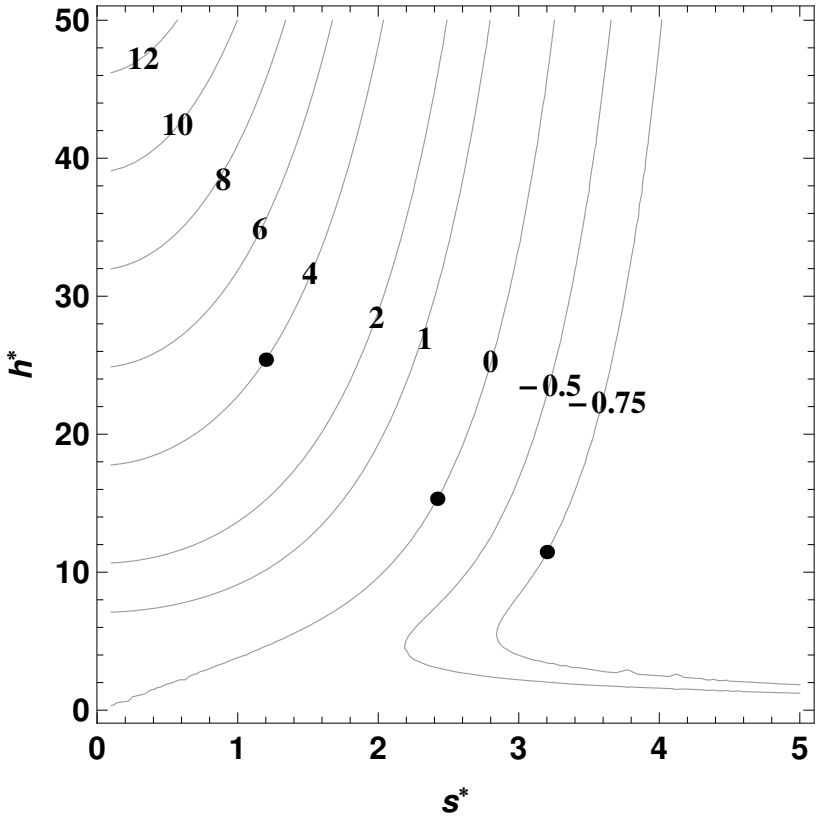

Figure 4.3: Local mixing contours, normalized to product of mean concentrations: $\frac{<c_1'^* c_2'^*>}{<C_1^*><C_2^*>}$, The three solid dots represents a positive segregation parameter (+4), (b) zero, and (c) a negative one (- 0.75).

The segregation parameter varies with h^* as shown in Fig. 4.4a. The segregation parameter changes vs. h^* for three different values of s^*. The figure shows that by increase of space between two filaments (e.g., $s^* = 3$), the variation of segregation parameter is significant and it changes between low negative values to high positive ones.

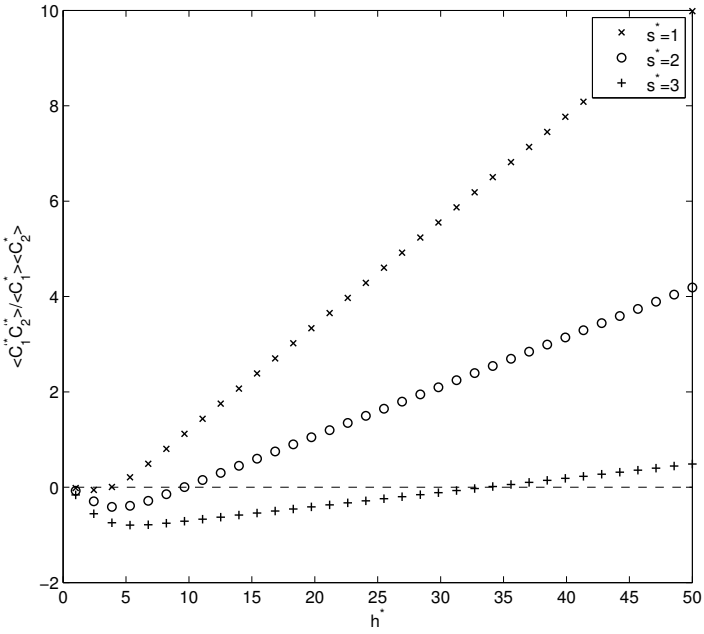

(a) $\alpha vs. h^*$

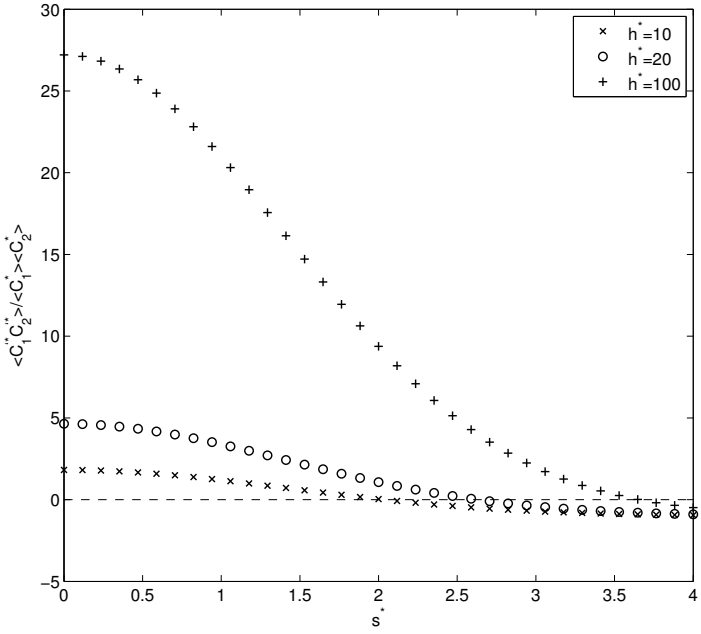

(b) $\alpha vs. s^*$

Figure 4.4: Segregation parameter changes vs. h^* and s^*

The segregation parameter varies also with s^*. Fig. 4.4b shows the segregation parameter changes vs. s^* for three different values of h^*. The plot shows that in smaller domain size ($h^* = 10$), the variation of segregation parameter is significant and it changes between negative values to positive ones.

4.3 Results and Discussion

Here we focus on three different segregation parameters spanning a range of behaviors: (a) a positive segregation parameter (+4), (b) a value of zero, and (c) a negative value (- 0.75). The location of these parameters are shown as solid dots in Fig. 4.3. In Fig. 4.5, plots of nondimensional concentration profiles and concentration covariance profiles for two filaments are shown for specific value of h^* and s^* for the three chosen values of the segregation parameter.

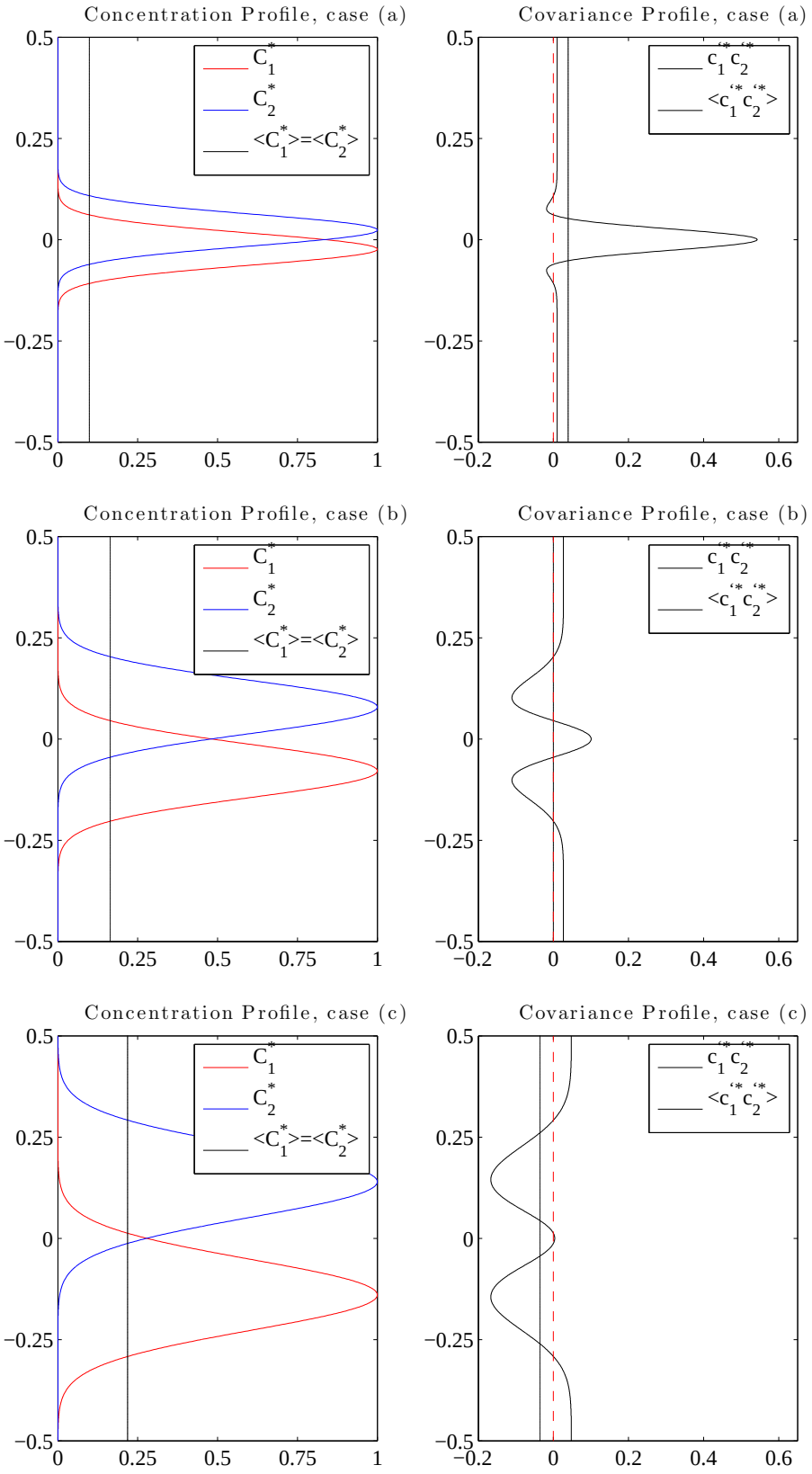

Figure 4.5: Nondimensional concentration and concentration covariance profiles of two filaments in different cases, a: positive segregation, b: zero segregation, c: negative segregation

Now, we can discuss physically the trend of covariance profile for specific case (e.g. Fig. 4.5b). By definition, $< C_1 >< C_2 >$ is everywhere non-negative, with positive values corresponding to regions where the mean concentration fields overlap. The covariance $c_1'c_2'$ is positive over the central region of the domain ($y^* = 0$) and ($|y^*| > 0.25$), and regions of negative fluctuation covariance near $y^* = \pm 0.125$. As it said, the understanding of these averaged covariances requires an investigation of the instantaneous scalar fields. Contributions to the scalar mixing product C_1C_2 come from the mean scalar fields as well as the fluctuating scalar fields c_1' and c_2'. In addition, the region near $y^* = \pm 0.125$ is dominated by filaments where $c_1'c_2'$ is negative, corresponding to events where turbulent intrusions of fluid from one filament displace fluid from the second filament. If the filament containing C_1 does the displacing, then locally $c_1' > 0$ and $c_2' < 0$, and vice-versa. It is obvious that in central region, $c_1'c_2'$ is strongly positive. A representative positive contribution to this average is seen in the fluctuating scalar field $< c_1'c_2' >$ near $y^* = 0$ resulting in $c_1' > 0$ and $c_2' > 0$. Outside the central region, in the vicinity of $y^* = \pm 0.25$, $c_1'c_2'$ is positive again. These are not mixing regions, but, instead, regions where C_1 and C_2 are both zero (Fig. 4.5).

4.3.1 Constraints and Boundaries of The Model

As we defined the model earlier, it is assumed to represent a pair of "typical" reactant filaments for a given system, and their cross-sectional shape, width, and their typical proximity look like they are initially localized and distant from one another. We need to consider the boundary condition in order to validate the equation's solution. The tail of filaments' concentration profile should look like the Gaussian shape profile at boundaries and goes to the zero. Otherwise, we need to investigate the "Mirror Image Effect" at boundaries. It means there is probability that the filament separation (i.e., s^*) would increase to some extent that causes the filaments' concentration profile crosses the width of the model (i.e., h^*).

In order to investigate mirror image effect we set a constraint as $C^* <= 0.05$ at boundaries (i.e., at y*= +/- 0.5). It means we assume the concentration values at boundaries are less than 5% of the initial concentration (i.e., C_0). However, we plotted the non-dimensionally contour for

segregation parameters for with and without mirror image effect on boundaries. According to Fig. 4.6, the result shows that even in the case $C^* > 0.05$, it doesn't affect segregation parameter value and we can neglect it in the closed-form solution (Fig. 4.7).

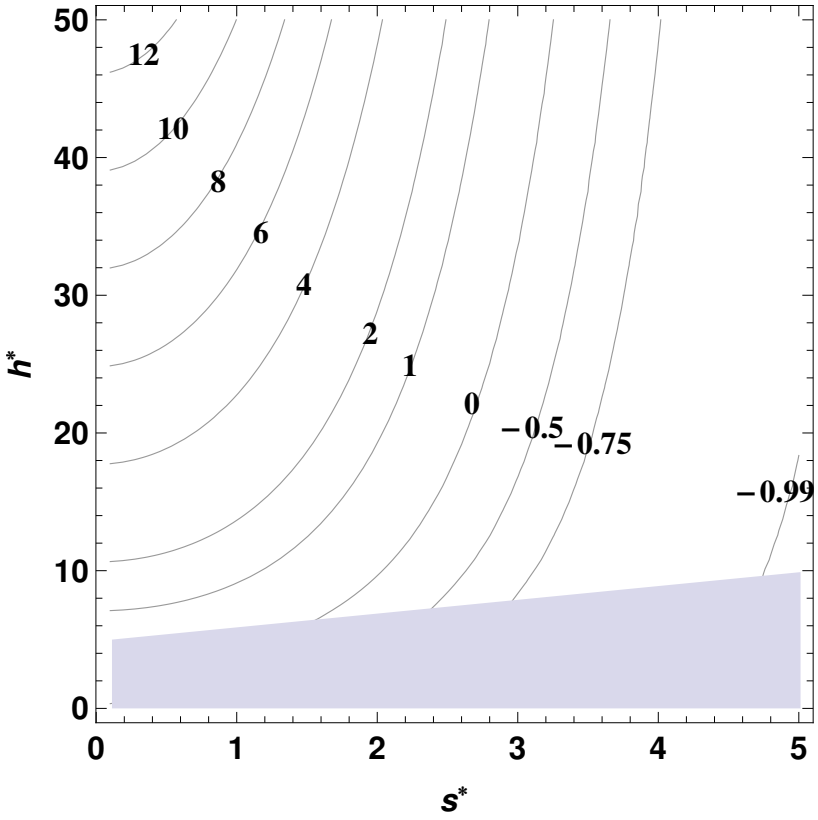

Figure 4.6: Contour of the segregation parameters with boundary condition $C^*_{1,2} <= 0.05$. In this case, the s^* is always less than h^*.

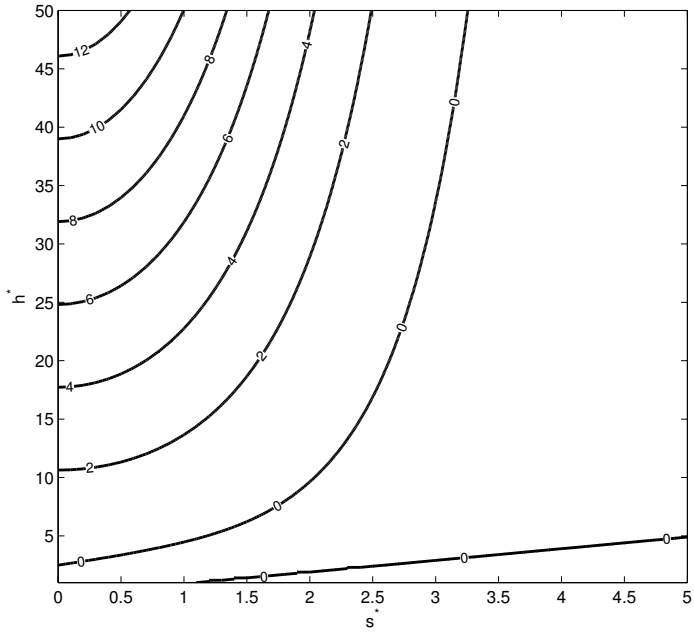

(a) $WithoutMirrorImageEffect$

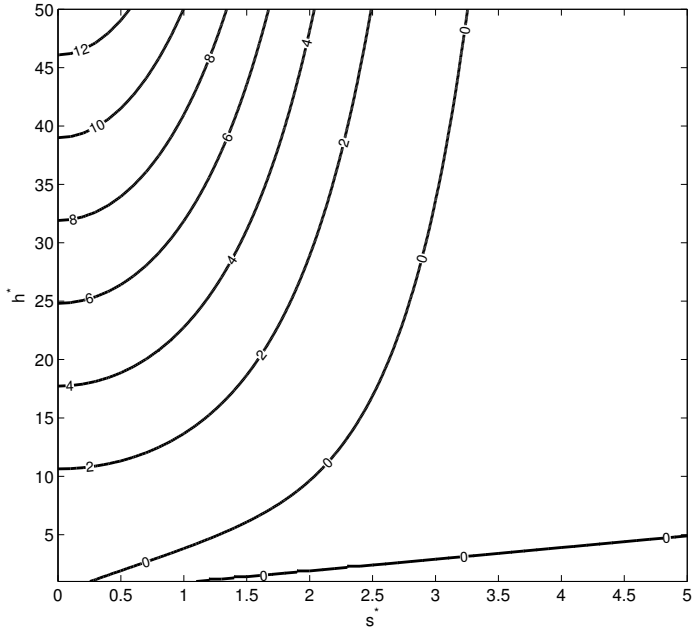

(b) $WithMirrorImageEffect$

Figure 4.7: Contour of the segregation parameter with and without mirror image effect at boundaries

In order to find a boundary for mixing, we also equalize Eq. 4.11 to zero to see which criteria affects the mixing. So It becomes:

$$(\frac{\text{erf}(\frac{h^*}{2})}{[\text{erf}(\frac{h^*-s^*}{2\sqrt{2}}) + \text{erf}(\frac{h^*+s^*}{2\sqrt{2}})]^2})h^* = \frac{\sqrt{\pi}}{2}\exp(-\frac{{s^*}^2}{4}) \tag{4.12}$$

By considering assumptions like $h^* >> s^*$, $s^* > 1$ and $erf(x)|_{x>2} \simeq 1$, above equation is summarized to:

$$h^* \approx 2\sqrt{\pi}\exp(-\frac{{s^*}^2}{4}) \tag{4.13}$$

It means that local mixing parameter would be zero when you move on this line. In Fig. 4.8 the mixing parameter is plotted for zero value based on different h^* and s^*. For comparison, the Eq. 4.13 line is plotted as well. It shows that assumptions are well considered with the scenario.

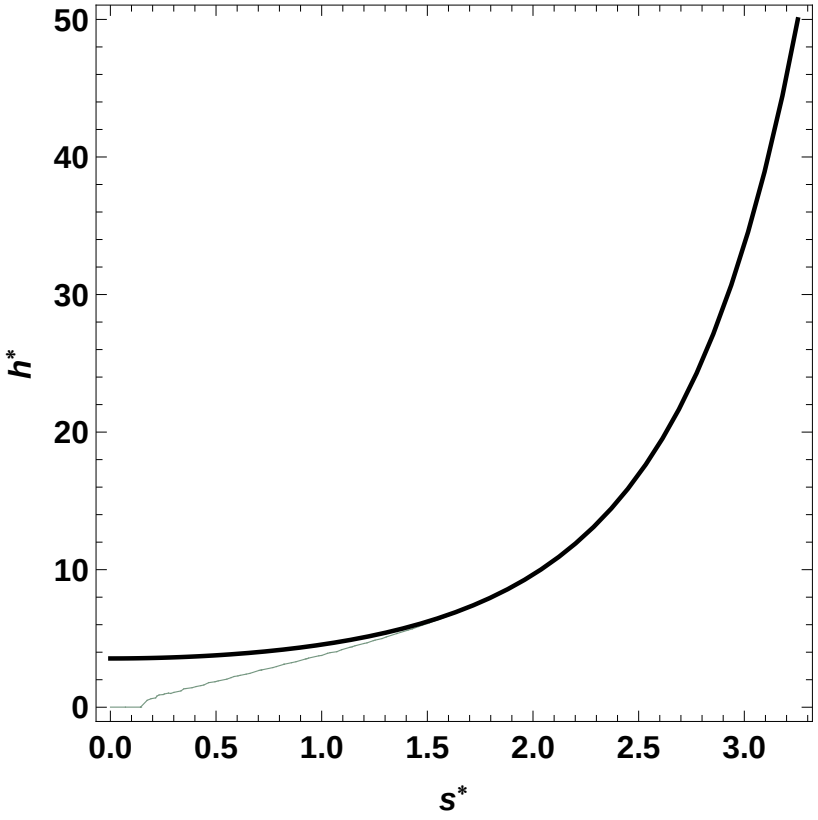

Figure 4.8: Thin line: $\frac{<{c_1'}^*{c_2'}^*>}{<C_1^*><C_2^*>} = 0$, Thick line: $h^* \approx 2\sqrt{\pi}\exp(-\frac{{s^*}^2}{4})$

4.3.2 Non-Gaussian Case Model

Now, consider a model of a representative slice across two representative filaments where their concentration cross profile for each filament physically looks symmetric, but Non-Gaussian. In fact, we assume there is a length at filaments' peak concentration which the concentration profile looks Non-Gaussian. The objective is to understand how the instantaneous structure and filaments separation in this case governs the magnitude and sign of the segregation parameter. The solution corresponding to a finite domain for filament 1 is:

$$C_1(y) = \frac{C_0}{2}[\mathrm{erf}(\frac{y + f/2 - s/2}{\sigma}) - \mathrm{erf}(\frac{y - f/2 - s/2}{\sigma})] \tag{4.14}$$

and

$$C_2(y) = \frac{C_0}{2}[\mathrm{erf}(\frac{y + f/2 + s/2}{\sigma}) - \mathrm{erf}(\frac{y - f/2 + s/2}{\sigma})] \tag{4.15}$$

where s is center to center distance between two peak filaments' concentration profiles and f is the length of the filament at peak at Non-Gaussian profile shape and σ is as representation of filament width like Gaussian case.

Eq. 4.14 and Eq. 4.15 can be written nondimensionally as:

$$C_1^* = \frac{1}{2}[\mathrm{erf}(\frac{2y^*h^* + f^* - s^*}{2}) - \mathrm{erf}(\frac{2y^*h^* - f^* - s^*}{2})] \tag{4.16}$$

and

$$C_1^* = \frac{1}{2}[\mathrm{erf}(\frac{2y^*h^* + f^* + s^*}{2}) - \mathrm{erf}(\frac{2y^*h^* - f^* + s^*}{2})] \tag{4.17}$$

Where $C^* = \frac{C_1(y)}{C_0}$, $y^* = \frac{y}{h}$, $f^* = \frac{f}{\sigma}$, $s^* = \frac{s}{\sigma}$ and $h^* = \frac{h}{\sigma}$.

Here is the contour of segregation parameter for dimensional Non-Gaussian case for specific case, $\sigma = 0.1$ and $C_0 = 1$ and $f = 1$, (Fig. 4.9b). You may see that in specific s=0.2, the segregation parameter is equal to 38.

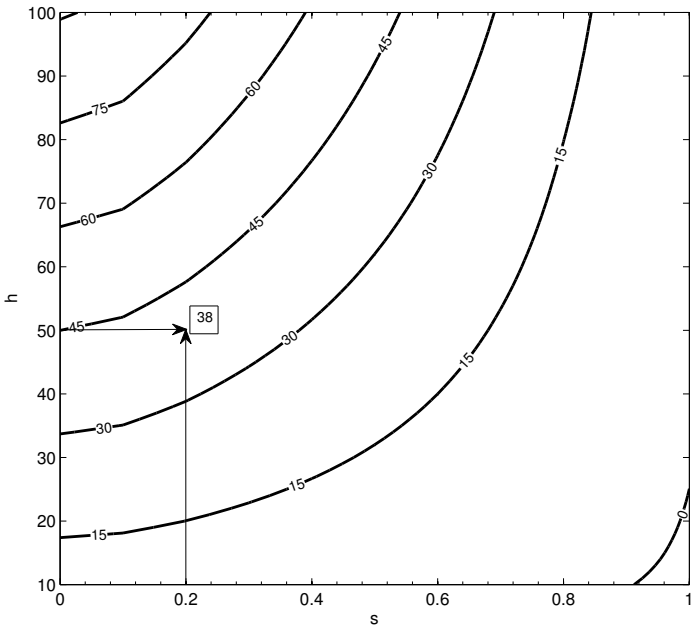

(a) *Gaussian*

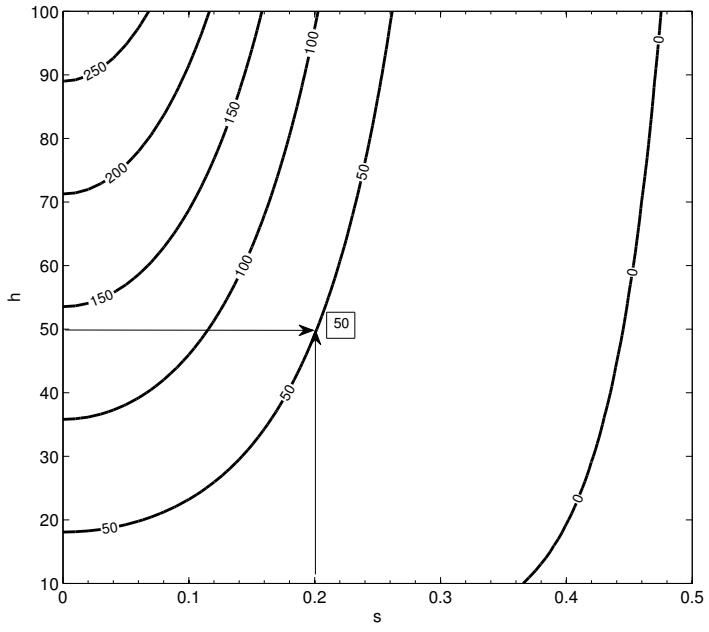

(b) $Non - Gaussian$

Figure 4.9: Dimensional segregation parameter contour in non-Gaussian case

In order to investigate the effect of the length of filament at peak concentration, f, on the segregation parameter, we plot the contour of segregation parameter for dimensional Gaussian case for the specific case (i.e., $\sigma = 0.1$ and $C_0 = 1$) (Fig. 4.9a). You may note that the segregation parameter increases now and its value is around 50. Therefore it can be concluded that dimensionally, due to variation of filaments profile shape from Gaussian to Non-Gaussian, the segregation parameter increases dramatically.

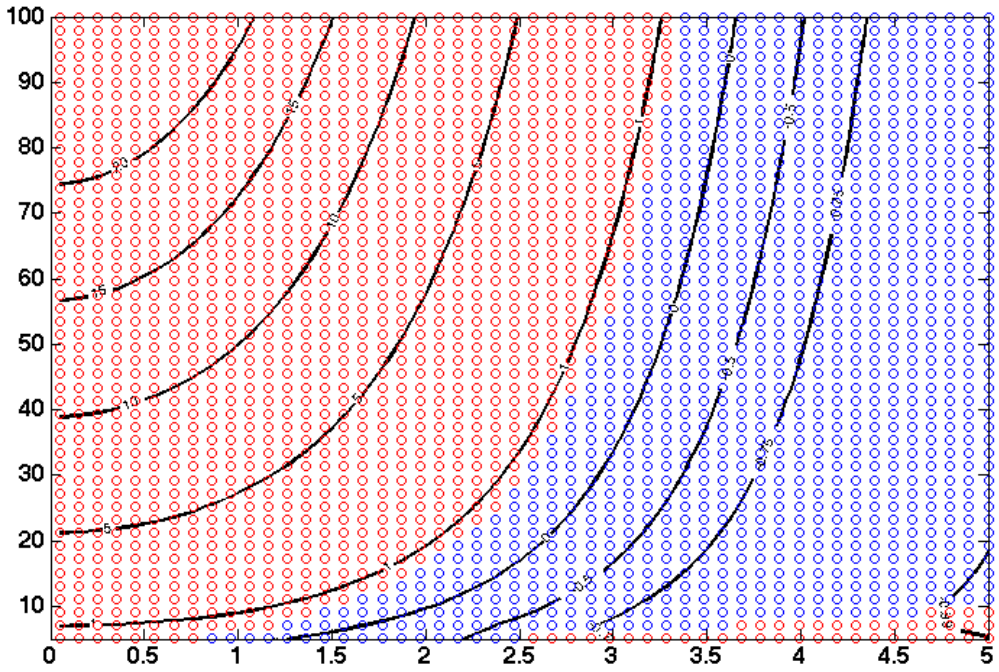

Figure 4.10: Contribution of positive covariance to segregation parameter in middle and corner of domain

Figure 4.10 shows the contribution of positive covariance to segregation parameter in middle and corner of domain. Red dots show region which middle positive covariance ($c_1' > 0, c_2' > 0$) is

dominant ($> 50\%$ contribution to α) and Blue dots show region which corner positive covariance ($c_1' < 0, c_2' < 0$) is dominant ($> 50\%$ contribution to α). In addition, Red dots in right bottom corner are not acceptable, because we assume everywhere $h* > s*$. Moreover, in specific α (e.g., $\alpha = 5$) if you move on contour line to top, the effect of corner positive covariance contribution to total α will be gradually increased. Therefore, we can propose another definition for positive segregation parameter as the ratio of middle positive covariance contribution ($c_1' > 0, c_2' > 0$) to corner positive covariance contribution($c_1' < 0, c_2' < 0$). For example, in (Fig 4.11) the contribution of each section to $\alpha = 4$ is shown. The area under each section is calculated and compared with segregation value. Hence, The middle positive covariance (pure mixing) contribution to α is 81.67% and corner positive covariance (no mixing) contribution to α is 18.33% which it gives you $\alpha \sim 4$.

Therefore we can define α as ratio of pure mixing in middle of domain to no mixing region or where the concentration of each scalars are less than averaged concentration value.

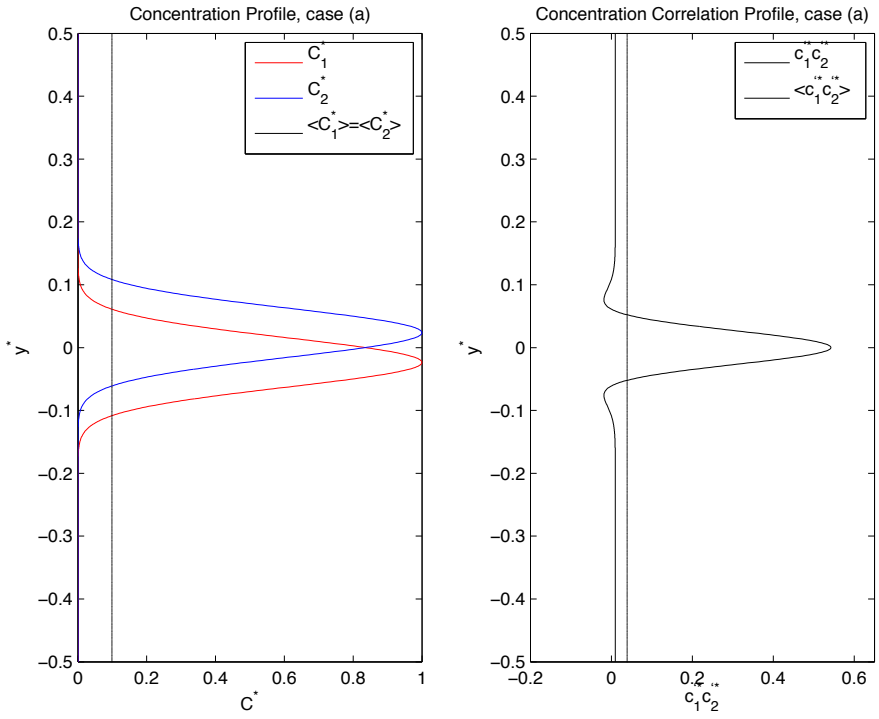

Figure 4.11: Contribution of positive covariance to segregation parameter for middle (Red) and corner (Blue) for $\alpha = 4$

Chapter 5

The Effect Of Viscosity and Non-Newtonian Rheology On Reaction Enhancement Between Two Initially Distant Scalars

5.1 Introduction

Turbulent stirring and mixing produces long-term dilution of gamete concentrations [25, 28], but the dilution may be mitigated by releasing gametes in a viscous matrix [137, 86, 151], or through gamete sequestration in surge channels [28] and tide pools [101]. The viscous non-Newtonian matrix in which gametes are often secreted may help to resist scalar dilution during the intermediate timescales where structured stirring is in the process of bringing gamete filaments into closer contact.

Broadcast spawners typically release gametes that are packaged in a viscous matrix. The rheology of the matrix is typically different from that of the ambient fluid, which alters the way the gametes are dispersed and diluted by the flow. The matrix is often highly viscous, which may act to minimize dilution [137, 86]. The viscous quality also lends a certain stickiness to the gametes, enabling them to adhere to the substratum or to adults [105, 89, 137, 151], where they may be preferentially fertilized. The matrix rheology is typically non-Newtonian and exhibits shear-thinning properties that facilitate extrusion through the gonoduct [137]. Shear-thinning fluids disperse and mix differently than Newtonian fluids (e.g., Niederkorn and Ottino [97]).Yet, the overall role of viscosity and rheology in gamete distribution and fertilization success is unknown.

The primary objective of my research is to understand the mechanistic processes responsible for gamete coalescence, in addition to predicting fertilization rates. The goal is to come up with broadly applicable findings. To this end, we used surrogates rather than real gametes for the labo-

ratory experiments. The use of surrogates permits compatibility with our laser-based measurement techniques, and enables us to investigate individual gamete traits (e.g., viscosity and rheology), one at a time, in order to isolate the effect of that trait on fertilization. Xanthan gum solutions have been used successfully in previous laser-based measurements of rheological behavior in fluids [43, 5] and have been used for our experiment as well.

5.1.1 Xanthan Gum Properties

Xanthan gum is an anionic polymer derived from the bacterium Xanthomonas campestris, which can be found on cruciferous veggies like cabbage and cauliflower. One of the most remarkable properties of xanthan gum is its ability to dramatically increase the viscosity of a liquid by adding a very small quantity of gum, to the order of one percent. It is commonly added to food products at 0.5% and lower concentration.

Figure 5.1: Xanthan Gum

In Figure. 5.2 the shear viscosity versus the shear rate is given for the polymer solution Xanthan Gum with various concentrations of the additives. The viscosity of xanthan gum solutions decreases with higher shear rates; this is called shear thinning or pseudoplasticity. This means that a product subjected to shear, whether from mixing, shaking or even chewing, will thin out. However,

once the shear forces are removed, the food will thicken up again.

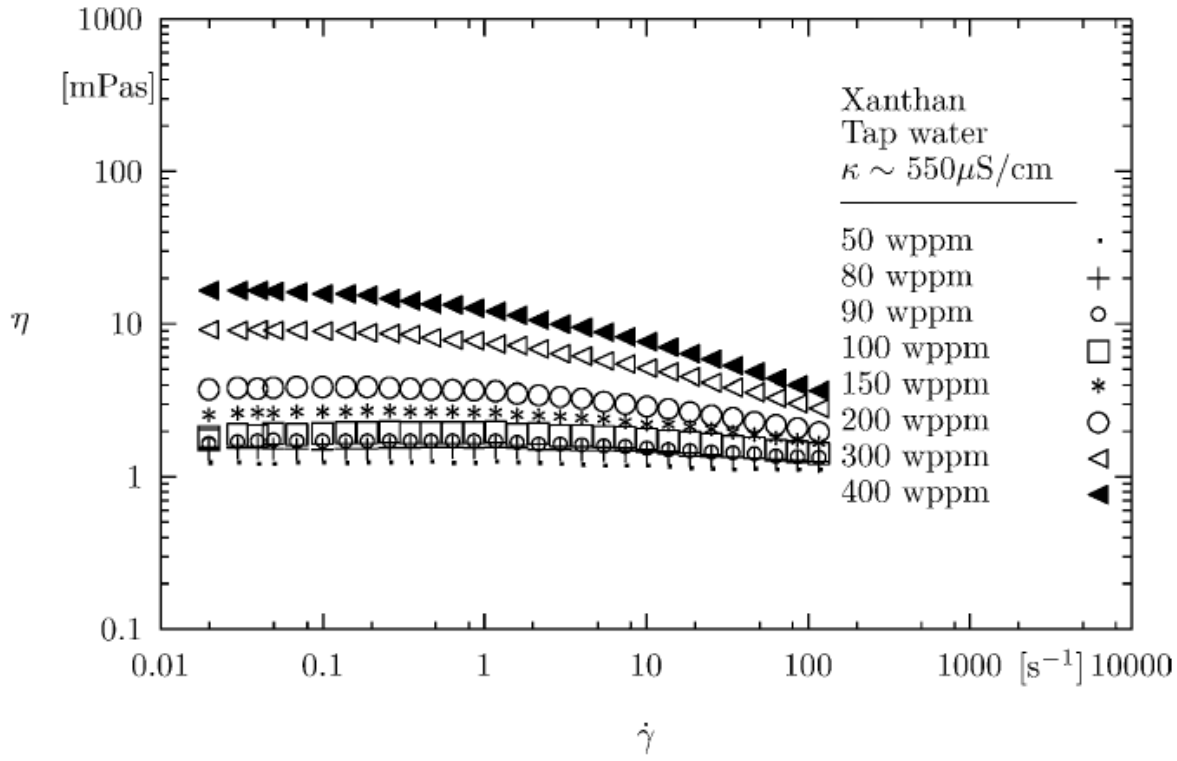

Figure 5.2: Shear Viscosity of Xanthan Gum, Gampert et al. [43]

The rheological properties of xanthan gum in both diluted and moderately concentrated solutions have been studied in the past. Xanthan gum systems demonstrate a differently complicated rheological behavior according to their concentration. Hence, in the previous works the determination of concentration regimes has been always a key parameter.

In 1978, for the first time, Whitcomb and Macosko [149] completed a comprehensive investigation on the steady shear flow properties of aqueous solutions of xanthan gum over a wide range of shear rates and concentrations. Their results showed a region of the Newtonian viscosity at low shear rates for sufficiently dilute xanthan gum solutions and exhibited a yield stress for more concentrated ones. Moreover, through modeling their intrinsic viscosity data, they guessed that the structure of xanthan gum in solution is rod-like, having some flexibility to some extent.

By contrast, Thurston and Pope [140, 141] divided the first theoretical approach on the viscoelastic properties of xanthan gum. They confirmed that for both the steady and oscillatory flow behaviors, the same relaxation processes contribute to the viscoelasticity of Xanthan gum and steady flow viscosity with shear rate.

Later, using both the steady and oscillatory shear experiments, Rochefort and Middleman [113] studied the influences of salt, temperature, and strain on the conformation of xanthan gum solutions. Their results indicated that in highly saline solution, a master curve of dynamic properties has been obtained and the frequency-temperature superposition allows a characterization of the conformational transition induced by temperature change.

Tiu et al [133, 134, 106] further investigated the steady and dynamic shear properties of dilute solutions of xanthan gum in aqueous media at different concentrations and temperatures. Both shear-thinning and elastic characteristics even at extremely low concentrations were observed in the solutions. Moreover, temperature-concentration superposition principle using reduced variables is applicable to both steady and dynamic shear data.

At moderate temperature, solutions of xanthan gum tend to exhibit a pseudoplastic behavior with high viscosity at low concentrations [145]. In comparison with temperature and pH, the concentration has a considerable effect on the rheological characteristics of xanthan gum solutions [85, 2].

5.2 Experiment Setup

Using a pharmaceutical-grade xanthan gum (Fig 5.2), we developed a technique to create surrogates that mimic the viscosity and shear-thinning rheology of the diluted gamete matrix of sea urchins (based on the data from Thomas [137]). The experiment setup is similar to the unsteady wake experiment setup. One cylindrical PVC pipe with diameter of $\phi = 4.826$ cm was used to produce unsteady obstacle wakes in flow. The tests were just conducted at one flow setting ($U_o = 4.05$ cm/s, or $Re_\phi = 2000$) at downstream location ($x = 64 - 80$). All plumes had the same source flow and dye concentration during the test. A specific volume (17000 mL) of Xanthan Gum

solution for each dye tank was made for two different concentrations (750 ppm and 1000 ppm). The room temperature and water in flume were kept constant at 22 °C.

Pulseless gear pumps were used to inject the scalars to flow. The pumps were calibrated to match the flume velocity for an isokinetic [125]. They are also calibrated for desired viscosity (0-1500 cP) range release. In order to allow plumes to have well developed turbulence, scalars were released 65 cm downstream of a turbulence-generating grid. The scalars were introduced using 2.75 m lengths of copper tubing with 0.56 cm diameter, to ensure a well developed flow profile and remove temperature fluctuations from the dye release. We have investigated the effect of gamete viscosity and non-Newtonian (shear-thinning) rheology on coalescence and fertilization using the PLIF technique, developed and validated for the unsteady wake experiments.

5.2.1 Preparation of Solutions

We used Xanthan gum as gamete surrogate to perform experiments on the effect of viscosity and rheology on gamete plume dispersion. Xanthan gum is soluble in both cold and hot water. When it mixes with an aqueous medium, like most other hydrocolloids, xanthan gum needs an intensive agitation to avoid formation of lumps [126].

In this work, xathan gum solutions with concentrations of 0.075 wt% and 0.1 wt% (750 ppm and 1000 ppm) were prepared by slowly adding the required amount of polymer powder (GRINDSTED XANTHAN 80 CLEAR, France), weighed using an electronic balance (AG204, Mettler-Toledo International, Inc., USA) into a known volume of gently agitated medium (17000 mL dust-free flume water), filled in a dye tank, which was maintained at room temperature with constant stirring using a driller mixer (18V, 3/8" Drillmaster, (Fig 5.3)) for 1 hour. After stirring, the top of a tank container was sealed to prevent an evaporation of the medium. When the polymer was perfectly dissolved and the solutions were lump-free and in order to complete the hydration of the polymer, we kept the prepared solutions at rest, at room temperature for more than 2 hours prior to conducting the rheological measurements.

(a) Mixer Shaft (b) Mixer Dril

Figure 5.3: Mixer Driller and shaft used for stirring the solution

5.3 Results and Discussions

Instantaneous PLIF images of three turbulent plumes with increasing levels of viscosity and shear-thinning behavior are shown in Fig 5.4. All three plumes have the same source flow and they are nondimensionalized to source dye concentration. All three images share the same concentration color scale. The purple filaments represents regions where mixing and overlapping occurred when the turbulence stirring brings the filaments together and continues to stretch and fold the scalar fields. The "low" viscosity plume is just an aqueous dye solution. The "medium" and "high" viscosity plumes have increasing amounts of Xanthan gum added to the plume fluid. In all three cases, the ambient fluid surrounding the plume is pure water. The effect is dramatic; the purely aqueous plume disperses rapidly and is barely visible in Fig. 5.4(a). Dispersion is dramatically reduced in Figs 5.4(b) and (c), with corresponding increases in the filament concentrations.

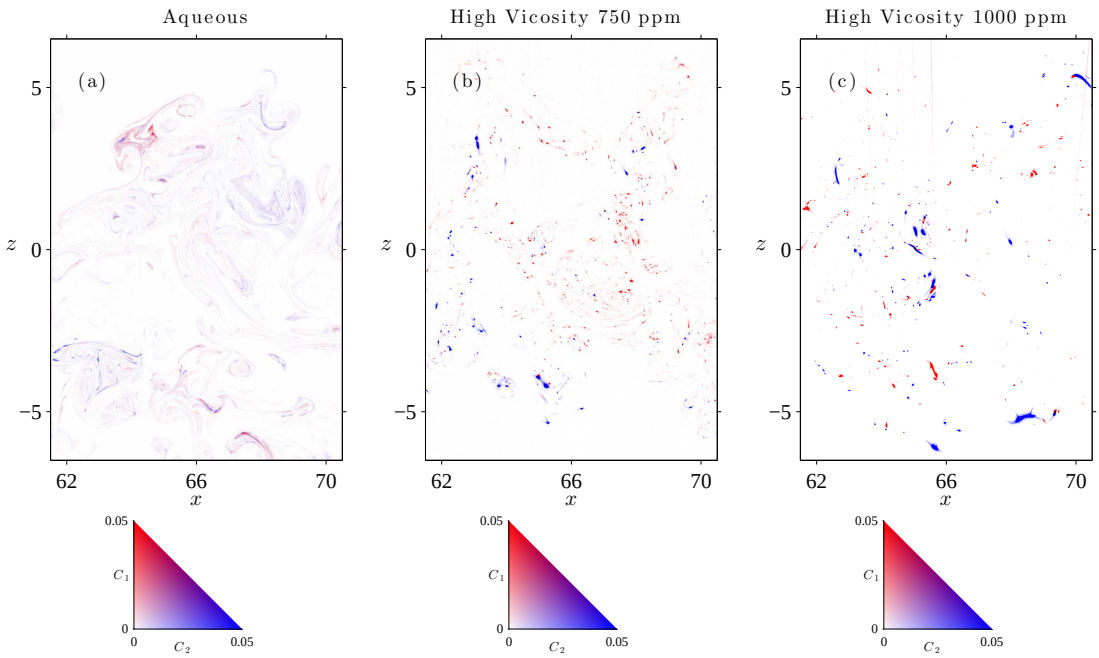

Figure 5.4: Instantaneous composite image of scalar fields C_1 (red), C_2 (Blue) in specific case: Cylinder-downstream location for (a) Aqueous (b) High viscosity 750ppm (c) High viscosity 1000ppm

The time-averaged, non-dimensional concentration profiles of the plumes at downstream location and cylinder case are shown in Fig. 5.5. Each point represents a bin of 75 pixels in z direction, and averaged spatially in the x direction and then normalized to full strength dye concentration. The mean profile is symmetric along the centerline ($z = 0$) for the aqueous case. In high viscosity case, the mean profile shape is similar to aqueous case since both scales are considered passive and they conserved the mass. They are approximately symmetric about the centerline, with a slight skew, due to the entrainment of the two plumes towards each other, especially in 1000 ppm concentration.

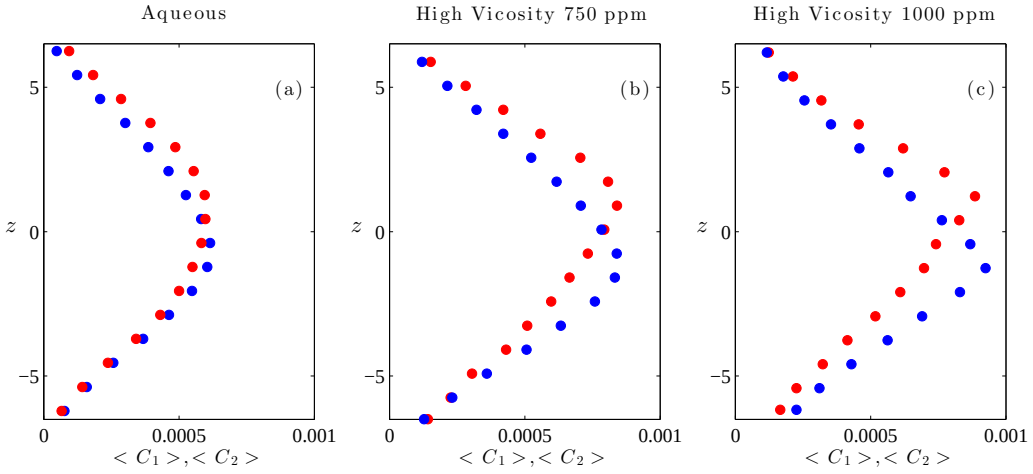

Figure 5.5: The time averaged mean profiles, $< C_1 >, < C_2 >$ for a) Aqueous b) High viscosity 750ppm c) High viscosity 1000ppm

The time-averaged, non-dimensional profiles of the RMS scalar plume fluctuations at downstream location for the cylinder case are shown in Fig. 5.6. Each point represents a bin of 75 pixels in z direction, and averaged spatially in x direction and then normalized to full strength dye concentration. Higher values are observed in the RMS profile for high viscosity cases, due to change of rheology of scalars and its corresponding flow environment, reduction of filaments' dispersion rate, and increment of filaments' concentration corresponding with aqueous case.

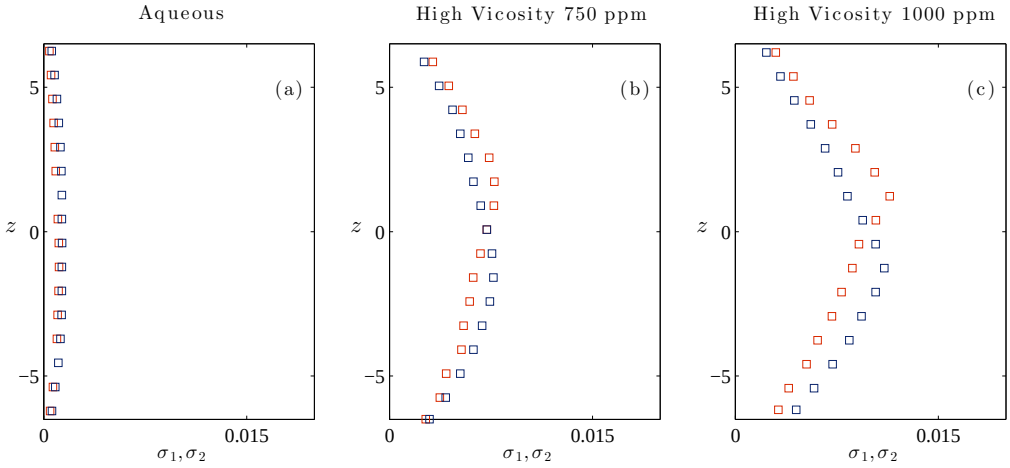

Figure 5.6: The time averaged RMS profiles, σ_1, σ_2 for a) Aqueous b) High viscosity 750ppm c) High viscosity 1000ppm

The total non-dimensional reaction, $\langle C_1 C_2 \rangle$ are shown in Fig. 5.7 for three cases. Results indicate that mixing and reaction rates in the low-Damkohler limit between the two scalars plumes increase as the viscosity of the scalars is increased. In aqueous case, the reaction plume exhibits a Non-Gaussian symmetric cross-section. However, in high viscous experiments, the viscosity and non-Newtoninan rheology of the scalars in the domain generates significant mixing enhancement up to three times higher than aqueous case, by increasing the aggregation of filaments and their concentrations. Further investigation is required to confirm whether this effect is attributable to the changes in viscosity, rheology, or both. To isolate these effects, we propose future experiments that would prepare surrogate solutions using glycerol (Fig 5.8) in addition to xanthan gum. The glycerol solutions permit viscosity to be independently increased, without simultaneously changing the rheology (that is, the glycerol solutions are Newtonian).

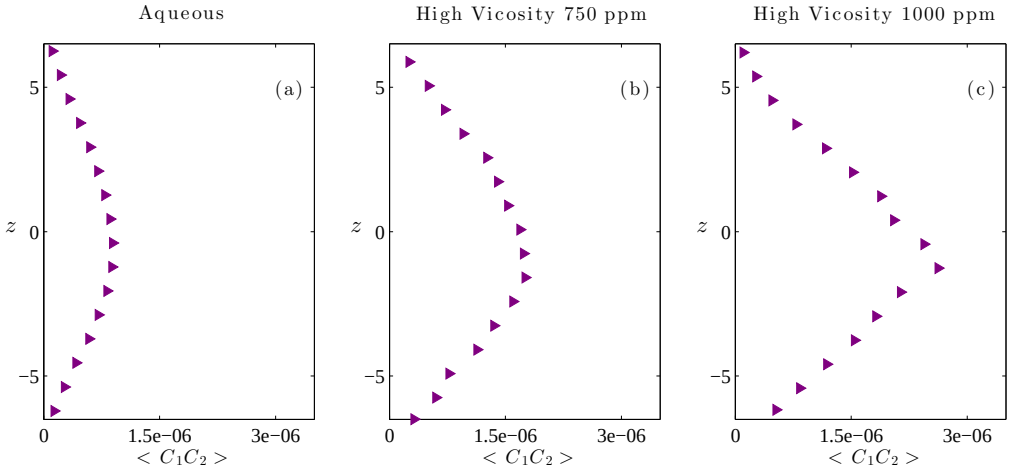

Figure 5.7: The time averaged reaction profiles, $\langle C_1C_2 \rangle$ for a) Aqueous b) High viscosity 750ppm c) High viscosity 1000ppm

Figure 5.8: Glycerol

Figure 5.9 shows the correlation coefficient, $\rho = \langle c_1' c_2' \rangle / (\sqrt{\langle c_1' \rangle^2} \sqrt{\langle c_2' \rangle^2})$ over the entire domain for three experimental setups. In the aqueous case, as the obstacle wake continues to stretch and fold the scalar fields, we see the overlap of diffused filaments over the entire domain and ρ is high and positive. In high viscosity cases, although the effect of instantaneous flow processes and particularly the covariance term is increased, due to relatively large increase in RMS values (shown in Figure 5.6, the ρ is decreased dramatically to low positive value (e.g., 0.05).

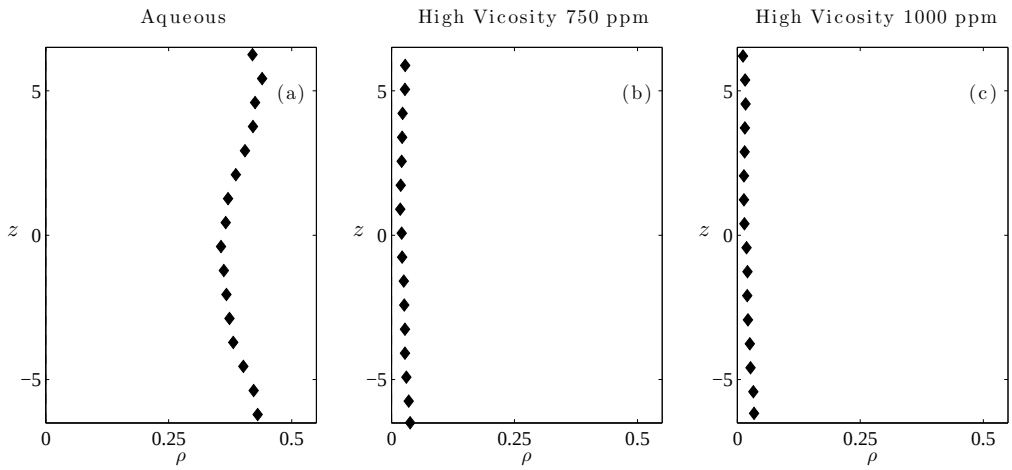

Figure 5.9: The time averaged correlation profiles, ρ for a)Aqueous b) High viscosity 750ppm c) High viscosity 1000ppm

As discussed earlier in Ch. 2, the roles of instantaneous and mean processes are compared using the segregation parameters (α and β). Hence, The beta coefficient for two high viscosity experiments with aqueous case at downstream location with the presence of the cylinder in flow appears in Fig 5.10. The study shows that the dominant contribution of total reaction derives from the scalar covariance associated with instantaneous flow processes, and depends strongly on viscosity and non-Newtonian rheology of the scalars in the domain. In other words, The contribution of instantaneous flow process (covariance term) to total reaction and mixing increases as the viscosity of the scalars is increased. The results of this study have broad implications for biological and ecological mixing processes involving now-Newtonian fluids.

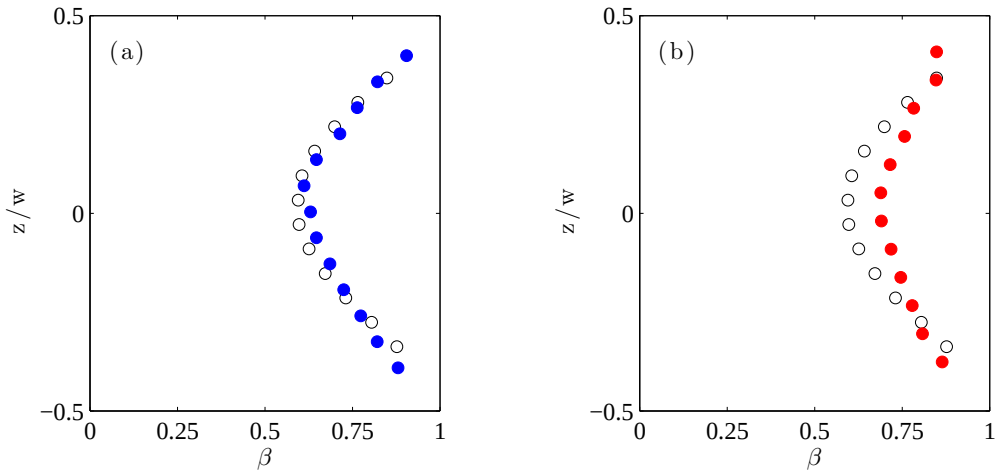

Figure 5.10: Comparison of β for (a) ∘ Aqueous vs. • High Viscosity 750 ppm and (b) ∘ Aqueous vs. • High viscosity 1000 ppm, both in cylinder case and downstream location

5.3.1 Effect of Flow Streamwise on Cylinder Wake Mixing In High Viscosity Case

The effect of viscosity and non-Newtonian (shear-thinning) rheology on mixing and reaction between two initially distant scalars has been investigated using a two-channel planar laser-induced fluorescence technique (2C-PLIF). The scalars are stirred and mixed in the mildly turbulent (Re=2000) wake of a round cylinder. Releasing the scalars continuously upstream of the cylinder, with a separation that initially impedes the reaction. The ambient flow is pure water, but the scalar solutions include Xanthan gum to alter their rheology. Results indicate that mixing and reaction rates in the low-Damkohler limit between the two scalars plumes increase with the increase in viscosity of the scalars.

Additional data was taken at upstream location ($x = 14 - 20$) to help understand the effect of flow streamwise on cylinder wake mixing at high viscosity case. The test was conducted at one flow setting (U_o = 4.05 cm/s, or Re_ϕ = 2000) and all plumes had the same source flow and dye concentration during the test. A specific volume (17000 mL) of Xanthan Gum solution for each dye tank was made for one concentration (i.e., 750 ppm).

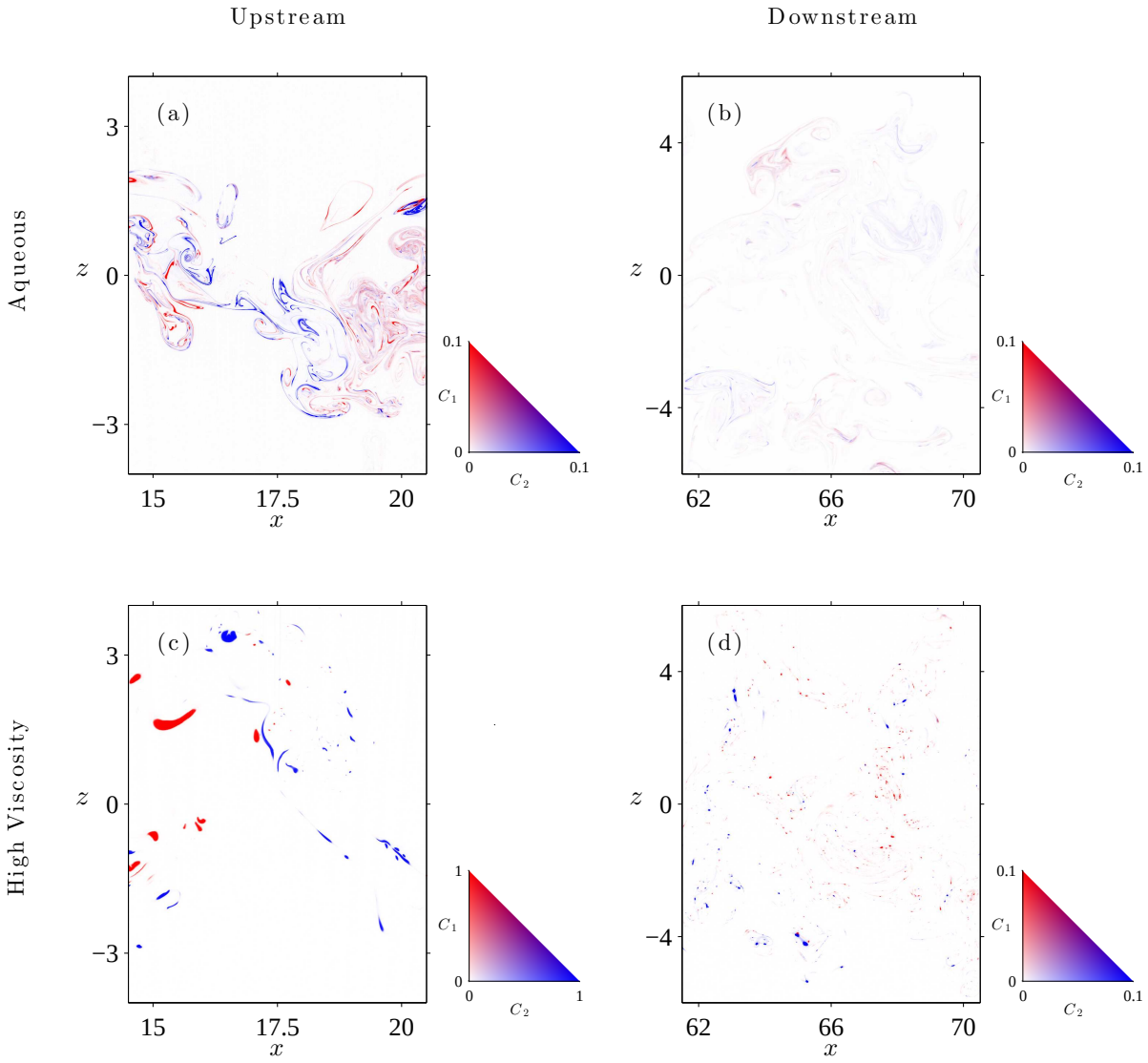

Figure 5.11: Instantaneous composite image of scalar fields C_1 (red), C_2 (Blue) for (a) Aqueous Upstream (b) Aqueous Downstream (c) High viscosity Upstream (d) High viscosity Downstream

Instantaneous distributions of concentrations C_1 and C_2 at the upstream and downstream locations shown in Fig. 5.11. The top row is for aqueous, and the bottom row is for the high viscosity 750 ppm case. The color scheme for C_1 (shades of red), C_2 (shades of blue), and various combinations of the two (shades of purple) is shown for each case. As expected, the purely aqueous plume disperses rapidly at both upstream and downstream locations and is barely visible

in Fig. 5.4(b). However, dispersion is dramatically reduced in Figs 5.11(c), with corresponding increases in the filament concentrations.

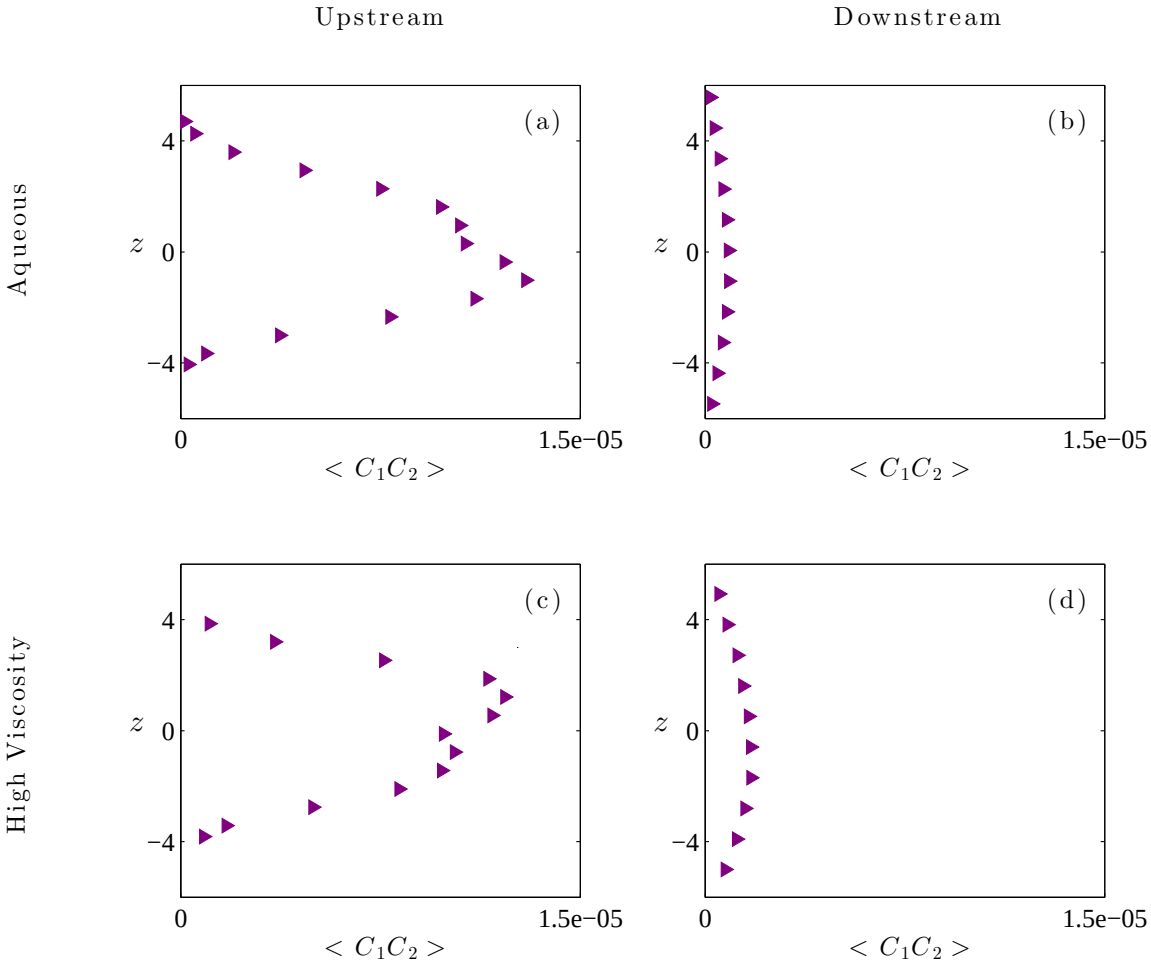

Figure 5.12: The time averaged reaction profiles, $\langle C_1C_2 \rangle$ for (a) Aqueous Upstream (b) Aqueous Downstream (c) High viscosity Upstream (d) High viscosity Downstream

The total non-dimensional reaction, $\langle C_1C_2 \rangle$ are shown in Fig. 5.12 for two aqueous and high viscosity cases. As earlier discussed, in high viscous experiments, the viscosity and non-Newtoninan rheology of the scalars in the domain generates significant mixing enhancement up to four times higher than aqueous case at downstream location, by increasing the aggregation of filaments and their concentrations. However, the reaction rate is similar to aqueous case at upstream location

shown in Fig. 5.12(c). In high viscosity case, scalars that are weakly diffusive relative to the diffusivity of momentum are characterized by a high Sc. When these weakly diffusive scalars are stirred, though the interfacial length is increased, there is a little diffusion to spread and mix the scalars, resulting in the similar reaction to aqueous case at upstream location. Whereas, a more diffuse scalar with a lower Sc disperses more readily increasing the reaction when provoked by stirring at downstream location.

Chapter 6

Synthesis

6.1 Synthesis

The research aims to determine the effect of key physical and biological factors on the fertilization rate associated with broadcast spawning in benthic invertebrates. Using a combination of analytical work and laboratory experiments, it is shown that turbulence imparts spatial correlations on two initially distant passive scalars, resulting in fertilization (reaction) enhancement. We have analytically modeled and investigated the processes that govern the magnitude and sign of the reaction and mixing terms. A novel technique have been used to do a number of investigations in various aspects of turbulent mixing in flows. The details of this two-channel technique are presented in chapter 2. This phenomenon has never been reported in the fluid mechanics literature, and it has important consequences for a range of engineered and ecological systems, including broadcast spawning. It highlights physics that have been sparsely examined due to the difficult nature of the measurements and the high caliber of data highlights our attention to detail.

The effect of turbulent wake behind a round obstacle (chapter 3) on the second-order reaction between two initially distant scalars has been investigated by a series of planar laser-induced fluorescence experiments. The scalars were released continuously, and were separated from each other by a lateral distance that initially impedes the reaction. The direct effect of the wake on mixing enhancement was determined by comparing segregation parameters for cases with and without the cylinder wake. We measured mixing statistics for variety of flow regimes, streamwise locations, and scalar release geometries. The study suggests that the presence of turbulent obstacle wakes in

spawning regions may substantially raise the efficacy of external fertilization, eventually contribute to a better understanding of marine ecology and biology. This study shows that the presence of an obstacle in spawning regions may substantially raise the contribution of instantaneous processes up to 65%. This estimate is expected to increase if lateral data in the y direction was measured, as locations away from the centerline contribute strongly towards the $< C_A C_B >$ plume.

Analytical model of scalar filament structures on mixing, reactions and segregation parameter is studied on chapter 4. We considered analytically a class of reaction problems where the two reactants are initially localized and distant from one another, separated by ambient fluid that contains neither reactant. Mechanical stirring stretches introduced scalars into thin shells (in 3D) and filaments (in 2D), increasing the interfacial area between the scalar and surrounding fluid, sharpening concentration gradients, and enhancing diffusive mixing and reactions. We made a simple 1-D idealized model of a representative slice across two symmetric and Gaussian representative filaments to investigate analytically the effect of their physical characteristics such as filament width, filament separation (s^*) and spatially domain averaged filament concentration (h^*) on fluctuating concentration fields. Results showed that the segregation parameter changes directly with changes of (h^*) and decreases with increase of (s^*). It is also estimated that dimensionally, due to variation of filaments profile shape from Gaussian to Non-Gaussian, the segregation parameter increases dramatically.

The effect of gamete viscosity and non-Newtonian (shear-thinning) rheology on coalescence and fertilization (chapter 5) has been investigated using that technique developed and validated for the unsteady wake experiments. Using a pharmaceutical-grade biopolymer called xanthan gum as gamete surrogates, we have developed a technique to observe the effect of viscosity and rheology on gamete plume dispersion. PLIF images of turbulent plumes with increasing levels of viscosity and shear-thinning behavior indicate that mixing and reaction rates in the low-Damkohler limit between the two scalars plumes increase with the increase in viscosity of the scalars. This study also showed that the dominant contribution of the total reaction derives from the scalar covariance associated with instantaneous flow processes, and depends strongly on viscosity and non-Newtonian rheology

of the scalars in the domain. The results of this study have broad implications for biological and ecological mixing processes involving now-Newtonian fluids.

6.2 Future Recommendations

6.2.1 Characterization And Analysis of Velocity Field Beyond The Obstacle Wake

Although turbulence statistics are typically calculated in the time domain for the sake of convenience, an evaluation of the spatial, temporal, and noise characteristics of data from a particular technique can be more conveniently examined in the frequency domain. The power spectral density (PSD) calculation (e.g., [6]) converts the time history of a statistic into frequency space, showing how contributions to the variance are distributed with respect to their frequency (or wavelength) content. In a spectral representation of flow characteristics, there is a relationship between frequency and eddy size. It is recommended to measure the power spectral densities of the streamwise and vertical components of all flow cases in cylinder mixing experiments to estimate the related integral length scale of the turbulent process which affects scalar covariance and instantaneous processes. It is made clear in the cylinder mixing experiments that presence of cylinder plays an important role in determining the sign and magnitude of the scalar covariance.

6.2.2 Numerical Simulations of Gamete Distribution And Fertilization Success

The process-level role of structured turbulence on gamete coalescence can be simulated and investigated numerically as well. The effect of obstacle wakes can be modeled using the Lagrangian particle-tracking approach utilizing an analytic approximation to the cylinder wake or using the full governing PDEs for flow and transport utilizing the COMSOL multiphysics modeling environment. Either way used, The effect of the following parameters on gamete distribution and fertilization rates will be suggested: (1) geometry and separation of initial egg and sperm blobs, (2) obstacle geometry, including arrays of obstacles, (3) Reynolds number, which determines the nature of the vortex shedding, (4) sperm taxis, and (5) gamete viscosity and rheology. For latter, a wide range

of viscosity and rheology parameters that span the sea urchin data (e.g., [59]) can be used. The numerical simulations results can be directly compared with companion flume experiments using high-viscosity and non-Newtonian gamete surrogates discussed in chapter 5.

6.2.3 Future Experiments

The effect of different gamete traits on gamete coalescence and fertilization in turbulent benthic boundary layers can be investigated experimentally in the flume. The suggested experiments can be for different flow speeds within the range of typical turbulent benthic boundary layers, for example different bed roughness levels, or with and without surface waves effect. The surface wave experiments can be done with and without bottom roughness to investigate the effect of the known nonlinear interaction between the two. The effect of surface-penetrating obstacles as well as surface waves on the evolution of the spatial gamete correlations can be suggested as well. When designing these experiments, quantification of the length-scales of the turbulent structures will govern the choices of scalar spacing such that the effect of length scales can be quantified.

In high viscous experiments, we observed that the viscosity and non-Newtoninan rheology of the scalars in the domain generates significant mixing enhancement by increasing the aggregation of filaments and their concentrations. Further investigation is required to confirm whether this effect is attributable to the changes in viscosity, rheology, or both. To isolate these effects, we propose future experiments that would prepare surrogate solutions using glycerol in addition to xanthan gum. The glycerol solutions permit viscosity to be independently increased, without simultaneously changing the rheology (that is, the glycerol solutions are Newtonian).

Finally, it has been shown that the scalar field dominates away from the centerline of the two isolated scalars. Three-dimensional quantification of the scalar fields would be useful in determining the net role of the instantaneous quantities towards the scalar overlap.

Bibliography

[1] RJ Adrian, KT Christensen, and Z-C Liu. Analysis and interpretation of instantaneous turbulent velocity fields. Experiments in flsuids, 29(3):275–290, 2000.

[2] Jasim Ahmed and H. S. Ramaswamy. Effect of high-hydrostatic pressure and concentration on rheological characteristics of xanthan gum. Food Hydrocolloids, 18(3):367–373, 2004.

[3] B. Andersson, K. Gustavsson, B. Mehlig, and M. Wilkinson. Advective collisions. EPL (Europhysics Letters), 80:69001, 2007.

[4] R. Babcock. Synchronous multispecific spawning on coral reefs: potential for hybridization and roles of gamete recognition. Reproduction, Fertility and Development, 7(4):943–950, 1995.

[5] Nicolas Benard, Sebastien Jarny, Damien Coisne, et al. Definition of an experimental blood like fluid for laser measurements in cardiovascular studies. Applied Rheology, 17(4):44251, 2007.

[6] Julius S Bendat and Allan G Piersol. Random data analysis and measurement procedures. Measurement Science and Technology, 11(12):1825, 2000.

[7] A. Bennani, J. N. Gence, and J. Mathieu. The influence of a grid-generated turbulence on the development of chemical reactions. AIChE journal, 31(7):1157–1166, 1985.

[8] R. W. Bilger. Turbulent diffusion flames. Annual Review of Fluid Mechanics, 21(1):101–135, 1989.

[9] R. W. Bilger, N. R. Mudford, and J. D. Atkinson. Comments on turbulent effects on the chemical reaction for a jet in a nonturbulent stream and for a plume in a grid-generated turbulence[phys. fluids [bold 2][bold 7], 77 (1984)]. Physics of Fluids, 28:3175, 1985.

[10] M Susan Bloor. The transition to turbulence in the wake of a circular cylinder. Journal of Fluid Mechanics, 19(02):290–304, 1964.

[11] S. H. Brawley. Fertilization in natural populations of the dioecious brown alga fucus ceranoides and the importance of the polyspermy block. Marine Biology, 113(1):145–157, 1992. ISSN 0025-3162.

[12] R. Breidenthal. Structure in turbulent mixing layers and wakes using a chemical reaction. Journal of Fluid Mechanics, 109:1–24, 1981.

[13] E. W. Byrd and F. D. Collins. Absence of fast block to polyspermy in eggs of sea urchin strongylocentrotus purpuratus. 1975.

[14] Bayram Celik and Ali Beskok. Mixing induced by a transversely oscillating circular cylinder in a straight channel. Physics of Fluids (1994-present), 21(7):073601, 2009.

[15] J. C. Coll, P. A. Leone, B. F. Bowden, A. R. Carroll, G. M. König, A. Heaton, R. Nys, M. Maida, P. M. Alino, and R. H. Willis. Chemical aspects of mass spawning in corals. ii.(-)-epi-thunbergol, the sperm attractant in the eggs of the soft coral lobophytum crassum (cnidaria: Octocorallia). Marine Biology, 123(1):137–143, 1995.

[16] R. Coma and H. R. Lasker. Small-scale heterogeneity of fertilization success in a broadcast spawning octocoral. Journal of experimental marine biology and ecology, 214(1-2):107–120, 1997.

[17] R. T. Counihan, D. C. McNamara, D. C. Souter, E. J. Jebreen, N. P. Preston, C. R. Johnson, and B. M. Degnan. Pattern, synchrony and predictability of spawning of the tropical abalone haliotis asinina from heron reef, australia. Marine Ecology Progress Series, 213:193–202, 2001.

[18] M Coutanceau and R Bouard. Experimental determination of the main features of the viscous flow in the wake of a circular cylinder in uniform translation. part 2. unsteady flow. Journal of Fluid Mechanics, 79:257–272, 1977.

[19] J. R. Cressman, J. Davoudi, W. I. Goldburg, and J. Schumacher. Eulerian and lagrangian studies in surface flow turbulence. New Journal of Physics, 6:53, 2004.

[20] J. P. Crimaldi. Planar laser induced fluorescence in aqueous flows. Exp in Fluids, 44(6):851–863, 2008. doi: 10.1007/s00348-008-0496-2. URL `http://www.springerlink.com/index/94V57048504V21PN.pdf`.

[21] J. P. Crimaldi and H. S. Browning. A proposed mechanism for turbulent enhancement of broadcast spawning efficiency. Journal of Marine Systems, 49(1-4):3–18, 2004. ISSN 0924-7963. doi: 10.1016/j.jmarsys.2003.06.005.

[22] J. P. Crimaldi, J. R. Hartford, and J. B. Weiss. Reaction enhancement of point sources due to vortex stirring. Physical Review E, 74(1):016307, 2006.

[23] John P. Crimaldi and Tanaya R. Kawakami. Reaction of initially distant scalars in a cylinder wake. Physics of Fluids (1994-present), 25(5):053604, 2013.

[24] John P Crimaldi, Jillian R Cadwell, and Jeffrey B Weiss. Reaction enhancement of isolated scalars by vortex stirring. Physics of Fluids, 20:073605, 2008.

[25] Gabriel T. Csanady. Turbulent diffusion in the environment. Number 3. Springer, 1973.

[26] P. V. Danckwerts. The definition and measurement of some characteristics of mixtures. Applied Scientific Research, 3(4):279–296, 1952.

[27] P. Denissenko, G. Falkovich, and S. Lukaschuk. How waves affect the distribution of particles that float on a liquid surface. Physical review letters, 97(24):244501, 2006.

[28] M. Denny, J. Dairiki, and S. Distefano. Biological consequences of topography on wave-swept rocky shores: I. enhancement of external fertilization. The Biological Bulletin, 183(2):220, 1992.

[29] M. W. Denny. Biology and the mechanics of the wave-swept environment. Princeton University Press Princeton, New Jersey, USA, 1988.

[30] M. W. Denny and M. F. Shibata. Consequences of surf-zone turbulence for settlement and external fertilization. American Naturalist, 134(6):859–889, 1989. ISSN 0003-0147.

[31] M. W. Denny, E. K. Nelson, and K. S. Mead. Revised estimates of the effects of turbulence on fertilization in the purple sea urchin, strongylocentrotus purpuratus. The Biological Bulletin, 203(3):275, 2002.

[32] S. R. Deshmukh and D. G. Vlachos. Novel micromixers driven by flow instabilities: Application to post-reactors. AIChE journal, 51(12):3193–3204, 2005.

[33] Daniel E Dombroski and John P Crimaldi. The accuracy of acoustic doppler velocimetry measurements in turbulent boundary layer flows over a smooth bed. Limnol. Oceanogr.: Methods, 5:23–33, 2007.

[34] Changming Dong and James C. McWilliams. A numerical study of island wakes in the southern california bight. Continental Shelf Research, 27(9):1233–1248, 2007.

[35] Changming Dong, James C. McWilliams, and Alexander F. Shchepetkin. Island wakes in deep water. Journal of Physical Oceanography, 37(4):962–981, 2007.

[36] J. E. Eckman. A model of passive settlement by planktonic larvae onto bottoms of differing roughness. Limnology and Oceanography, pages 887–901, 1990.

[37] J. E. Eckman. Closing the larval loop: linking larval ecology to the population dynamics of marine benthic invertebrates. Journal of Experimental Marine Biology and Ecology, 200 (1-2):207–237, 1996.

[38] T. Elperin, N. Kleeorin, M. A. Liberman, V. S. Lvov, and I. Rogachevskii. Clustering of aerosols in atmospheric turbulent flow. Environmental Fluid Mechanics, 7(2):173–193, 2007.

[39] G. S. Farley and D. R. Levitan. The role of jelly coats in sperm-egg encounters, fertilization success, and selection on egg size in broadcast spawners. American Naturalist, pages 626–636, 2001. ISSN 0003-0147.

[40] G Ferrier, PA Davies, and JM Anderson. Cover remote sensing observations of a vortex street downstream of an obstacle in an estuarine flow. International Journal of Remote Sensing, 17 (1):1–8, 1996.

[41] E. S. Franke, R. C. Babcock, and C. A. Styan. Sexual conflict and polyspermy under sperm-limited conditions: in situ evidence from field simulations with the free-spawning marine echinoid evechinus chloroticus. American Naturalist, 160(4):485–496, 2002. ISSN 0003-0147.

[42] A. M. Froncioni, F. J. Muzzio, R. L. Peskin, and P. D. Swanson. Chaotic motion of fluid and solid particles in plane wakes. Chaos, Solitons & Fractals, 8(1):109–130, 1997.

[43] B Gampert, T Braemer, T Eich, and T Dietmann. Rheo-optical investigations and near-wall turbulence structure of polymer solutions in turbulent channel flow. Journal of non-newtonian fluid mechanics, 126(2):115–121, 2005.

[44] B. Gaylord. Hydrodynamic context for considering turbulence impacts on external fertilization. The Biological Bulletin, 214(3):315, 2008. doi: Hydrodynamic.

[45] B. Gaylord, D. C. Reed, P. T. Raimondi, L. Washburn, and S. R. McLean. A physically based model of macroalgal spore dispersal in the wave and current-dominated nearshore. Ecology, 83(5):1239–1251, 2002. ISSN 0012-9658.

[46] JH Gerrard. The wakes of cylindrical bluff bodies at low reynolds number. Philosophical Transactions for the Royal Society of London. Series A, Mathematical and Physical Sciences, pages 351–382, 1978.

[47] A. C. Giese and J. S. Pearse. Reproduction of marine invertebrates: 2. Entoprocts and lesser Coelomates, volume 2. 1975.

[48] R. Gordon and S. H. Brawley. Effects of water motion on propagule release from algae with complex life histories. Marine Biology, 145(1):21–29, 2004. ISSN 0025-3162.

[49] J. Gray. The movement of sea-urchin spermatozoa. Journal of Experimental Biology, 32(4): 775, 1955.

[50] J. R. Guest, A. H. Baird, B. P. L. Goh, and L. M. Chou. Seasonal reproduction in equatorial reef corals. Invertebrate reproduction & development, 48(1):207–218, 2005.

[51] Frédéric Guichard and Edwin Bourget. Topographic heterogeneity, hydrodynamics, and benthic community structure: a scale-dependent cascade. Marine Ecology Progress Series, 171: 59–70, 1998.

[52] J. F. Hamel and A. Mercier. Gamete dispersion and fertilisation success of the sea cucumber cucumaria frondosa. SPC Beche-de-mer Information Bulletin, 8:34–40, 1996.

[53] P. L. Harrison and C. C. Wallace. Reproduction, dispersal and recruitment of scleractinian corals. Ecosystems of the world, 25:133–207, 1990.

[54] P. L. Harrison, R. C. Babcock, G. D. Bull, J. K. Oliver, C. C. Wallace, and B. L. Willis. Mass spawning in tropical reef corals. Science, 223(4641):1186, 1984. ISSN 0036-8075.

[55] D. Hasegawa, H. Yamazaki, R. G. Lueck, and L. Seuront. How islands stir and fertilize the upper ocean. Geophysical research letters, 31(16), 2004.

[56] Daisuke Hasegawa, Hidekatsu Yamazaki, Takashi Ishimaru, Hideki Nagashima, and Yoshio Koike. Apparent phytoplankton bloom due to island mass effect. Journal of Marine Systems, 69(3):238–246, 2008.

[57] James K Helgesen and Michael J Matteson. Particle mixing and diffusion in the turbulent wake of a single cylinder. Aerosol science and technology, 20(1):111–126, 1994.

[58] Karen J. Heywood, Eric D. Barton, and John H. Simpson. The effects of flow disturbance by an oceanic island. Journal of Marine Research, 48(1):55–73, 1990.

[59] F. IM THOMAS. Physical properties of gametes in three sea urchin species. J. exp. Biol, 194:263–284, 1994.

[60] T. M. Jantzen, R. De Nys, and J. N. Havenhand. Fertilization success and the effects of sperm chemoattractants on effective egg size in marine invertebrates. Marine Biology, 138 (6):1153–1161, 2001.

[61] A. Juneja and S. B. Pope. A dns study of turbulent mixing of two passive scalars. Physics of Fluids, 8:2161, 1996.

[62] C. Jung, T. Tél, and E. Ziemniak. Application of scattering chaos to particle transport in a hydrodynamical flow. Chaos: An Interdisciplinary Journal of Nonlinear Science, 3(4): 555–568, 1993.

[63] György Károlyi, Áron Péntek, Zoltán Toroczkai, Tamás Tél, and Celso Grebogi. Chemical or biological activity in open chaotic flows. Physical Review E, 59(5):5468, 1999.

[64] György Károlyi, Áron Péntek, István Scheuring, Tamás Tél, and Zoltán Toroczkai. Chaotic flow: the physics of species coexistence. Proceedings of the National Academy of Sciences, 97(25):13661–13665, 2000.

[65] E. G. Kastrinakis and S. G. Nychas. Mixing at high schmidt numbers in the near wake of a circular cylinder. Chemical engineering science, 53(23):3977–3989, 1998.

[66] EG Kastrinakis and SG Nychas. Mixing at high Schmidt numbers in the near wake of a circular cylinder. Chemical Engineering Science, 53(23), 1998. URL `http://linkinghub.elsevier.com/retrieve/pii/S0009250998002024`.

[67] E. F. Keller and L. A. Segel. Model for chemotaxis. Journal of Theoretical Biology, 30(2): 225–234, 1971.

[68] A. Kiselev and L. Ryzhik. Biomixing by chemotaxis and enhancement of biological reactions. Arxiv preprint arXiv:1101.2440, 2011.

[69] S. Komori, J. C. R. Hunt, T. Kanzaki, and Y. Murakami. The effects of turbulent mixing on the correlation between two species and on concentration fluctuations in non-premixed reacting flows. Journal of fluid mechanics, 228(1):629–659, 1991.

[70] S. Komori, T. Kanzaki, and Y. Murakami. Simultaneous measurements of instantaneous concentrations of two reacting species in a turbulent flow with a rapid reaction. Physics of Fluids A: Fluid Dynamics, 3:507, 1991.

[71] K. J. Larson. Riding langmuir circulations and swimming in circles: a novel form of clustering behavior by the scyphomedusalinuche unguiculata. Marine Biology, 112(2):229–235, 1992.

[72] J. S. Lauzon-Guay and R. E. Scheibling. Importance of spatial population characteristics on the fertilization rates of sea urchins. The Biological Bulletin, 212(3):195, 2007.

[73] D. R. Levitan. The importance of sperm limitation to the evolution of egg size in marine invertebrates. American Naturalist, 141(4):517–536, 1993. ISSN 0003-0147.

[74] D. R. Levitan. The ecology of fertilization in free-spawning invertebrates. CRC Marine Science Series, 6, 1995.

[75] D. R. Levitan. Density-dependent sexual selection in external fertilizers: variances in male and female fertilization success along the continuum from sperm limitation to sexual conflict in the sea urchin strongylocentrotus franciscanus. American Naturalist, 164(3):298–309, 2004. ISSN 0003-0147.

[76] D. R. Levitan. Sex-specific spawning behavior and its consequences in an external fertilizer. American Naturalist, 165(6):682–694, 2005. ISSN 0003-0147.

[77] D. R. Levitan. The relationship between egg size and fertilization success in broadcast-spawning marine invertebrates. Integrative and Comparative Biology, 46(3):298, 2006.

[78] D. R. Levitan and S. D. Irvine. Fertilization selection on egg and jelly-coat size in the sand dollar dendraster excentricus. Evolution, 55(12):2479–2483, 2001. ISSN 0014-3820.

[79] D. R. Levitan and C. M. Young. Reproductive success in large populations: empirical measures and theoretical predictions of fertilization in the sea biscuit clypeaster rosaceus. Journal of Experimental Marine Biology and Ecology, 190(2):221–241, 1995.

[80] D. R. Levitan, M. A. Sewell, and F. S. Chia. Kinetics of fertilization in the sea urchin strongylocentrotus franciscanus: interaction of gamete dilution, age, and contact time. The Biological Bulletin, 181(3):371, 1991.

[81] D. R. Levitan, H. Fukami, J. Jara, D. Kline, T. M. McGovern, K. E. McGhee, C. A. Swanson, and N. Knowlton. Mechanisms of reproductive isolation among sympatric broadcast-spawning corals of the montastraea annularis species complex. Evolution, 58(2):308–323, 2004. ISSN 0014-3820.

[82] J. D. Li and R. W. Bilger. The diffusion of conserved and reactive scalars behind line sources in homogeneous turbulence. Journal of Fluid Mechanics, 318:339–372, 1996.

[83] S. Lukaschuk, P. Denissenko, and G. Falkovich. Clustering of floating particles by surface waves. Journal of Low Temperature Physics, 145(1):297–310, 2006. doi: 10.1007/s10909-006-9238-0.

[84] K. W. Mao and H. L. Toor. Second-order chemical reactions with turbulent mixing. Industrial & Engineering Chemistry Fundamentals, 10(2):192–197, 1971.

[85] Michèle Marcotte, Ali R. Taherian Hoshahili, and H. S. Ramaswamy. Rheological properties of selected hydrocolloids as a function of concentration and temperature. Food Research International, 34(8):695–703, 2001.

[86] D. J. Marshall. In situ measures of spawning synchrony and fertilization success in an intertidal, free-spawning invertebrate. Marine Ecology Progress Series, 236:113–119, 2002. ISSN 0171-8630.

[87] D. J. Marshall, C. A. Styan, and M. J. Keough. Intraspecific co-variation between egg and body size affects fertilisation kinetics of free-spawning marine invertebrates. Marine Ecology Progress Series, 195:305–309, 2000. ISSN 0171-8630.

[88] D. J. Marshall, D. Semmens, and C. Cook. Consequences of spawning at low tide: limited gamete dispersal for a rockpool anemone. Marine Ecology Progress Series, 266:135–142, 2004. ISSN 0171-8630.

[89] F. S. McEuen. Spawning behaviors of northeast pacific sea cucumbers (holothuroidea: Echinodermata). Marine Biology, 98(4):565–585, 1988.

[90] K. S. Mead and M. W. Denny. The effects of hydrodynamic shear stress on fertilization and early development of the purple sea urchin strongylocentrotus purpuratus. The Biological Bulletin, 188(1):46, 1995.

[91] Jianchun Mi, Y. Zhou, and G. J. Nathan. The effect of reynolds number on the passive scalar field in the turbulent wake of a circular cylinder. Flow, turbulence and combustion, 72(2-4): 311–331, 2004.

[92] R. B. Millar and M. J. Anderson. The kinetics of monospermic and polyspermic fertilization in free-spawning marine invertebrates. Journal of theoretical biology, 224(1):79–85, 2003.

[93] R. L. Miller. Demonstration of sperm chemotaxis in echinodermata: Asteroidea, holothuroidea, ophiuroidea. Journal of Experimental Zoology, 234(3):383–414, 1985.

[94] R. L. Miller. Specificity of sperm chemotaxis among great barrier reef shallow-water holothurians and ophiuroids. Journal of Experimental Zoology, 279(2):189–200, 1997.

[95] S. W. Moore. Scrambled eggs: mechanical forces as ecological factors in early development. Evolution & Development, 5(1):61–66, 2003. ISSN 1525-142X.

[96] N. R. Mudford and R. W. Bilger. Examination of closure models for mean chemical reaction rate using experimental results for an isothermal turbulent reacting flow. In Symposium (International) on Combustion, volume 20, pages 387–394. Elsevier, 1985.

[97] Thomas C. Niederkorn and Julio M. Ottino. Chaotic mixing of shear-thinning fluids. AIChE journal, 40(11):1782–1793, 1994.

[98] P. J. W. Olive. Annual breeding cycles in marine invertebrates and environmental temperature: probing the proximate and ultimate causes of reproductive synchrony. Journal of Thermal Biology, 20(1-2):79–90, 1995.

[99] J. Oliver and R. Babcock. Aspects of the fertilization ecology of broadcast spawning corals: sperm dilution effects and in situ measurements of fertilization. The Biological Bulletin, 183 (3):409, 1992.

[100] J. K. Oliver and B. L. Willis. Coral-spawn slicks in the great barrier reef: preliminary observations. Marine Biology, 94(4):521–529, 1987.

[101] G. A. Pearson and S. H. Brawley. Reproductive ecology of fucus distichus (phaeophyceae): an intertidal alga with successful external fertilization. Marine ecology progress series. Oldendorf, 143(1):211–223, 1996.

[102] G. A. Pearson and E. A. Serrao. Revisiting synchronous gamete release by fucoid algae in the intertidal zone: fertilization success and beyond? Integrative and Comparative Biology, 46(5):587, 2006. ISSN 1540-7063.

[103] G. A. Pearson, E. A. Serra o, and S. H. Brawley. Control of gamete release in fucoid algae: sensing hydrodynamic conditions via carbon acquisition. Ecology, 79(5):1725–1739, 1998. ISSN 0012-9658.

[104] G. A. Pearson, E. A. Serrão, M. Dring, and R. Schmid. Blue-and green-light signals for gamete release in the brown alga, silvetia compressa. Oecologia, 138(2):193–201, 2004. ISSN 0029-8549.

[105] G. B. Picken and D. Allan. Invertebrate reproduction: Unique limpet spawning behaviour. 1983.

[106] Anthony K. Podolsak, Carlos Tiu, Takashi Saeki, and Hiromoto Usui. Rheological properties and some applications for rhamsan and xanthan gum solutions. Polymer international, 40 (3):155–167, 1996.

[107] R. D. Podolsky. Life-history consequences of investment in free-spawned eggs and their accessory coats. American Naturalist, 163(5):735–753, 2004. ISSN 0003-0147.

[108] J. A. Pyle and A. M. Zavody. The modelling problems associated with spatial averaging. Quarterly Journal of the Royal Meteorological Society, 116(493):753–766, 1990.

[109] H Rehab, RA Antonia, and L Djenidi. Streamwise evolution of a high-schmidt-number passive scalar in a turbulent plane wake. Experiments in fluids, 31(2):186–192, 2001.

[110] Kelvin J Richards and Stuart J Brentnall. The impact of diffusion and stirring on the dynamics of interacting populations. Journal of theoretical biology, 238(2):340–347, 2006.

[111] KJ Richards. Physical processes in the benthic boundary layer. Philosophical Transactions of the Royal Society of London. Series A, Mathematical and Physical Sciences, 331(1616): 3–13, 1990.

[112] J. A. Riffell and R. K. Zimmer. Sex and flow: the consequences of fluid shear for sperm-egg interactions. JOURNAL OF EXPERIMENTAL BIOLOGY, 210(20):3644, 2007. ISSN 0022-0949.

[113] Willie E. Rochefort and Stanley Middleman. Rheology of xanthan gum: salt, temperature, and strain effects in oscillatory and steady shear experiments. Journal of Rheology (1978-present), 31(4):337–369, 1987.

[114] Mathias Sandulescu, Cristóbal López, Emilio Hernández-García, and Ulrike Feudel. Plankton blooms in vortices: The role of biological and hydrodynamic time scales. arXiv preprint arXiv:0802.3973, 2008.

[115] B. L. Sawford, C. C. Frost, and T. C. Allan. Atmospheric boundary-layer measurements of concentration statistics from isolated and multiple sources. Boundary-Layer Meteorology, 31 (3):249–268, 1985.

[116] IstvÁn Scheuring, GyÖrgy KÁrolyi, Áron PÉntek, TamÁs TÉl, and ZoltÁn Toroczkai. A model for resolving the plankton paradox: coexistence in open flows. Freshwater Biology, 45 (2):123–132, 2000.

[117] István Scheuring, György Károlyi, Zoltán Toroczkai, Tamás Tél, and Áron Péntek. Competing populations in flows with chaotic mixing. Theoretical population biology, 63(2):77–90, 2003.

[118] J. Schumacher and B. Eckhardt. Clustering dynamics of lagrangian tracers in free-surface flows. Physical Review E, 66(1):017303, 2002.

[119] A. Scott and P. L. Harrison. Embryonic and larval development of the host sea anemones entacmaea quadricolor and heteractis crispa. The Biological Bulletin, 213(2):110, 2007.

[120] E. A. Serrão and J. Havenhand. Fertilization strategies. Marine Hard Bottom Communities, pages 149–164, 2009.

[121] E. A. SERRao, G. Pearson, L. Kautsky, and S. H. Brawley. Successful external fertilization in turbulent environments. Proceedings of the National Academy of Sciences of the United States of America, 93(11):5286, 1996.

[122] E. A. Serrao, S. H. Brawley, J. Hedman, L. Kautsky, and G. Samuelsson. Reproductive success of fucus vesiculosus (phaeophyceae) in the baltic sea. Journal of Phycology, 35(2): 254–269, 1999.

[123] R. A. Shaw. Particle-turbulence interactions in atmospheric clouds. Annual review of fluid mechanics, 35(1):183–227, 2003.

[124] P. Singh and D. D. Joseph. Fluid dynamics of floating particles. Journal of Fluid Mechanics, 530(-1):31–80, 2005.

[125] M. A. Soltys and J. P. Crimaldi. Scalar interactions between parallel jets measured using a two-channel PLIF technique. Experiments in Fluids, December 2010. ISSN 0723-4864. doi: 10.1007/s00348-010-1019-5. URL `http://www.springerlink.com/index/10.1007/s00348-010-1019-5`.

[126] Ki-Won . W. Song, Yong-Seok . S. Kim, and Gap-Shik . S. Chang. Rheology of concentrated xanthan gum solutions: Steady shear flow behavior. Fibers and Polymers, 7(2):129–138, 2006.

[127] M. Starr, J. H. Himmelman, and J. C. Therriault. Direct coupling of marine invertebrate spawning with phytoplankton blooms. Science, 247(4946):1071, 1990. ISSN 0036-8075.

[128] C. A. Styan. Polyspermy, egg size, and the fertilization kinetics of free-spawning marine invertebrates. American Naturalist, 152(2):290–297, 1998. ISSN 0003-0147.

[129] C. A. Styan and A. J. Butler. Fitting fertilisation kinetics models for free-spawning marine invertebrates. Marine biology, 137(5):943–951, 2000. ISSN 0025-3162.

[130] C. A. Styan, M. Byrne, and E. Franke. Evolution of egg size and fertilisation efficiency in sea stars: large eggs are not fertilised more readily than small eggs in the genus patiriella (echinodermata: Asteroidea). Marine Biology, 147(1):235–242, 2005.

[131] B Mutlu Sumer and Jørgen Fredsøe. Hydrodynamics around cylindrical structures, volume 12. World Scientific, 1997.

[132] I. B. Svane and J. N. Havenhand. Spawning and dispersal in ciona intestinalis (l.). Marine Ecology, 14(1):53–66, 1993.

[133] K. C. Tam and C. Tiu. Steady and dynamic shear properties of aqueous polymer solutions. Journal of Rheology (1978-present), 33(2):257–280, 1989.

[134] K. C. Tam and C. Tiu. Improved correlation for shear-dependent viscosity of polyelectrolyte solutions. Journal of non-newtonian fluid mechanics, 46(2):275–288, 1993.

[135] L. Tang, F. Wen, Y. Yang, C. T. Crowe, J. N. Chung, and T. R. Troutt. Self-organizing particle dispersion mechanism in a plane wake. Physics of Fluids A: Fluid Dynamics, 4:2244, 1992.

[136] Tamas Tel, György Károlyi, Aron Péntek, István Scheuring, Zoltán Toroczkai, Celso Grebogi, and James Kadtke. Chaotic advection, diffusion, and reactions in open flows. Chaos: An Interdisciplinary Journal of Nonlinear Science, 10(1):89–98, 2000.

[137] F. Thomas. Physical properties of gametes in three sea urchin species. Journal of experimental biology, 194(1):263, 1994.

[138] F. I. M. Thomas. Transport and mixing of gametes in three free-spawning polychaete annelids, phragmatopoma californica (fewkes), sabellaria cementarium (moore), and schizobranchia insignis (bush). Journal of experimental marine biology and ecology, 179(1):11–27, 1994. ISSN 0022-0981.

[139] S. A. Thorpe. Langmuir circulation. Annu. Rev. Fluid Mech., 36:55–79, 2004.

[140] G. B. Thurston and G. A. Pope. Shear rate dependence of the viscoelasticity of polymer solutions.: Ii. xanthan gum. Journal of Non-Newtonian Fluid Mechanics, 9(1):69–78, 1987.

[141] George B. Thurston. Shear rate dependence of the viscoelasticity of polymer solutions.: I. theoretical model. Journal of non-newtonian fluid mechanics, 9(1):57–68, 1987.

[142] C. Tong and Z. Warhaft. Passive scalar dispersion and mixing in a turbulent jet. Journal of Fluid Mechanics, 292:1–38, 1995.

[143] Zoltán Toroczkai, György Károlyi, Áron Péntek, Tamás Tél, and Celso Grebogi. Advection of active particles in open chaotic flows. Physical review letters, 80(3):500, 1998.

[144] DJ Tritton. Experiments on the flow past a circular cylinder at low reynolds numbers. J. Fluid Mech, 6(4):547–567, 1959.

[145] B. Urlacher and O. Noble. Xanthan gum. In Thickening and gelling agents for food, pages 284–311. Springer, 1997.

[146] H. Vogel Gerhard. Fertilization kinetics of sea urchin eggs. Mathematical Biosciences, 58(2): 189–216, 1982.

[147] C. T. Wang and Y. C. Hu. Mixing of liquids using obstacles in y-type microchannels. Tamkang J. Sci. Eng, 13:385–394, 2010.

[148] Z. Warhaft. The interference of thermal fields from line sources in grid turbulence. Journal of Fluid Mechanics, 144(1):363–387, 1984.

[149] P. J. Whitcomb and C. W. Macosko. Rheology of xanthan gum. Journal of Rheology (1978-present), 22(5):493–505, 1978.

[150] P. O. Yund. How severe is sperm limitation in natural populations of marine free-spawners? Trends in Ecology & Evolution, 15(1):10–13, 2000. ISSN 0169-5347.

[151] P. O. Yund and S. K. Meidel. Sea urchin spawning in benthic boundary layers: Are eggs fertilized before advecting away from females? Limnology and oceanography, 48(2):795–801, 2003.

[152] E. M. Ziemniak, C. Jung, and T. Tél. Tracer dynamics in open hydrodynamical flows as chaotic scattering. Physica D: Nonlinear Phenomena, 76(1):123–146, 1994.

Appendix A

Papers

A.1 In Preparation Paper I

Shoaei, F and Crimaldi, J.P (in prep) **The Effect of Instantaneous Flow Structures on Mixing and Stirring Between Two Initially Distant Scalars** Journal of Experiments In Fluids

Abstract

The effect of turbulent wakes behind a round obstacle on mixing and reaction between two initially distant scalars has been investigated using a two-channel planar laser-induced fluorescence technique (2C-PLIF). The scalars are stirred and mixed in the mildly turbulent (Re=2000) wake of a round cylinder. The scalars are released continuously upstream of the cylinder, with a separation that initially impedes the reaction and would impede any possible reactions. The direct effect of the wake on mixing enhancement is determined by comparing segregation parameter for cases with and without the cylinder obstruction. Results indicate that mixing and reaction rates in the low-Damkohler limit between the two scalars plumes increase with the presence of the cylinder in the domain. The study also shows that the dominant contribution of total reaction derives from the scalar covariance associated with instantaneous flow processes, and depends strongly on streamwise location and cylinder presence. The results have broad implications for biological and ecological mixing processes involving broadcast spawning.

A.2 Proposed Paper II

Shoaei, F , Soltys, M and Crimaldi, J.P **The Role of Scalar Filament Structures on Mixing, Reactions and Segregation Parameter.** Journal of Physical Review E

Abstract

Mechanical stirring stretches introduced scalars into thin shells (in 3D) and filaments (in 2D), increasing the interfacial area between the scalar and surrounding fluid, sharpening concentration gradients, and enhancing diffusive mixing and reactions. We considered a class of reaction problems where the two reactants are initially localized and distant from one another, separated by ambient fluid that contains neither reactant. We made a simple 1-D idealized model of a representative slice across two symmetric and Gaussian representative filaments to investigate the effect of their physical characteristics such as filament width, filament separation and spatially domain averaged filament concentration on fluctuating concentration fields and to gain intuition on the processes that govern the magnitude and sign of total reaction terms.

Appendix B

Image Processing and Data Analysis Scripts and Functions

An important part of understanding the data displayed in this thesis is understanding the data processing. The image processing and analysis scripts used for this thesis were written for MATLAB. They are dependent on having the Imaging Processing Toolbox, Parallel Computing Toolbox, Statistics Toolbox and Curve Fitting Toolbox installed. All codes have been tested compatible with up to Matlab R2013b. The description and technique are fully written and presented by PhD graduated student, "Mike Soltys", in his thesis dissertation on Appendix B and C chapters. In addition, You may access all scripts and functions produced for this thesis publicly at:

http://github.com/mrsoltys/2C-PLIF.

However, a brief instruction on all calling functions, including descriptions of function dependancies, inputs and outputs for this thesis are shown in the Fig.B.1. Many of these functions rely on sub-functions included in the git repository that will not be covered here.

Function	Description	Input Parameters	Output Data
PreRun.m	Loads raw images from current directory, sorting them into groups based on SeiresName	Raw Data	'C1Dir', 'C2Dir', 'SkippedFilesDir', 'Size', 'TFORM1', 'TFORM2', 'Scale', 'SetStart', 'Cs'
ParTrans.m	Perform image rectification on a series of images	ParTrans(Direct, Start, Stop, AddCrop)	'I1Scale', 'I2Scale'
FindLambdaSSE.m	Find leakage, λ, based on image series with only one channel running	FindLambdaSSE(Direct, Start, Stop, BackStart, BackStop)	'Lambda1','Lambda2'
ParProc.m	Perform image flat fielding and error correction with λ	ParProc(Direct,Start, Stop, BackStart, BackStop)	'I1max', 'I2max'
ParTransProc.m	Combines the functions of ParTrans.m and ParProc.m for speed improvement, when both processes are needed.	ParTransProc(Direct,Start, Stop, BackStart, BackStop, AddCrop, Lambda)	'I1max', 'I2max'
FindMeanE.m	Computes time-averaged statistics including mean, RMS, covariance, and product for an image series between Start - Stop	FindMeanE(Direct, Start, Stop,eps)	'mean1', 'mean2', 'RMSE1', 'RMSE2', 'C1C2', 'Cov'
FindMeanHistTrans.m	Computes time-averaged statistics including histogram for an image series between Start - Stop	FindMeanHistTrans(Direct, Start, Stop)	'meanhist1', 'meanhist2'
MeanFigsP.m	Computes spatial-averaged statistics including mean, RMS, covariance, rho, reaction and segregation parameters for time-averaged outputs of FindMeanE.m	MeanFigsPP(MeanName , S, Shift, TitleText, FileName,eps,S1,S2)	Mean1P','Mean2P','RMSE1P','RMSE2P','CovP','C1C2P', 'RhoP','SegP','Xs','Ys','ycent','S1','S2'
MakeMovieE.m	Making the video with known FPS for an image series between Start - Stop	MakeMovieE(Direct,Start,Stop,MovieName, FPS,eps, S1,S2)	Video.avi
CSfigs.m	Computes spatial-averaged statistics for bins of #BSz pixels in z direction	CSfigs(USstart, USstop, eps, Xshift,Expon, NAME,S1,S2,BSx,BSz)	'CSys','CSmean1','CSmean2','CSrms1','CSrms2','CSs','CSrho','CSc1c2','CScov'
Clfigs.m	Computes centerline spatial-averaged statistics for bins of #BSx pixels in x direction	CLfigs(USstart, USstop, eps, Xshift,Expon, NAME,S1,S2,BSx,BSz)	CLxdat','CLmean1','CLmean2','CLmeanC1C2','CLrms1','CLrms2','CLs','CLrho','CLc1c2','CLcov'

Figure B.1: a brief instruction on calling functions, including descriptions of function dependancies, inputs and outputs, Soltys and Crimaldi [125].

Appendix C

Flow Facility Calibration Tests

C.1 Main Pump Flow Rate Calibration Tests

In order to calibrate the main pump flow rate, more than 50 different tests are taken based on two major goals:

- Getting the maximum capacity of the pump flow rate (velocity) in different weir heights installed in the flume.
- Getting the maximum flow depth in different weir heights installed in the flume.

Three different weir heights are utilized to make this calibration curve, 14", 16" and 18". Figure.C.1 shows the liner relationship between the flow depth and the velocity of the flow. But this figure implies that you can the maximum flow depth but less flow speed around for the 18" weir installed in the flume. The maximum velocity you can take from the pump in this case is around 4.2 cm/sec for 505 mm depth of the flow. In order to getting more speed flow, we used the smaller weir size and increased the velocity up to 8.6 cm/sec. For the smallest weir size (14"), we have gotten the less flow depth but faster flow speed (up to 12 cm/sec) in the flume.

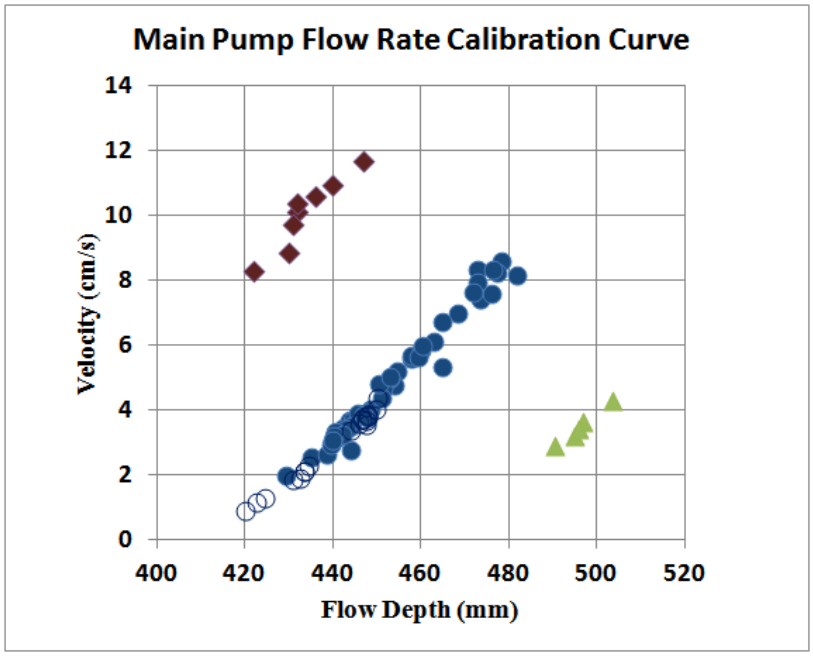

Figure C.1: Flow depth vs. flume velocity in three different weir heights (i.e., ♦ Weir 14", • Weir 16", ○ Weir 16", ▲ Weir 18") installed in the flume.

In order to run experiments in $Re_\phi = 5000$, we chose the 16" weir height and we trended the line in order to calibrate the pump setting. Figure.C.2 shows the pump calibration for the 16" weir size installed in the flume. For lower Reynolds number flow (i.e., $Re_\phi = 2000$) we chose the 18" weir height.

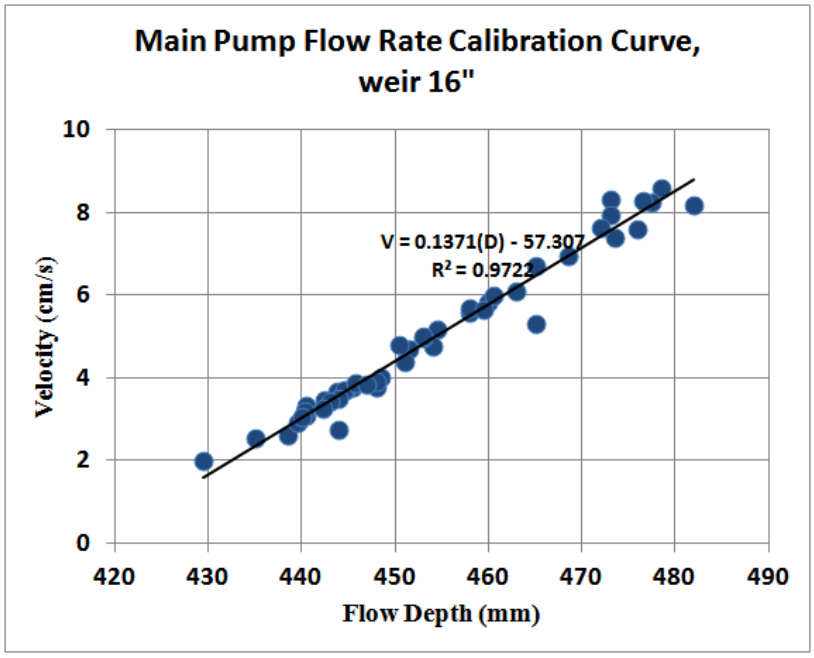

Figure C.2: Main pump flow rate calibration curve for weir height 16”

C.2 Gear Pump Rate Calibration Tests

Two micropump A-mount suction shoe pumps installed on the gear pumps and they are used for sucking and injecting the dyes from dye tank into the flume. Figure.C.3 shows the specification of those micropumps used in our PLIF experiments. It serves the flow rates between 4.6 mL/min and 460 mL/min in viscosity range between 0.2 and 1500 cP.

Specifications	
mL/rev	0.092
Wetted parts	Body: 316 SS, PPS gears, PTFE seals
Temp range	-50 to 350°F
Differential pressure (Max)	75 psi
Flow rate (min)	4.6 mL/min at 50 rpm 460 mL/min at 5000 rpm
Port size	1/8" NPT(F)
Particulates	none
Run dry	under 30 seconds
Relief valve	No
Duty cycle	continuous (from 150 to 5000 rpm)
Viscosity	0.2 to 1500 cp
Suction lift	24 in. H_2O (1750 rpm)
Manufacturer number	L20013
Internal bypass	No
Model	L20013
Reversible	No
Motor rpm	8000
Brand	Micropump

Figure C.3: Micropump specification used in the cylinder and high viscosity mixing experiments

In order to calibrate the gear pumps' flow rate used for dyes injection, more than 20 different tests are taken based on two major goals:

- Investigation on the relationship between the setting flow rate and the actual flow rate .
- Comparing and adjusting the both gear pumps using for two dyes injection.

Figure.C.4 shows the gear pump calibration for different flow settings for Oxazine dye. There is a linear relationship between the flow setting and the actual setting.

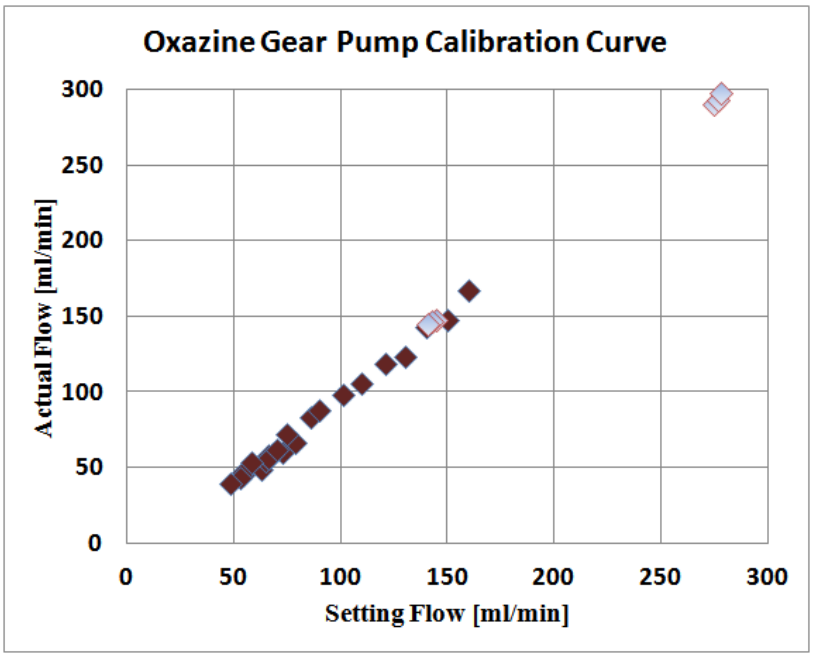

Figure C.4: Oxazine gear pump calibration (i.e., ♦ data series I, ◇ data series II)

Figure.C.5 shows the gear pump calibration for different flow settings for Fluorescein dye.

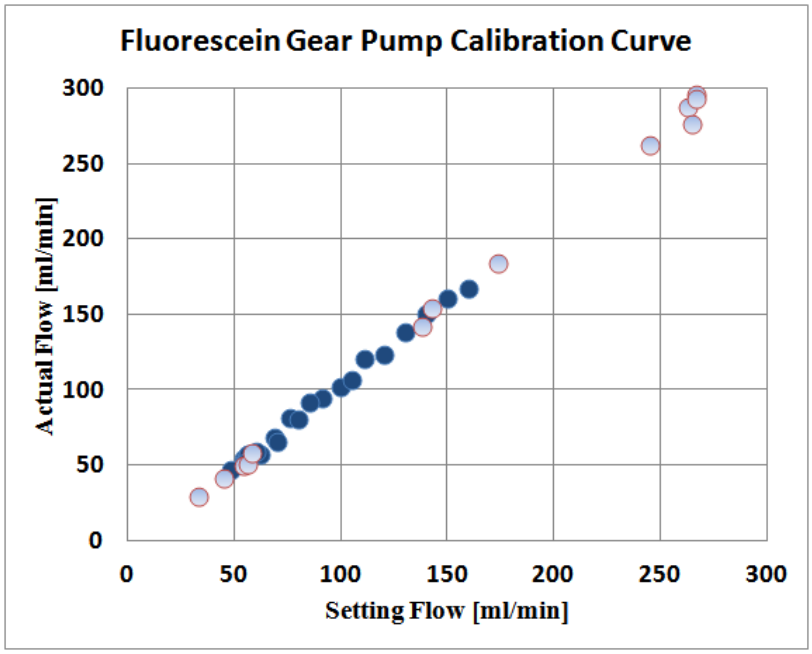

Figure C.5: Fluorescein gear pump calibration (i.e., • data series I, ○ data series II)

In order to run experiments in $Re_\phi = 2000$, those pumps were calibrated to match the flume velocity or an isokinetic release. Therefor, we chose the setting flow rate 69 mL/min for the Oxazine gear pump and 62 mL/min for the Fluorescein gear pump for the flume flow speed $U_o = 4.05$ cm/sec. For higher Reynolds number, (i.e., $Re_\phi = 5000$) we chose the 144 mL/min for the Oxazine gear pump and 137 mL/min for Fluorescein gear pump in order to giving the isokinetik flow with flow speed $U_o = 10.05$ cm/sec. Figures.C.6 and C.7 show the pump calibration for range close to designed flow rate for two dyes gear pumps.

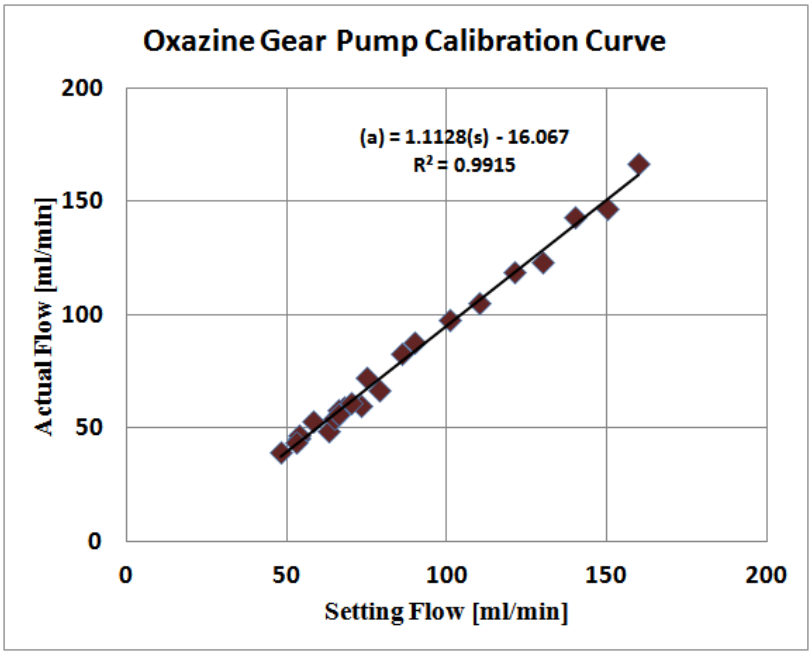

Figure C.6: Oxazine gear pump calibration for designed injection speed

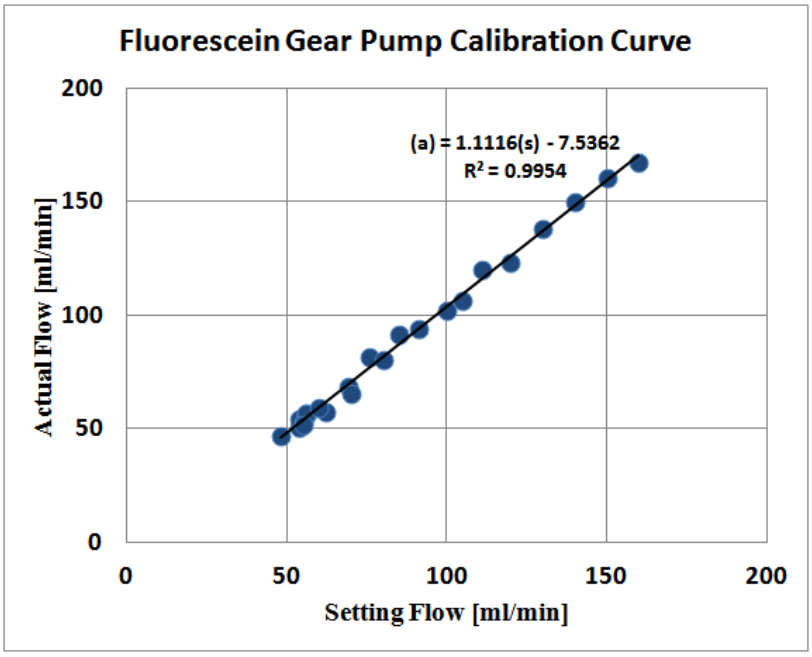

Figure C.7: Fluorescein Gear pump calibration designed injection speed

Appendix D

Physical Characteristic of a Xanthan Gum Solution versus Temperature and Time Changes

a specific volume (500mL) of 750ppm Xanthan Gum solution is made on July 3, 2014 at time: 15:03 pm. The room temperature and water in graduated glass beaker was kept constant and 22°C. All measurement is based on the Cannon-Fenske Routine Viscometer, size 100 (Fig D.1). Xanthan Gum concentration is always kept 750ppm.

16 different tests are taken based on two major goals:

- Investigation on changes of Xanthan Gum viscosity based on dye temperature.
- Investigation on changes of Xanthan Gum viscosity based on time passed since dye made.

Figure D.1: Cannon-Fenske Routine Viscometer, size 100

Here are the figures for two types of experiments done on Xanthan Gum physical characteristic.

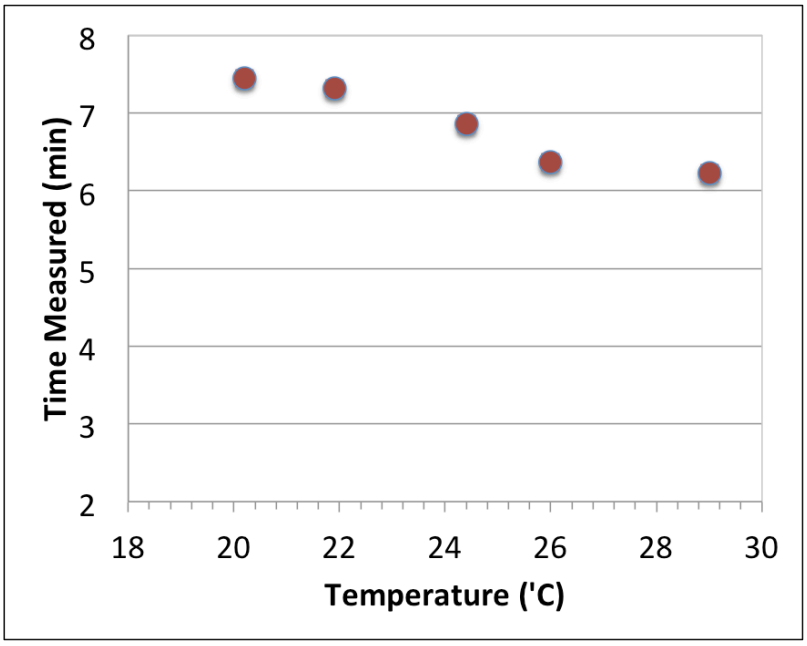

Figure D.2: Physical characteristic of a Xanthan Gum solution 750 ppm versus temperature

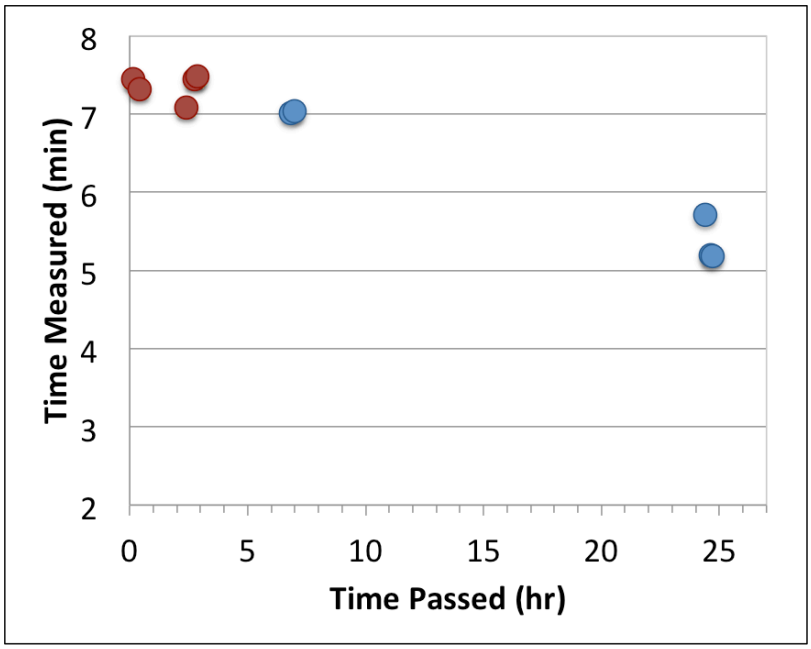

Figure D.3: Physical characteristic of a Xanthan Gum solution 750 ppm versus time passed since dye has been made, (i.e., • sample 1, • sample 2)

In Fig.D.2 you may notice that viscosity decreases with increase of temperature. (16.38% reduction). In Fig.D.3), two different batches with the same concentration have been used for the test in two different time periods. For the red circle-shape dye, it is a good sign that in the first 5 hours, the viscosity is not changed and is almost constant (i.e., NO break down is observed). For the blue circle-shape dye, It shows that after 24 hours, the viscosity decreases dramatically with time about to 25.82% reduction.

Therefore, we can rely on Xanthan Gum viscosity for the first six hours of time-made. It is almost constant. But, we should always pay attention to temperature (Both room and flume) and keep the temperature constant.

Here is the another figure for viscosity vs. time in the first six hours for two different Xanthan Gum solutions; one made in two main dye tanks and another one made in the 500mL glass beaker.

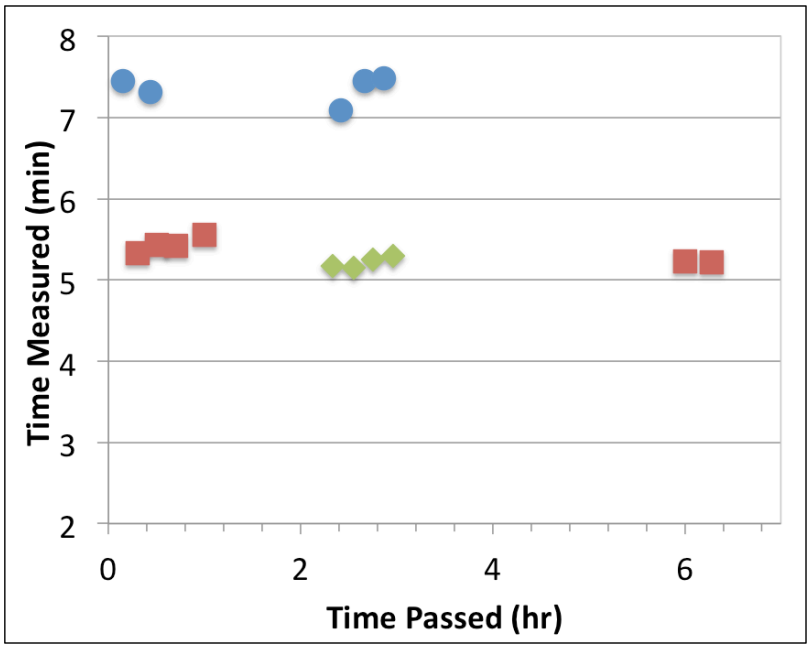

Figure D.4: Physical characteristic of a Xanthan Gum versus time for two different solutions (i.e., ● sample 1, ■ sample 2, ♦ sample 3)

You may observe that the Xanthan Gum concentration in two main dye tanks is less than the concentration in the 500mL glass beaker according to time measured in the viscosimeter. However,

there is a consistency in all viscosity measurements during the first six hours of solution has been made.

Here is the same figure including error bars on both X and Y data series.

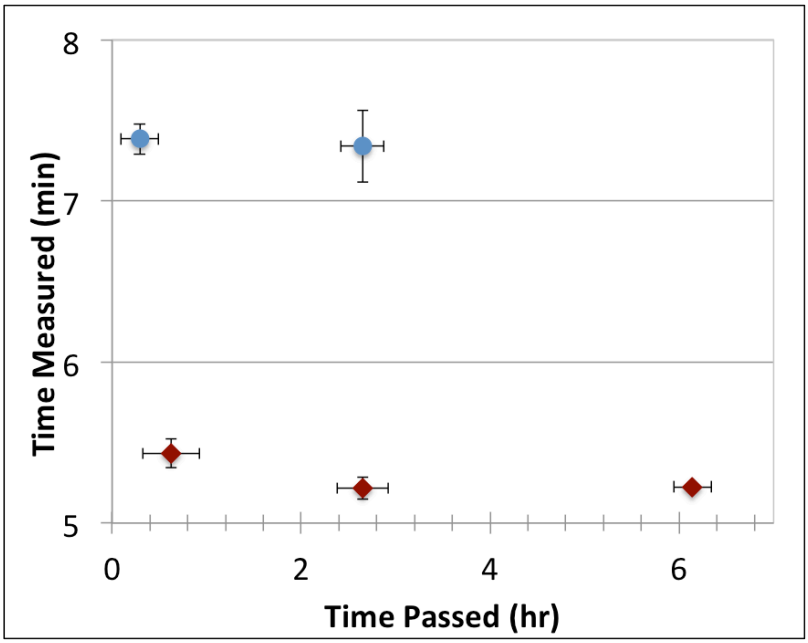

Figure D.5: Physical characteristic of a Xanthan Gum versus time for two different solutions including error bars on both X and Y (i.e., • sample 1, ♦ sample 2)

Appendix E

Summary of LDA Experiments

(a)

X [mm]	Y [mm]	**Z [mm]**	Date_Time	Count	Data Rate [#/s]	Validation [%]	**U-Mean [m/s]**	**V-Mean [m/s]**	U-RMS [m/s]	V-RMS [m/s]	U x V [x2]]
0	0	**36**	12:46:14 PM	1036	0.86	97.65	**0.0387**	**-0.0001**	0.0023	0.002	-7.22E-07
0	0	**86**	1:06:26 PM	513	0.43	95.91	**0.0395**	**0**	0.0016	0.0014	-1.43E-07
0	0	**136**	1:26:30 PM	775	0.65	98.22	**0.0392**	**-0.0002**	0.0015	0.0014	-3.63E-07
0	0	**186**	1:46:40 PM	953	0.79	97.94	**0.0393**	**-0.0002**	0.0014	0.0014	-1.89E-07
0	0	**236**	2:06:52 PM	430	0.36	99.07	**0.0342**	**-0.0003**	0.002	0.0015	5.78E-07
0	0	**286**	2:26:59 PM	325	0.27	98.11	**0.0348**	**-0.0002**	0.0019	0.0018	-1.28E-06
0	0	**336**	2:47:13 PM	708	0.59	98.56	**0.0372**	**-0.0007**	0.0017	0.0016	-3.88E-08
0	0	**386**	3:07:22 PM	1671	1.39	98.8	**0.0372**	**-0.0007**	0.0018	0.0016	-1.52E-07
0	0	**436**	3:27:30 PM	3679	2.44	98.91	**0.0368**	**-0.0003**	0.0016	0.0015	-1.77E-07

(b)

X [mm]	Y [mm]	**Z [mm]**	Date_Time	Count	Data Rate [#/s]	Validation [%]	**U-Mean [m/s]**	**V-Mean [m/s]**	U-RMS [m/s]	V-RMS [m/s]	U x V [x2]]
0	0	**36**	3:15:00 PM	2887	2.41	95.62	**0.0946**	**-0.0056**	0.0056	0.0045	-7.22E-06
0	0	**86**	3:35:05 PM	1459	1.22	96.81	**0.0963**	**-0.0055**	0.0038	0.0035	-2.58E-06
0	0	**136**	3:55:15 PM	1828	1.52	96.18	**0.0974**	**-0.006**	0.0035	0.0033	-3.69E-06
0	0	**186**	4:15:18 PM	2606	2.17	96.41	**0.0958**	**-0.0059**	0.0032	0.0031	-2.98E-06
0	0	**236**	4:35:27 PM	1201	1	97.83	**0.0845**	**-0.0055**	0.0048	0.0038	-9.88E-07
0	0	**286**	4:55:35 PM	1128	0.94	97.37	**0.0835**	**-0.0046**	0.0047	0.0043	-4.52E-06
0	0	**336**	5:15:42 PM	2730	2.28	96.77	**0.0878**	**-0.0065**	0.0044	0.0042	-5.53E-06
0	0	**386**	5:35:48 PM	6135	5.11	97.23	**0.0884**	**-0.0063**	0.0041	0.0038	-2.30E-06
0	0	**436**	5:55:54 PM	10036	8.36	97.1	**0.0898**	**-0.0056**	0.0043	0.0039	-3.10E-06

Figure E.1: Experimental parameters for LDA experiments on No Cylinder Upstream case (a)$Re_M = 1600$ (b)$Re_M = 4000$.

(c)

X [mm]	Y [mm]	**Z [mm]**	Date_Time	Count	Data Rate [#/s]	Validation [%]	**U-Mean [m/s]**	**V-Mean [m/s]**	U-RMS [m/s]	V-RMS [m/s]	U x V [x2]]
0	0	**36**	5:54:17 PM	1659	1.38	97.38	**0.042**	**-0.0021**	0.0022	0.0019	-1.37E-06
0	0	**86**	6:14:23 PM	1277	1.06	98.18	**0.042**	**-0.0015**	0.0016	0.0016	-2.65E-07
0	0	**136**	6:34:33 PM	1144	0.95	97.65	**0.0415**	**-0.0013**	0.0019	0.002	-6.40E-07
0	0	**186**	6:54:39 PM	1422	1.18	98.04	**0.0399**	**-0.001**	0.0052	0.0066	6.34E-06
0	0	**236**	7:14:49 PM	904	0.75	99.39	**0.0314**	**-0.0019**	0.0062	0.0089	6.53E-06
0	0	**286**	7:34:56 PM	663	0.55	98.11	**0.0366**	**-0.0034**	0.0056	0.0066	-5.99E-06
0	0	**336**	7:55:06 PM	1366	1.14	98.73	**0.0392**	**-0.0038**	0.0023	0.0026	-1.24E-06
0	0	**386**	8:15:15 PM	2255	1.88	98.27	**0.0395**	**-0.0035**	0.0017	0.0017	-4.66E-07
0	0	**436**	8:35:20 PM	3686	3.07	98.69	**0.0388**	**-0.0027**	0.0016	0.0016	-2.68E-07

(d)

X [mm]	Y [mm]	**Z [mm]**	Date_Time	Count	Data Rate [#/s]	Validation [%]	**U-Mean [m/s]**	**V-Mean [m/s]**	U-RMS [m/s]	V-RMS [m/s]	U x V [x2]]
0	0	**36**	6:43:45 PM	3145	2.62	94.85	**0.1008**	**-0.0057**	0.0051	0.0046	-5.22E-06
0	0	**86**	7:03:51 PM	2331	1.94	96.15	**0.1023**	**-0.0051**	0.004	0.0037	-1.71E-06
0	0	**136**	7:23:56 PM	2073	1.73	95.27	**0.1027**	**-0.0043**	0.006	0.0068	1.49E-06
0	0	**186**	7:44:03 PM	2588	2.16	94.56	**0.096**	**-0.0016**	0.0149	0.0179	3.69E-05
0	0	**236**	8:04:10 PM	1420	1.18	96.89	**0.0747**	**-0.0021**	0.0182	0.0314	9.41E-05
0	0	**286**	8:24:20 PM	1089	0.91	94.3	**0.0884**	**-0.0064**	0.0174	0.0204	2.40E-06
0	0	**336**	8:44:25 PM	2860	2.39	96.39	**0.0924**	**-0.0077**	0.0082	0.0089	-9.60E-06
0	0	**386**	9:04:31 PM	7506	6.26	95.75	**0.0939**	**-0.007**	0.0044	0.0043	-2.60E-06
0	0	**436**	9:24:37 PM	12319	10.27	96.67	**0.0949**	**-0.0062**	0.0043	0.0038	-1.84E-06

Figure E.2: Experimental parameters for LDA experiments on Cylinder Upstream case (c)$Re_\phi = 2000$ (d)$Re_\phi = 5000$.

(e)

X [mm]	Y [mm]	**Z [mm]**	Date_Time	Count	Data Rate [#/s]	Validation [%]	**U-Mean [m/s]**	**V-Mean [m/s]**	U-RMS [m/s]	V-RMS [m/s]	U x V [x2]]
0	0	**36**	6:31:48 PM	6696	7.44	96.75	**0.0379**	**-0.0016**	0.0028	0.0019	-2.19E-06
0	0	**86**	6:46:55 PM	4657	5.18	97.78	**0.0413**	**-0.0018**	0.0012	0.0014	-2.99E-07
0	0	**136**	7:02:01 PM	3728	4.14	96.74	**0.0405**	**-0.0015**	0.0012	0.0013	-4.18E-07
0	0	**186**	7:17:07 PM	4568	5.08	97.34	**0.0404**	**-0.0014**	0.0013	0.0014	-6.68E-08
0	0	**236**	7:32:13 PM	3800	4.22	97.55	**0.0379**	**-0.0014**	0.0015	0.0015	2.25E-08
0	0	**286**	7:47:20 PM	9182	10.21	97.95	**0.0375**	**-0.0012**	0.0015	0.0016	-7.16E-07
0	0	**336**	8:02:27 PM	5259	5.85	98.3	**0.0387**	**-0.0017**	0.0014	0.0015	-6.88E-07
0	0	**386**	8:17:33 PM	7898	8.78	96.92	**0.0395**	**-0.0016**	0.0014	0.0015	-6.31E-07
0	0	**436**	8:32:39 PM	5831	6.48	98.18	**0.039**	**-0.0015**	0.0014	0.0014	-4.14E-07

(f)

X [mm]	Y [mm]	**Z [mm]**	Date_Time	Count	Data Rate [#/s]	Validation [%]	**U-Mean [m/s]**	**V-Mean [m/s]**	U-RMS [m/s]	V-RMS [m/s]	U x V [x2]]
0	0	**36**	3:28:19 PM	15287	16.99	94.67	**0.093**	**-0.0038**	0.0052	0.0043	-7.76E-06
0	0	**86**	3:43:24 PM	11968	13.3	94.35	**0.0999**	**-0.0046**	0.0029	0.0032	-2.37E-06
0	0	**136**	3:58:30 PM	10115	11.24	94.49	**0.0989**	**-0.004**	0.0028	0.0031	-2.89E-06
0	0	**186**	4:13:35 PM	11378	12.64	94.5	**0.0979**	**-0.0036**	0.0028	0.0031	-1.23E-06
0	0	**236**	4:28:41 PM	11640	12.93	95.59	**0.092**	**-0.0037**	0.0035	0.0036	-1.23E-06
0	0	**286**	4:43:46 PM	20665	22.97	95.1	**0.0904**	**-0.0029**	0.0033	0.0035	-3.50E-06
0	0	**336**	4:58:52 PM	8703	9.67	96.81	**0.0927**	**-0.0044**	0.0031	0.0034	-2.81E-06
0	0	**386**	5:13:58 PM	11882	13.2	95.6	**0.0944**	**-0.004**	0.0032	0.0035	-3.73E-06
0	0	**436**	5:29:03 PM	12990	14.43	96.44	**0.0954**	**-0.0036**	0.0033	0.0033	-3.26E-06

Figure E.3: Experimental parameters for LDA experiments on No Cylinder Downstream case (e)$Re_M = 1600$ (f)$Re_M = 4000$.

(g)

X [mm]	Y [mm]	**Z [mm]**	Date_Time	Count	Data Rate [#/s]	Validation [%]	**U-Mean [m/s]**	**V-Mean [m/s]**	U-RMS [m/s]	V-RMS [m/s]	U x V [x2]]
0	0	**36**	9:09:13 PM	6636	7.37	97.73	**0.0394**	**-0.0016**	0.0031	0.0021	-2.79E-06
0	0	**86**	9:24:20 PM	4781	5.31	96.7	**0.0435**	**-0.0013**	0.0016	0.0017	-1.05E-07
0	0	**136**	9:39:26 PM	4805	5.34	96.66	**0.0422**	**-0.001**	0.002	0.0024	3.62E-07
0	0	**186**	9:54:32 PM	6998	7.77	96.55	**0.0408**	**-0.0009**	0.0028	0.0032	1.17E-06
0	0	**236**	10:09:39 PM	6232	6.93	97.45	**0.0388**	**-0.0017**	0.0034	0.004	-3.70E-07
0	0	**286**	10:24:45 PM	11830	13.15	97.15	**0.0393**	**-0.002**	0.0032	0.0037	-2.96E-06
0	0	**336**	10:39:51 PM	6707	7.45	97.56	**0.0413**	**-0.0027**	0.0025	0.0028	-1.90E-06
0	0	**386**	10:54:58 PM	9495	10.55	96.43	**0.0416**	**-0.0021**	0.0018	0.0019	-5.90E-07
0	0	**436**	11:10:04 PM	5655	6.29	97.75	**0.041**	**-0.0018**	0.0016	0.0015	-3.67E-07

(h)

X [mm]	Y [mm]	**Z [mm]**	Date_Time	Count	Data Rate [#/s]	Validation [%]	**U-Mean [m/s]**	**V-Mean [m/s]**	U-RMS [m/s]	V-RMS [m/s]	U x V [x2]]
0	0	**36**	6:45:29 PM	13941	15.49	93.86	**0.0995**	**-0.0041**	0.0061	0.0045	-1.00E-05
0	0	**86**	7:00:35 PM	14054	15.62	93.92	**0.1055**	**-0.0045**	0.0044	0.0048	5.57E-07
0	0	**136**	7:15:41 PM	13315	14.8	93.91	**0.1022**	**-0.0037**	0.0065	0.0067	5.89E-06
0	0	**186**	7:30:46 PM	14221	15.8	94.31	**0.0954**	**-0.0038**	0.0085	0.009	8.72E-06
0	0	**236**	7:45:52 PM	10513	11.68	95.92	**0.0887**	**-0.0043**	0.009	0.0102	6.08E-07
0	0	**286**	8:00:57 PM	21878	24.31	95.18	**0.0921**	**-0.004**	0.009	0.0097	-1.97E-05
0	0	**336**	8:16:04 PM	11322	12.58	95.92	**0.0981**	**-0.0049**	0.0078	0.0078	-1.36E-05
0	0	**386**	8:31:09 PM	17763	19.74	94.2	**0.1002**	**-0.0038**	0.0057	0.006	-9.90E-06
0	0	**436**	8:46:15 PM	13011	14.46	96.27	**0.1014**	**-0.0038**	0.0039	0.0039	-3.53E-06

Figure E.4: Experimental parameters for LDA experiments on Cylinder Downstream case (g)$Re_\phi = 2000$ (h)$Re_\phi = 5000$.

Appendix F

Summary of Cylinder Wake Mixing and High Viscosity Experiments

	No Cylinder US	Cylinder US	No Cylinder DS	Cylinder DS type I	Cylinder DS type II	Cylinder DS type III
Date	3/19/14	5/24/13	7/18/13	7/9/13	7/11/13	7/23/13
U [cm/s]	4.05	4.05	4.05	4.05	10.05	4.05
s/Φ	0.5	0.5	0.5	0.5	0.5	0.25
Oxazine Conc. [ppm]	0.0468	0.273	0.2828	1.5	4.5	3.528
Fluorescein Conc. [ppm]	0.0057	0.0318	0.02544	0.16875	0.405	0.23625
Pump 1 Rate [mL/min]	62	62	62	62	137	62
Pump 2 Rate [mL/min]	69	69	69	69	144	69
Dye Temp [C]	18.8	20.2	24.9	23	22.2	23.4
Krypton Ion Power [W]	0.67	0.58	0.73	0.725	0.73	0.73
Argon Ion Power [W]	0.67	0.42	0.73	0.73	0.73	0.73
Integration Time [ms]	200	300	333	533	288	333
Clear Time [ms]	1850	1850	3330	3330	1438	3330
Camera 1 Aperture	f1.4	f1.4	f1.4	f1.4	f1.4	f1.4
Camera 2 Aperture	f1.4	f2	f2.8	f2.8	f2	f2
Flow Depth [mm]	501.5	501.5	501.5	501.5	487.5	501.5
Weir Height [in]	18	18	18	18	16	18
Pump Rate [Hz]	22.75	21.25	20.5	23.5	36.5	19.65
Water Temp [C]	19.1	20.4	25.6	23.2	22.8	24

Figure F.1: Experimental parameters for select experiments on cylinder mixing from this thesis.

	Cylinder US 750 PPM	Cylinder DS 750 PPM	Cylinder DS 1000 PPM
Date	6/2/14	7/29/14	7/31/14
U [cm/s]	4.05	4.05	4.05
Oxazine Conc. [ppm]	0.051375	0.22624	0.16968
Fluorescein Conc. [ppm]	0.004725	0.017808	0.01272
Pump 1 Rate [mL/min]	62	62	62
Pump 2 Rate [mL/min]	69	69	69
Dye Temp [C]	21.4	21.1	20.5
Krypton Ion Power [W/Amp]	0.63	0.67	0.67
Argon Ion Power [W/Amp]	0.67	0.67	0.6
Integration Time [ms]	300	500	500
Clear Time [ms]	1850	3330	3330
Camera 1 Aperture	f1.4	f1.4	f1.4
Camera 2 Aperture	f2.8	f2.8	f2.8
Flow Depth [mm]	501.5	501.5	501.5
Weir Height [in]	18	18	18
Pump Rate [Hz]	24	25	25.05
Water Temp [C]	22.4	22	22.4

Figure F.2: Experimental parameters for select experiments on high viscosity from this thesis.

Appendix G

Cylinder Wake Mixing and High Viscosity Experiments Videos

Here is the list of videos available for Cylinder Mixing experiments:

- 1) $Re_\phi = 2000$, $s/\phi = 0.5$, No Cylinder US
- 2) $Re_\phi = 2000$, $s/\phi = 0.5$, Cylinder US
- 3) $Re_\phi = 2000$, $s/\phi = 0.5$, No Cylinder DS
- 4) $Re_\phi = 2000$, $s/\phi = 0.5$, Cylinder DS type I
- 5) $Re_\phi = 5000$, $s/\phi = 0.5$, Cylinder DS type II
- 6) $Re_\phi = 2000$, $s/\phi = 0.25$, Cylinder DS type III

Here is the list of videos available for High Viscosity experiments:

- 1) $Re_\phi = 2000$, $s/\phi = 0.5$, Cylinder US 750 ppm
- 2) $Re_\phi = 2000$, $s/\phi = 0.5$, Cylinder DS 750 ppm
- 3) $Re_\phi = 2000$, $s/\phi = 0.5$, Cylinder DS 1000 ppm

Here is the snapshot of MATLAB function for making the videos for each PLIF experiment.

```
function []=MakeMovieE(Direct,Start,Stop,MovieName,FPS,eps,S1,S2)

load([Direct 'Vars/PreRunVars.mat'], 'ImgStart', 'SetStop');
if nargin == 1, Start=ImgStart; Stop=SetStop(1); end


% create the AVI file object, set fps, compression, etc.
    aviFileName = [MovieName];
    aviobj = VideoWriter(aviFileName);
    aviobj.FrameRate=FPS;
    open(aviobj);

    for i=Start:Stop
        %Load Image and Scale
        load([Direct 'ProcImgs/Proc' sprintf('%05d', i)],'C1','C2');

        C1n=C1.*S1;
        C2n=C2.*S2;

        %Set <eps to 0 and >1 to 1
        C1n(abs(C1n)<=eps)=0;C2n(abs(C2n)<=eps)=0;
        C1n(C1n>1)=1;C2n(C2n>1)=1;


        %Color Change
        Img=ColorChangeWhite(C2n,C1n,1);

        Img=double(Img);
        Img(Img<0)=0;
        Img(isnan(Img))=0;
        f = im2frame(Img);

        writeVideo(aviobj,f);
        %Display Progress
            stopBar= progressbar((i-Start+1)/(Stop-Start+1),5);
            if (stopBar) break; end
    end

    % close the avi movie object
     close(aviobj);
end
```

Figure G.1: MATLAB function (MovieMakeE.m) for making the videos of PLIF Experiment